PhD-FSTC-2018-13
The Faculty of Sciences, Technology and Communication

DISSERTATION

Defense held on 09/03/2018 in Luxembourg

to obtain the degree of

DOCTEUR DE L'UNIVERSITÉ DU LUXEMBOURG
EN INFORMATIQUE

by

Christos POLITIS

Born on 22 September 1986 in Amarousio (Greece), Greece

SPECTRUM MONITORING ALGORITHMS FOR WIRELESS AND SATELLITE COMMUNICATIONS

Dissertation defense committee

Dr. Symeon CHATZINOTAS, Dissertation Supervisor

Senior Research Scientist, University of Luxembourg

Dr. Björn OTTERSTEN, Vice-Chairman

Professor, University of Luxembourg

Director of the Interdisciplinary Centre for Security, Reliability and Trust (SnT, University of Luxembourg)

Dr. Jacques KLEIN, Chairman

Senior Research Scientist, University of Luxembourg

Dr. Geert LEUS,

Professor, TU Delft, Netherlands

Dr. Konstantinos LIOLIS,

Senior Systems Engineer, SES S.A., Luxembourg

Abstract

Nowadays, there is an increasing demand for more efficient utilization of the radio frequency spectrum as new terrestrial and space services are deployed resulting in the congestion of the already crowded frequency bands. In this context, spectrum monitoring is a necessity. Spectrum monitoring techniques can be applied in a cognitive radio network, exploiting the spectrum holes and allowing the secondary users to have access in an unlicensed frequency band for them, when it is not occupied by the primary user. Furthermore, spectrum monitoring techniques can be used for interference detection in wireless and satellite communications. These two topics are addressed in this thesis.

In the beginning, a detailed survey of the existing spectrum monitoring techniques according to the way that cognitive radio users 1) can detect the presence or absence of the primary user; and 2) can access the licensed spectrum is provided. Subsequently, an overview of the problem of satellite interference and existing methods for its detection are discussed, while the contributions of this thesis are presented as well.

Moreover, this thesis discusses some issues in a cognitive radio system such as the reduction of the secondary user's throughput of the conventional "listen before talk" access method in the spectrum. Then, the idea of simultaneous spectrum sensing and data transmission through the collaboration of the secondary transmitter with receiver is proposed to address these concerns. First, the secondary receiver decodes the signal from the secondary transmitter, then, removes it from the total received signal and finally, applies spectrum sensing in the remaining signal in order to decide if the primary user is active or idle. The effects of the imperfect signal cancellation due to decoding errors, which are ignored in the existing literature, are considered in our analysis. The analytical expressions for the probabilities of false alarm and detection are derived and numerical results through simulations are also presented to validate the proposed study.

Furthermore, the threat of interference for the satellite communications services is studied in this thesis. It proposes the detection of interference on-board the satellite by introducing a spectrum monitoring unit within the satellite transponder. This development will bring several benefits such as faster reaction time and simplification of the ground stations in multi-beam satellite systems. Then, two algorithms for the detection of interference are provided. The first detection scheme is based on energy detector with signal cancellation exploiting the pilot symbols. The second detection scheme considers a two-stage detector, where first, the energy detector with signal cancellation in the pilot domain is performed, and if required, an energy detector with signal cancellation in the data domain is carried out in the second stage. Moreover, the analytical expressions for

the probabilities of false alarm and detection are derived and numerical results through simulations are provided to verify the accuracy of the proposed analysis.

Finally, this thesis goes one step further and the developed algorithms are evaluated experimentally using software defined radios, particularly universal software radio peripherals (USRPs), while it concludes discussing some open research topics.

Acknowledgements

First of all, I would like to express my sincere gratitude to my supervisor Dr. Symeon Chatzinotas, senior research scientist at SnT, for giving me the opportunity to work on this interesting topic. I am highly indebted to him for his continuous support, supervision and technical advice, which helped and encouraged me to accomplish this thesis. Furthermore, I would like to thank Professor Björn Ottesrten for his valuable suggestions and critical comments and the chance he gave to me to pursue my PhD in an excellent working environment.

I would like to express my most sincere gratitude to Dr. Sina Maleki for his excellent supervision and techical guidance and his immediate feedback to my work. I would also like to thank Dr. Christos Tsinos for his technical advice and guidance and the time he devoted to me.

I would like to thank Dr. Konstatinos Liolis from SES, who substantiated the practical aspects of my work, Professor Geert Leus and Dr. Jacques Klein for their helpful suggestions on my thesis and their participation in the evaluation committee.

Moreover, I feel the need to thank my colleagues Dr. Juan Carlos Merlano Duncan and Mr. Jevgenij Krivochiza for their time and suggestions in the implementation of my research work in the lab. In addition, I would like to thank my colleagues at SnT for the friendly and professional environment.

Most importantly, I owe all my accomplishments to the love, support and trust of my family. My father Nikos, my mother Fotini and my brother Giorgos. I dedicate this thesis to them.

Christos Politis
Luxembourg, March 2018

Contents

List of Figures

List of Tables

Abbreviations

ACM	Adaptive Coding and Modulation
ADC	Analog-to-Digital Converter
AGM	Arithmetic-to-Geometric Mean
AWGN	Additive White Gaussian Noise
BPF	Bandpass Filter
BSS	Broadcasting Satellite Service
CDF	Cumulative Distribution Function
CED	Conventional Energy Detector
CLT	Central Limit Theorem
CR	Cognitive Radio
DAC	Digital-to-Analog Converter
DDC	Digital Down-Converter
DSP	Digital Signal Processor
DTP	Digital Transparent Processor
DUC	Digital Up-Converter
DVB-S2X	Extension of second generation standard for Digital Video Broadcasting over Satellite
DVB-RCS2	second generation of Digital Video Broadcasting, Return link over Satellite
ED	Energy Detector
EDISC	Energy Detector with Imperfect Signal Cancellation
EDPSC	Energy Detector with Perfect Signal Cancellation
EME	Energy with Minimum Eigenvalue
ES	Earth Station
FDD	Frequency Division Duplex
FPGA	Field Programmable Gate Array
FSS	Fixed Satellite Service

GEO	Geostationary
GUI	Graphical User Interface
HPA	High Power Amplifier
i.i.d	independent and identically distributed
IDE	Integrated Development Environment
IF	Intermediate Frequency
IMUX	Input Multiplexer
INR	Interference-to-Noise Ratio
ISI	Intersymbol Interference
ISNR	Interference-to-Signal plus Noise Ratio
LED	Light Emitting Diode
LLF	Log-Likelihood Function
LNA	Low Noise Amplifier
LO	Local Oscillator
LPF	Low-Pass Filter
LS	Least Squares
MEO	Medium Earth Orbit
MGF	Moment Generating Function
MIMO	Multiple Input, Multiple Output
MLE	Maximum Likelihood Estimation
MME	Maximum-to-Minimum Eigenvalue
NGEO	Non Geostationary
NI	National Instruments
NP	Neyman-Pearson
OFDM	Orthogonal Frequency Division Multiplexing
OMUX	Output Multiplexer
PDF	Probability Density Function
PLL	Phase-Locked Loop
PU	Primary User
QoS	Quality of Service
RF	Radio Frequency
ROC	Receiver Operating Characteristic
Rx	Receiver

SDR	Software Defined Radio
SIGCOM	Signal Processing and Communications
SINR	Signal-to-Interference plus Noise Ratio
SISO	Single Input-Single Output
SNR	Signal-to-Noise Ratio
SU	Secondary User
TDD	Time Division Duplex
TT&C	Telemetry, Tracking and Control
Tx	Transmitter
USRP	Universal Software Radio Peripherals
VCO	Voltage Controlled Oscillators
VSAT	Very Small Aperture Terminal

Notations

$\mathbf{s}$	Column vector
$(\cdot)^T$	Transpose of $(\cdot)$
$(\cdot)^*$	Conjugate of $(\cdot)$
$(\cdot)^H$	Hermitian of $(\cdot)$
$\|\cdot\|$	Standard vector norm
$\|\cdot\|$	Absolute value
$\mathbb{E}\{\cdot\}$	Expectation of $\{\cdot\}$
$\mathbb{V}\{\cdot\}$	Variance of $\{\cdot\}$
$\mathcal{R}\{\cdot\}$	Real part of $\{\cdot\}$
$\mathcal{I}\{\cdot\}$	Imaginary part of $\{\cdot\}$

I would like to dedicate this thesis to my father Nikos, mother Fotini and brother Giorgos, who have always supported me in my life.

Chapter 1

Introduction

In this thesis, the design of spectrum monitoring algorithms for wireless and satellite communications is considered. The purpose of this chapter is to describe the motivations, the main contributions and the organization of the thesis.

1.1 Motivation

Radio frequency (RF) spectrum is not an unlimited resource. It is a very precious radio resource and needs to be used efficiently in order to ensure reliable access to the licensed users. Nowadays, there is a steady increase of new deployment of terrestrial and space systems and a constant increase in two-way communications to support broadband and broadcast services. Therefore, there is a congestion of the already crowded frequency bands and this situation results in an increasing demand for more effective and efficient utilization of the radio frequency spectrum. In this context, spectrum monitoring is a promising solution, which can be used in a plethora of applications. However, in this thesis, it is used under two scenarios: 1) in a cognitive radio (CR) system, exploiting the spectrum holes and allowing the unlicensed or secondary user (SU) to access the spectrum when it is not occupied by the primary user (PU); and 2) in a satellite communications system, helping in the detection of the RF interference on-board the satellite. Hence, this thesis is structured into two main parts as described below.

In the first part, this thesis focuses on a cognitive radio system. Cognitive radio has become a promising technology in wireless communications, because of its capability to be aware of the spectral environment, and hence offer efficient use of the spectrum [1], [2]. Spectrum sensing is the key functionality of a cognitive radio system protecting the PU from the interference caused by the SU, or for allowing the SU to access the

spectrum when it is not occupied by the PU. The common spectrum sensing techniques, in terms of the way that the cognitive radio users can detect the presence or absence of the PU are presented in [3], and include matched filter detection [4], energy detection [5]-[8], cyclostationary detection [9] and eigenvalue based detection [10]-[12].

On the other hand, the spectrum sensing paradigms discussed in the literature, according to the way that the cognitive radio users can access the licensed spectrum, are divided into the following two categories: i) quiet [13] and ii) active [14]. In quiet spectrum sensing, the SU devotes τ units of time (quiet period) in order to sense the presence or absence of the PU user before it starts the transmission. If the frequency band is detected idle (the PU is absent), the SU employs the remaining frame duration $T - \tau$ for data transmission. However, this approach uses a quiet period for spectrum sensing resulting in the reduction of SU's throughput, as no data transmission takes place during the sensing period.

To address this issue, the idea of simultaneous sensing and data transmission has been proposed. These works are distinguished into two main types: 1) techniques that apply the concept at the SU transmitter side [15]-[18]; and 2) techniques that enable the cooperation between the SU transmitter and an inactive SU [14], [19] or between the SU transmitter and the SU receiver via a control channel [20].

In the first category, the same cognitive radio device performs simultaneous sensing and communication, where the transmitter is equipped with both a sensing and a transmit unit. The critical issue of this method is the self-interference, created between the sensing and communication path because of the close proximity of the antennas. Therefore, the functionality of this method is completely based on the ability to isolate the antennas of the transmit and sensing unit and cancel the self-interference. On the other hand, there are works which propose simultaneous sensing and transmission using an inactive SU. However, again, these approaches face challenges, such as the extra power consumption and waste of resources by using an inactive SU or some other SUs for spectrum sensing.

In [20], a different concept was proposed, where the simultaneous spectrum sensing and data transmission is obtained through the collaboration of the SU transmitter and the SU receiver, which perform in different nodes. The SU transmitter is responsible for the data transmission, while the SU receiver decodes the signal from the secondary transmitter, removes it from the total received signal and carries out spectrum sensing in the remaining signal. The two main advantages of this technique compared to the approach at the transmitter's side are that 1) it does not use extra antennas for the spectrum sensing, hence, it can be easily implemented in the current systems with no additional hardware change; and also 2) it does not face the problem of self-interference that was described earlier. Furthermore, this approach offers much better detection

performance than that of using inactive SUs, if we assume that the adopted detection scheme is the conventional energy detector (CED). The reason is that the decoding and cancellation of the SU transmitted signal is almost impossible by using the inactive SU, because the latter needs information about the channel, such as modulation and coding which is hardly available in practice. However, the work of [20] is under the ideal assumption of perfect signal decoding. Unlike existing works that assume perfect signal cancellation, in this thesis, we investigate simultaneous sensing and transmission taking the imperfect signal cancellation due to decoding errors into account. Energy detection is then applied on the remaining signal to detect the presence or absence of the PU.

In the second part, this thesis focuses on a satellite communication system for the detection of interference on-board the satellite. Interference constitutes one of the main concerns for the commercial satellite telecommunication systems [21]. It has a financial impact on satellite operators, ranging from the revenue loss due to the reduction of the network capacity to the increase of the expenses for the purchase of interference monitoring equipment [22]. In addition to the satellite operators, their customers also suffer from interference because of the decreased quality of service (QoS) [23]. Therefore, interference management is a crucial issue for the commercial satellite industry.

Interference can affect both the forward and the return links. However, the uplink interference, in both cases, is propagated in the entire system, while the interference in the downlink has impact on a limited area. Consequently, this thesis focuses on the detection of the uplink RF interference by introducing a dedicated on-board spectrum monitoring unit within the satellite payload. Such an on-board unit brings several benefits with respect to the ground-based solutions: 1) monitoring the complete uplink RF spectrum by using a single equipment instead of one equipment in each downlink beam; 2) allowing faster reaction to resolve the interference on-board; and 3) offering the capability to process uplink signals which are not affected by additional downlink impairments and possible distortions related to the transponder [21], [24], [25].

The satellite operators have reported that the VSAT (very small aperture terminal) interference accounts for the majority of the interference events [26], as also shown in Figure 1.1. Each VSAT terminal transmits low power signals causing almost a negligible impact on the satellite services. However, the aggregated interference generated by a large number of geographically distributed VSAT terminals greatly affects the satellite communication services [21]. Therefore, it is required to employ algorithms for the detection of weak interfering signals, preventing the generation of aggregated VSAT interference. The conventional energy detector is considered to be a reliable detection scheme for strong interferences. However, it faces difficulties with the detection of weak

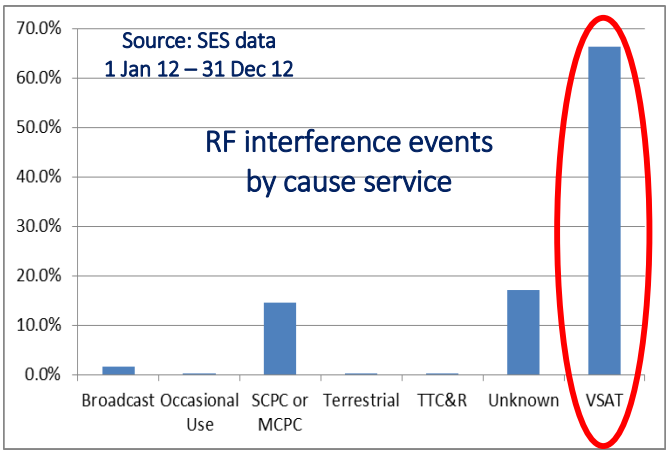

FIGURE 1.1: Radio frequency interference events, where VSAT interference is the most frequently occurring harmful RF interference type(courtesy of sIRG and SES [26]).

interference scenarios, as in this case, accurate estimation of both the noise variance and desired signal power is necessary which is very challenging in practice.

To address this concern, first, a new detection scheme based on the energy detector (ED) with signal cancellation exploiting the pilot symbols of the satellite communication standards is proposed. This proposed detector is applied only on the samples related to the position of the pilot symbols. However, the detection of weak interfering signal may require more samples than the number of pilots supported by the standards. Furthermore, if the interference is intermittent during the frame, the samples related to the position of the pilot symbols may not be affected, and thus the previous method will not provide a reliable detection of interference. To address this issue, a second more sophisticated detection scheme based on the idea of two-stage detectors [27] - [28] is also proposed.

1.2 Thesis Organization and Contributions

The outline of this thesis is included in this section. A brief explanation and the main contributions are provided for each topic. The first part of this thesis includes Chapter 2 and Chapter 3, which present a detailed survey and study the simultaneous spectrum sensing and transmission for cognitive radio networks, respectively. The second part includes Chapter 4 and Chapter 5, which deal with the interference detection on-board the satellite, and with the demonstration of the developed algorithms using software defined radios, respectively.

Chapter 2: Spectrum Sensing on Cognitive Radio and Satellite Communications

Spectrum sensing has a plethora of applications such as cognitive radio, network management, interference detection. In this chapter, a detailed survey of spectrum sensing in a cognitive radio system is presented and also a discussion about the satellite interference is provided. The spectrum sensing in the CR is distinguished into two main parts. In the first part, the spectrum sensing techniques in terms of the way that the cognitive users can detect the presence or absence of the primary user is discussed, while the second part reviews the spectrum sensing paradigms based on the way that the cognitive users can access the spectrum. Furthermore, the sources of on-board satellite interference are presented, and finally, the interference detection techniques based on the signal cancellation are reviewed [29].

Chapter 3: Simultaneous Sensing and Transmission for Cognitive Radios with Imperfect Signal Cancellation

In conventional cognitive radio systems, the secondary user employs a "listen-before-talk" paradigm, where it senses if the primary user is active or idle, before it decides to access the licensed spectrum. However, this method faces challenges with the most important being the reduction of the secondary user's throughput, as no data transmission takes place during the sensing period. In this context, this chapter discusses the idea of simultaneous spectrum sensing and data transmission through the collaboration of the secondary transmitter with the secondary receiver. First, the secondary receiver decodes the signal from the secondary transmitter, subsequently, removes it from the total received signal and then, carries out spectrum sensing in the remaining signal in order to decide about the presence or absence of the primary user. Different from the existing literature, this chapter takes into account the imperfect signal cancellation, evaluating how the decoding errors affect the sensing reliability and derives the analytical expressions for the probability of false alarm. Finally, numerical results are presented illustrating the accuracy of the proposed analysis. The content of this chapter has been published in [30] and [31].

Contributions

The contributions of this chapter are as follows:

- Unlike existing works that assume perfect signal cancellation, in this chapter, the simultaneous sensing and transmission taking the imperfect signal cancellation into account is investigated. Energy detection is then applied on the remaining signal to detect the presence or absence of the primary user.
- Evaluation how the imperfect signal cancellation due to decoding errors affects the sensing performance is carried out. In addition, the sensing performance parameters i.e., probability of detection (P_D) and probability of false alarm (P_{FA}) for BPSK, QPSK, and general M-QAM SU signals are derived.
- It is shown that the remaining signal, and consequently its energy follows a truncated distribution. Applying the concept of truncated distribution, the mean and variance of a truncated central or non-central chi-squared variable are derived. Further, in combination with central limit theorem (CLT), the distribution, mean and variance of the sum of N truncated central or non-central chi-squared variables are derived. This is used to model the distribution of the energy detection test statistics. Finally, the approximated expressions are evaluated by numerical results which verify the accuracy.

Chapter 4: Energy Detector with Imperfect Signal Cancellation for Interference Detection On-board the Satellite

Interference is a threat for the commercial satellite communication services. Strong interference can be detected by applying simple energy detection techniques. However, the low power interference is not easily detectable, for example, the interference generated by very small aperture terminals. The aggregated interference generated by geographically distributed VSAT terminals greatly affects the satellite communication services and is reported as the most important contributor to the number of interference events by the satellite operators. In this context, this chapter proposes two algorithms for the detection of weak interference, which both take place on-board the satellite. The first detection scheme is based on energy detector with signal cancellation exploiting the pilot symbols. The second detection scheme considers a two-stage detector, where first, the energy detector with signal cancellation in the pilot domain is performed, and if required, an energy detector with signal cancellation in the data domain is carried out in the second stage. The sensing reliability of both detection schemes is evaluated taking into account the channel estimation error. Furthermore, analytical closed-form expressions for the probabilities of false alarm and detection are derived. Finally, numerical results are provided to verify the accuracy and efficiency of the proposed interference detection schemes. The content of this chapter has been published in [25] and [32].

Contributions

The contributions of this chapter are as follows:

- The idea of detecting the uplink satellite interference by introducing a dedicated spectrum monitoring unit within the satellite payload is investigated. Two advanced payload architectures for this purpose are considered, based on the digital transparent processor (DTP) and Hybrid DTP/Regenerative payloads.
- Furthermore, two detectors for the detection of weak interfering signals are proposed. Both detectors are based on the energy detector and signal cancellation. The first detection scheme exploits the pilot symbols of the satellite standards, while the second detection scheme employs a two-stage detector. The first stage is again based on the pilot symbols, but the detector of the second stage processes the received signal in the data domain. Numerical results show that both detectors provide better detection performance than the conventional energy detector, particularly for weak interfering signals and in the presence of the noise and signal power uncertainties.
- In addition, evaluation how the imperfect signal cancellation due to the channel estimation error affects the sensing performance is carried out. Analytical closed-form expressions for the probability of false alarm and probability of detection are derived and the decision threshold with the aim to maximize the probability of detection for a given false alarm rate is designed. It is worth mentioning that although this chapter focuses on the detection of interference in satellite communications, the developed techniques can be straightforwardly applied in any wireless communication system.

Chapter 5: Lab Demonstration of Interference Detection

This chapter goes one step further and evaluates the developed algorithms experimentally using software defined radio (SDR). Particularly, we build a demonstrator of a realistic communication system for the detection of interference using National Instruments (NI) USRPs, which are programmed using LabVIEW Communications System Design Suite 2.0. The demonstrator consists of one transmitter, one interferer, one channel emulator and one receiver. The used NI USRP-2954R has two RF transmitters. Therefore, the Tx1 port is used for the generation of the desired signal, while the Tx2 port is used for the generation of the interference. Furthermore, the desired signal is sent to the channel emulator, which injects to the signal additive white Gaussian noise

(AWGN) with a controlled power. With this controlled artificial noise, we can adjust the desired signal-to-noise ratio (SNR). Then, this signal and the interference are added in their analog waveforms through a connector and the resulting signal is sent to the Rx port of the USRP for further processing. Then, the two main tasks are: 1) the implementation of a method for the derivation of the decision threshold; and 2) the implementation of the developed detectors for the detection of interference. Finally, this chapter demonstrates experimental results and verifies that the derived theoretical expressions are valid in a real-time practical system. The content of this chapter has been published in [33].

Chapter 6: Conclusions and Open Issues

This chapter briefly summarizes the thesis and opens research issues in the considered domain.

Appendix

The appendix includes mathematical analysis and detailed proofs of the results presented in Chapters 3 and 4.

1.3 Research Methodology

In this thesis, some theoretical and numerical tools have been used to study, analyze and evaluate our research problems. The main theoretical tools are the detection and estimation theory in statistical signal processing and the linear algebra. The detection theory enables to detect the presence or absence of the signal of interest from the random received signal. In this thesis, a binary hypothesis test has been used under two cases: 1) to detect if the primary user is active or idle in the case of simultaneous spectrum sensing and data transmission in a cognitive radio system; and 2) to detect the presence or absence of interference in a satellite communications scenario. Furthermore, the estimation theory is a mathematical tool for the estimation of an unknown parameter from a set of measured/received data. In this thesis, the least squares estimation (LS) has been used for channel estimation, while the maximum likelihood estimation (MLE) has been employed for the estimation of the unknown noise variance. Finally, linear algebra is a widely used mathematical tool in the field of signal processing and communications.

Furthermore, in this thesis the numerical analysis is obtained using two methods: 1) Monte Carlo simulations and the help of MATLAB; and 2) real time experiments and the

help of LabVIEW. In the Monte Carlo method, the considered system model is simulated by a number of realizations. In each realization, the developed algorithms perform and calculate the required performance metric. In order to estimate reliably the performance of the system, after a large number of realizations, the calculated performance metric is averaged. Then, the numeric results are compared with the analytical results in order to demonstrate the validity of the theoretical analysis.

On the other hand, in the real time experiments, a realistic demonstrator of the considered communication system using USRPs is built and the performance of the developed algorithms through real time results is evaluated. In both cases, the performance metrics are the probabilities of false alarm and detection, the interference-to-signal and noise ratio (ISNR) and the interference-to-noise ratio (INR).

1.4 Publications

The author has published his PhD research in the IEEE journal and conference papers and book chapters. The publications are listed below with the acronyms "J", "C" and "B" defining the journal, conference and book chapter publications, respectively.

Journals

- J1: C. Politis, S. Maleki, C. Tsinos, K. Liolis, S. Chatzinotas, B. Ottersten, "Simultaneous Sensing and Transmission for Cognitive Radios with Imperfect Signal Cancellation," *in IEEE Transactions on Wireless Communications (TWC)*, vol. 16, no. 9, pp. 5599–5615, Sep. 2017, *published*.

- J2: C. Politis, S. Maleki, C. Tsinos, K. Liolis, S. Chatzinotas, B. Ottersten, "Energy Detector with Imperfect Signal Cancellation for Interference Detection Onboard the Satellite, *in IEEE Transactions on Aerospace and Electronic Systems*, 2018, *submitted*.

- J3: C. Politis, S. Maleki, J. C. M. Duncan, J. Krivochiza, S. Chatzinotas, B. Ottersten, "SDR Implementation of a Testbed for Real-Time Interference Detection with Signal Cancellation, *in IEEE Access*, 2018, *submitted*.

Conferences

- C1: C. Politis, S. Maleki, C. Tsinos, S. Chatzinotas, B. Ottersten, "On-board the satellite interference detection with imperfect signal cancellation," *in IEEE International Workshop on Signal Processing Advances in Wireless Communications (SPAWC)*, Edinburgh, Scotland, Jul. 2016, *published*.

- C2: C. Politis, S. Maleki, S. Chatzinotas, B. Ottersten, "Harmful Interference Threshold and Energy Detector for On-Board Interference Detection," *22nd Ka band and Broadband Communications Conference*, Cleveland, USA, Oct. 2016, *published*.

- C3: C. Politis, S. Maleki, C. Tsinos, S. Chatzinotas, B. Ottersten, "Weak interference detection with signal cancellation in satellite communications," *in IEEE International Conference on Acoustis, Speech, and Signal Processing (ICASSP)*, New Orleans, USA, Mar. 2017, *published*.

Book Chapter

- B1: C. Politis, Ashkan Kalantari, S. Maleki, S. Chatzinotas, "On-board interference detection and localization for satellite communication," *to appear in SATCOMs in the 5G Era*, IET, 2018.

Chapter 2

Spectrum Monitoring on Cognitive Radio and Satellite Communications

First, this chapter discusses the concept of spectrum sensing in a cognitive radio system. Subsequently, it divides and reviews the spectrum sensing techniques based on the way that the cognitive users 1) detect the presence or absence of the primary user; and 2) access the licensed spectrum. Then, it talks about the interference, reviewing the interference detection techniques based on the signal cancellation and finally, it presents the scenario of the satellite interference as a suitable case for interference detection.

2.1 Cognitive Radio

Cognitive radio is a promising technology for a more efficient use of the spectrum in wireless communications. The first definition of what is a cognitive radio was proposed by J. Mitola in the late 1990's [1]. In [34], he defines the CR as "a really smart radio that would be self-, RF- and user-aware, and that would include language technology and machine vision along with a lot of high-fidelity knowledge of the radio environment". There are also many other definitions of a CR as they are proposed in [35], [36], [37] and [38]. In this thesis, the CR is defined as "a radio or system that dynamically senses the environment allowing the secondary user to have access in an unlicensed frequency band, guaranteeing at the same time the protection of the primary user".

2.1.1 Spectrum sensing in a cognitive radio system

Spectrum sensing is the most important operation of a CR [39], [40] that can be utilized in other applications as well, such as network management services [41] and interference detection [42]. This thesis is interested in using the information from spectrum sensing under two scenarios: 1) in a CR case, for protecting the PU from the interference caused by the SU, or for allowing the SU to access the spectrum when it is not occupied by the PU; and 2) in a satellite communications case, for the interference detection on-board the satellite.

2.1.1.1 Spectrum sensing techniques

There are many spectrum sensing techniques in the literature and each of them has its advantages and disadvantages in terms of the practical implementation. In [43], [44], a detailed survey of the existing spectrum sensing techniques is presented. In the following part, the most important and known techniques are discussed.

Matched filter detection

Matched filtering is an optimal detection approach when the transmitted signal is known [45]. Its main advantage is that it obtains the required probabilities of false alarm and detection in less time than most of the other detection methods [7]. However, it has some disadvantages such as: 1) it requires a priori knowledge of the signal of interest for detection, e.g, modulation, coding and etc., which is often not available in practice; and 2) it needs perfect synchronization between the transmitter and receiver, otherwise the available sensing time is reduced [46]. However, the perfect synchronization may be impossible in practical systems as in the case that the primary and secondary user are managed by different operators. Finally, this approach faces extra practical challenges as it increases the power consumption and complexity of the sensing unit.

Energy detection

Energy detector measures the energy of the received signal and compares it with a properly selected threshold to decide about the presence or absence of the signal of interest. The ED is the most popular detection method in the literature due to its low computational and implementation complexity [6], [46], [47], [48]. The ED is the optimal detection approach when the signal is random but under the widely used Gaussian assumption [49]. However, the main drawback of the ED is that it is sensitive to the noise

variance uncertainty, which results in a decreased detection performance particularly for low values of SNR. The ED is the main used detection method in this thesis, and hence a detailed analysis of the technique is provided in Section 2.3.

Cyclostationary detection

Cyclostationary detector is the most known approach in the literature that belongs to the family of feature detection techniques. The cyclostationary detector employs the cyclosationary features, like cyclic prefix, of the received signal in order to detect if the primary user is active or idle. The main advantage of this detector compared to ED is its robustness to noise variance uncertainty. However, it has two main drawbacks: 1) it requires knowledge of the cyclic frequencies from the signal that we are interested to detect; and 2) it increases the computational complexity of the sensing unit. These two characteristics make the use of the cyclostationary detector challenging in practical systems.

Eigenvalue detection

Eigenvalue detector is based on the eigenvalue decomposition of the sample covariance matrix of the received signal. Then, the eigenvalue properties are exploited in order to design the proper test statistics for the detection of the signal of interest. There are many eigenvalue detectors in the literature [10], [11], [12], [50], [51], [52], [53], [54], [55], [56], [57]. However, the most known eigenvalue detectors are the AGM (arithmetic-to-geometric mean), MME (maximum-to-minimum eigenvalue) and EME (energy with minimum eigenvalue). Eigenvalue detectors do not require a priori information of the transmitted signal and they perform better than the ED under the noise variance uncertainties scenarios, as there is no need for noise variance estimation.

Other detection techniques

There are also other detection techniques in the literature such as the autocorrelation sensing [58], [59] and the covariance sensing [60], [61]. Autocorrelation based detectors take into account the difference between the signal and noise spectrum, where this difference comes from the higher autocorrelation of the signal. On the other hand, Covariance based detectors use the sample covariance matrix of the received signal and compare it with the covariance matrix of the noise. This detector does not need any knowledge about the transmitted signal, channel and noise power.

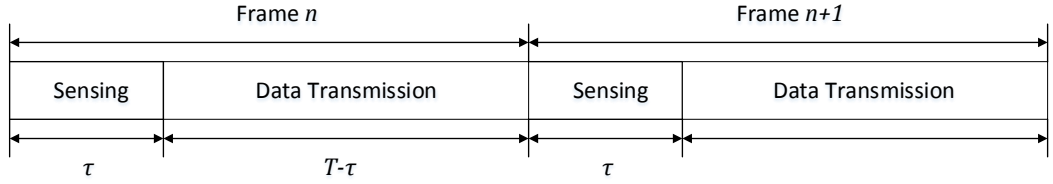

FIGURE 2.1: Quiet spectrum sensing.

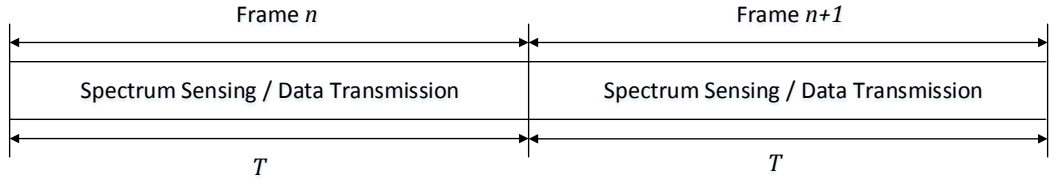

FIGURE 2.2: Simultaneous spectrum sensing and data transmission.

2.1.1.2 Spectrum access techniques

The spectrum sensing paradigms discussed in the literature, according to the way that the cognitive radio users can access the licensed spectrum, are divided into the following two categories: i) quiet [13] and ii) active [14]. In quiet spectrum sensing, the SU devotes τ units of time in order to sense the presence or absence of the PU user before it starts the transmission. If the frequency band is detected idle, the SU employs the remaining frame duration $T - \tau$ for data transmission. This strategy is depicted in Figure 2.1, where each frame is divided into two parts: 1) the spectrum sensing period; and 2) the data transmission period. The main advantage of this method is the hardware simplicity, as the switch from the sensing to communication mode can be obtained by using a single radio architecture [43]. However, this approach uses a quiet period for spectrum sensing resulting in the reduction of SU's throughput, as no data transmission takes place during the sensing period.

To address this issue, the idea of simultaneous sensing and data transmission has been proposed and the frame structure is presented in Figure 2.2. These works are distinguished into two main types: 1) techniques that apply the concept at the SU transmitter side [18]-[21]; and 2) techniques that enable the cooperation between the SU transmitter and an inactive SU [14], [19] or between the SU transmitter and the SU receiver via a control channel [20]. These approaches are summarized as follows.

In the first category, the same CR device performs simultaneous sensing and communication, where the transmitter is equipped with both a sensing and transmit unit. The critical issue of this method is the self-interference, created between the sensing and

communication path because of the close proximity of the antennas. Therefore, the functionality of this method is completely based on the ability to isolate the antennas of the transmit and sensing unit and cancel the self-interference. In [15], an approach was proposed based on the idea of spatial filtering for achieving a tolerable level of isolation. However, a stronger isolation was required and was obtained by equipping the transmitter with redundant antennas. In [16], the work of [17] was extended by proposing a multi-antenna structure, which adaptively uses spatial resources regarding the surrounding environment. However, this technique limits its applicability only to SUs equipped with multiple antennas. Furthermore, in [17] a "listen-and-talk" protocol was proposed that enables simultaneous sensing and transmission by adopting the ED as sensing scheme, where the threshold adaptively changes, in terms of the secondary transmitter activity. In [18] a two-phase concurrent sensing and transmission scheme was proposed employing a suitable control power mechanism. Nevertheless, an important drawback of these techniques is the requirement for extra dedicated hardware (antennas) for sensing that increases the cost of the system. Moreover, as mentioned earlier, these approaches introduce the phenomenon of self-interference, which degrades the sensing performance, and hence, self-interference cancellation schemes have to be adopted, which however, increase the power consumption of the system even more.

On the other hand, there are works which propose simultaneous sensing and transmission using an inactive SU. In [14] a cognitive radio system was proposed, which performs spectrum sensing through an inactive SU, while an active SU is transmitting. A similar analysis is proposed in [19], where a cognitive base station transmits data to some SUs using zero forcing, while some other SUs carry out spectrum sensing. However, again, these approaches face challenges, such as the additional power consumption and waste of resources by using an inactive SU or some other SUs for spectrum sensing.

In [20] and [62], a different concept was proposed, where the simultaneous spectrum sensing and data transmission is obtained through the collaboration of the SU transmitter and the SU receiver, which perform in different nodes. The SU transmitter is responsible for the data transmission, while the SU receiver decodes the signal from the secondary transmitter, removes it from the total received signal and carries out spectrum sensing in the remaining signal. The two main advantages of this technique compared to the approach at the transmitter's side are that 1) it does not use extra antennas for the spectrum sensing, hence, it can be easily implemented in the current systems with no additional hardware change; and also 2) it does not face the problem of self-interference that described earlier. Furthermore, this approach offers much better detection performance than that of using inactive SUs, if we assume that the adopted detection scheme is the ED. The reason is that the decoding and cancellation of the SU transmitted signal is almost impossible by using the inactive SU, because the latter

needs information about the channel, modulation and coding and etc., which are hardly available in practice. However, the work of [20] and [62] are under the ideal assumption of perfect signal decoding and Gaussian signaling, respectively.

2.2 Interference

By definition, interference is the undesired power contribution of other carriers in the frequency band occupied by the wanted carrier [63]. Interference has been identified as a threat for wireless and satellite communication systems and services, resulting in throughput degradation and revenue loss to the terrestrial and satellite operators. Therefore, a strategy for the proper management and detection of interference has to be designed.

2.2.1 Spectrum sensing for interference detection

The interference detection can be obtained based on the common spectrum sensing techniques discussed earlier, including matched filter detection [4], cyclostationary detection [9] and energy detection [5] -[8]. As mentioned earlier, matched filter detection is an optimal detection approach, however it requires a priori information of the interfering signal, e.g., modulation, coding and etc., which is often not available in practice. Furthermore, cyclostationary detection needs the knowledge of the cyclic frequencies of the interfering signal, and increases the complexity, which make it difficult for practical implementation. On the other hand, the ED does not require a priori knowledge of the interfering signal and it is the most popular detector due to its simplicity, resulting in low complexity algorithms, which constitutes a crucial factor for on-board processing. The main drawback of the ED for the detection of interference is its sensitivity to the noise variance and desired signal power uncertainties [25].

2.2.1.1 Interference detection with signal cancellation

To overcome this issue of the conventional energy detector, this thesis proposes detection schemes based on the concept of "energy detector with signal cancellation" on the pilot or data domain. There are similar works in the literature [16], [20], [64], [65], [66]. Nevertheless, [20] does not consider real constellation for the signal of interest and also assumes perfect signal cancellation. Furthermore, [16] considers a system which knows when the decoding is successful and only then it cancels the signal, while [64] and [65]

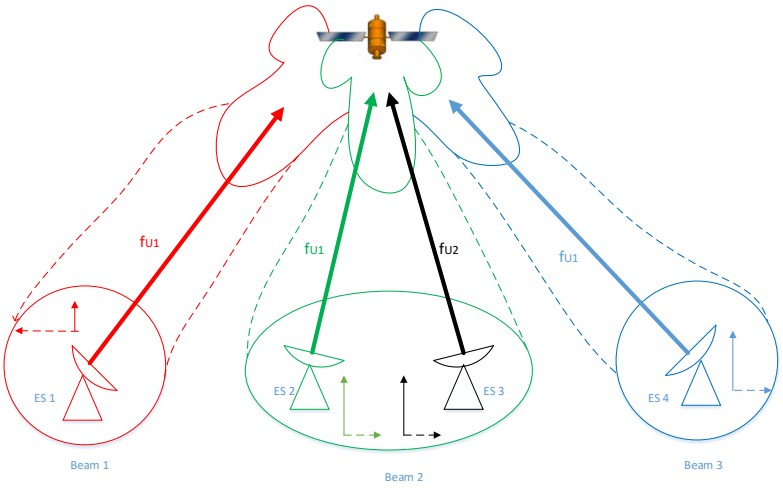

FIGURE 2.3: Sources of intra-system interference.

assume that the remaining signal after the signal or interference cancellation follows a Gaussian distribution.

2.2.2 Satellite interference

A suitable case for the detection of interference, examined in this thesis, is the satellite interference. There is a large number of scenarios where interference can occur which are described in Sections 2.2.2.1 and 2.2.2.2, focused on the uplink satellite interference. The latter can be classified into two categories: 1) intra-system interference; and 2) external interference [67].

2.2.2.1 Intra-system interference

The intra-system interference is produced over carriers transmitted by Earth stations belonging to the same system [68]. Some potential sources of intra-system interference in the satellite network are: co-channel interference, adjacent channel interference and cross-poll interference [63] - [70] as they are depicted in Figure 2.3. This figure presents three beams assuming that the Earth station (ES) 2 of beam 2 is the useful ES.

- **Co-channel interference** is generated due to imperfect isolation between different beams. In Figure 2.3, the ES 2 transmits a signal which is received by the antenna which defines the beam 2, in the main lobe with the maximum antenna gain. Moreover, the ES 4 of beam 3 transmits a signal at the same frequency and

polarization as the ES 2 and the signal is received by the side lobes of the antenna defining the beam 2, with low but non-zero gain. Therefore the carrier of beam 3 appears as interference noise in the spectrum of the carrier of beam 2, producing co-channel interference.

- **Cross-poll interference** is the result of the opposite polarization field of the carriers. In Figure 2.3, if the ES 1 of beam 1 transmits at the same frequency but opposite polarization as the carrier of the useful ES, cross-poll interference is produced.
- **Adjacent channel interference** is produced due to the fact that part of the power of the adjacent carrier at frequency f_{U2} is captured by the satellite tuned to the carrier at frequency f_{U1}. In Figure 2.3, we see that part of the power of the signal transmitted by the ES 3 of beam 2, at the same polarization but different frequency as the ES 2, is introduced as a result of imperfect filtering in the channel occupied by the carrier of ES 2, generating this way adjacent channel interference.

2.2.2.2 External interference

The external interference is produced by carriers from Earth stations belonging to a different system [68]. Some examples of potential external interference sources are: adjacent system interference, in-line interference, terrestrial interference and intentional interference.

- **Adjacent system interference** is generated by an ES into an adjacent satellite. This type of interference is typically accidental, due to operator errors, poor inter-system coordination or poor equipment setup. A scenario of adjacent system interference is presented in Figure 2.4, where the interfering source is transmitting towards the operational satellite.
- **In-line interference** [71], [72] is produced when an NGEO (non geostationary) satellite passes through a line of sight path between an ES and the GEO (geostationary) satellite in the co-existence scenarios of GEO and NGEO networks. This type of interference is shown in Figure 2.5.
- **Terrestrial interference** is produced due to the fact that some frequency bands allocated to satellite communications are often also allocated to terrestrial communications, particularly at C-band.
- **Intentional interference** is generated when an interfering signal is designed to degrade the performance of the satellite system. The most known type of intentional interference is the jamming.

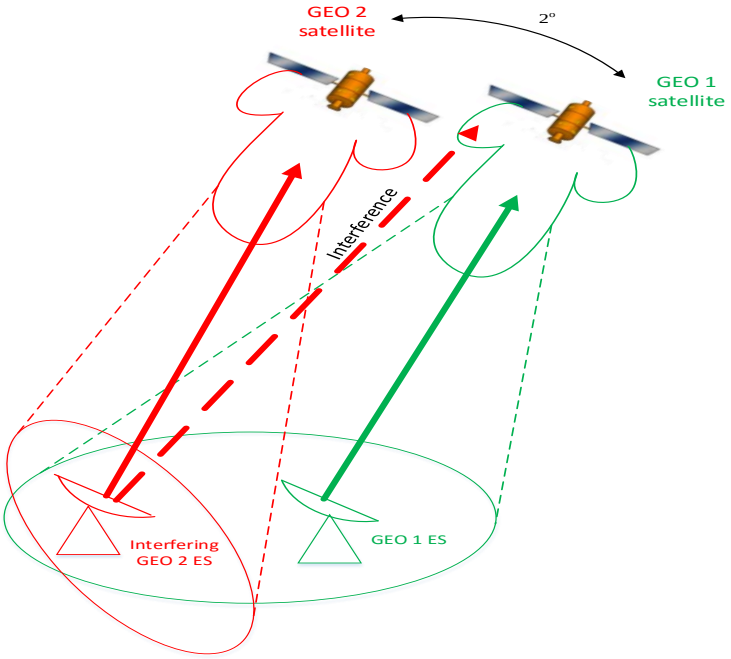

FIGURE 2.4: Adjacent system interference.

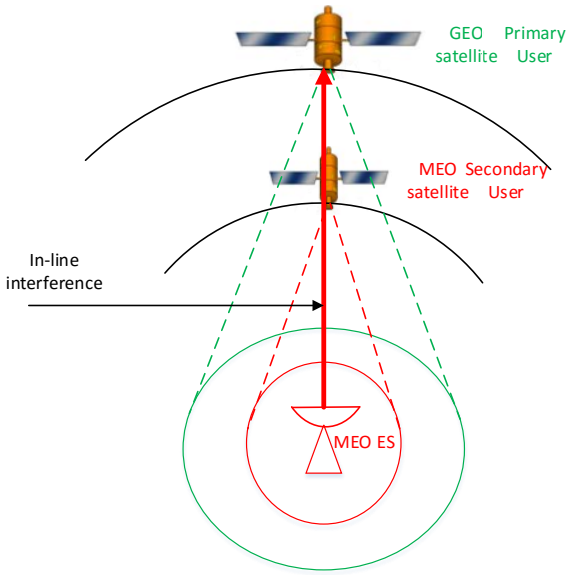

FIGURE 2.5: In-line interference.

From the above analysis, the uplink satellite interference can be also classified in terms of the nature of the interference source into intentional interference (e.g., jamming) and unintentional interference (e.g., co-channel, cross-poll, adjacent channel, adjacent system, in-line and terrestrial interference). The satellite operators have estimated that

90% of all interference events are due to unintentional interference, while intentional interferences correspond to 10% of them [69] - [70].

Finally, the types of unintentional interference can be further classified according to the service that the interfering signals belong (e.g., broadcasting satellite service (BSS), fixed satellite service (FSS), VSAT). According to SES data [26], a VSAT interference is the most critical and with the most important contribution to the number of interference events. Each VSAT terminal transmits a low power signal, however, there is a large number of geographically distributed VSAT terminals, and hence, the aggregated interference from many of them has an important impact on satellite communications.

2.2.2.3 On-ground based solution for satellite interference detection

The satellite acts as a transparent transponder and all the processing is performed on-ground possibly combined with other functionalities. A possible solution is provided by SIEMENS [73], by using the error vector magnitude [74], which enables detection of interfering in-band spurious signals without deteriorating ongoing transmissions. Another solution is provided by GLOWLINK [75], by using a two-steps method: i) a signal separator processes the received signal to form an estimate of the desired communication signal and an estimate of the in-band signals; and ii) a performance improver processes the received signal and the estimate of the one or more in-band signals to form an improved estimate of the desired communication signal and an improved estimate of the in-band signals. Finally, some other solutions are supported by KRATOS and include Monics Net [76] for RF interference detection and SatGuard [77] for identifying VSAT interference.

2.2.2.4 On-board based solution for satellite interference detection

On the other hand, the processing for the detection of the interference takes place on-board the satellite. This choice brings several benefits compared to a ground-based solution such as avoiding duplication of hardware at multiple ground stations and potential downlink impairments. For the implementation of this method, as mentioned earlier, this thesis proposes interference detection algorithms based on the concept of "energy detector with signal cancellation" on the pilot or data domain.

2.3 Basic Principles of Energy Detection

In this section, a general detection problem is presented and the basic principle of the energy detector is shown.

Let us consider a cognitive radio system, where we want to detect if the PU is active or idle in a specific frequency band. This detection problem can be formulated as follows:

$$\mathcal{H}_0: \quad y(n)=w(n), \qquad n=0,1,...,N-1 \tag{2.1}$$

$$\mathcal{H}_1: \quad y(n)=x(n)+w(n), \qquad n=0,1,...,N-1 \tag{2.2}$$

where $y(n)$ denotes the received signal at the CR receiver at the n_{th} time instant, $x(n)$ denotes the transmitted signal at the n_{th} time instant and follows Gaussian distribution with variance σ_x^2 and $w(n)$ denotes the additive white Gaussian noise (AWGN) at the n_{th} time instant with variance σ_w^2. Furthermore, $\mathcal{H}_0$ represents the hypothesis where the PU is absent, while $\mathcal{H}_1$ corresponds to the hypothesis where the PU is present.

Based on this detection problem, a proper test statistic has to be used and compared with a selected decision threshold ε. If the hypothesis $\mathcal{H}_0$ is satisfied the PU is idle, while if the hypothesis $\mathcal{H}_1$ is satisfied, the PU is active. Therefore, the evaluation of each detector depends on the probabilities of false alarm and detection. The probability of false alarm happens when we decide $\mathcal{H}_1$ while $\mathcal{H}_0$ is true. On the other hand, the probability of detection happens when we decide $\mathcal{H}_1$ and $\mathcal{H}_1$ is true.

The most popular approach that maximizes the probability of detection for a given probability of false alarm is the Neyman-Pearson (NP) theorem [49]. A NP detector decides $\mathcal{H}_1$ if thelikelihood ratio exceeds a threshold as follows:

$$L(\mathbf{y}) = \frac{p\left(\mathbf{x};\mathcal{H}_1\right)}{p\left(\mathbf{x};\mathcal{H}_0\right)} > \varepsilon. \tag{2.3}$$

But, from the above assumptions for the distribution of signal and noise, the likelihood ratio can be written as:

$$L(\mathbf{y}) = \frac{\frac{1}{(2\pi(\sigma_x^2+\sigma_w^2))^{\frac{N}{2}}} e^{\frac{1}{2(\sigma_x^2+\sigma_w^2)}\sum_{n=0}^{N-1} y(n)^2}}{\frac{1}{(2\pi(\sigma_w^2))^{\frac{N}{2}}} e^{\frac{1}{2(\sigma_w^2)}\sum_{n=0}^{N-1} y(n)^2}}. \tag{2.4}$$

Then, the log-likelihood ratio is expressed as:

$$l\left(\mathbf{y}\right) = \frac{N}{2}\ln\left(\frac{\sigma_w^2}{\sigma_x^2+\sigma_w^2}\right) + \frac{1}{2}\frac{\sigma_x^2}{\sigma_x^2\left(\sigma_x^2+\sigma_w^2\right)}\sum_{n=0}^{N-1} y\left(n\right)^2. \tag{2.5}$$

Therefore, we decide $\mathcal{H}_1$ if

$$T(\mathbf{y}) = \sum_{n=0}^{N-1} y(n)^2 > \varepsilon'. \tag{2.6}$$

From (2.6), it is shown that the NP detector calculates the energy of the received signal and compares it with a decision threshold. This detector is known as an energy detector.

2.4 Summary

This chapter presented the idea of cognitive communications and reviewed the existing spectrum sensing and access techniques. Furthermore, an overview of interference detection techniques through signal cancellation was provided. Subsequently, it described the interference on satellite communications and concluded studying the basic principles of the energy detector.

Chapter 3

Simultaneous Sensing and Transmission for Cognitive Radios with Imperfect Signal Cancellation

This chapter presents a novel algorithm for simultaneous spectrum sensing and data transmission through the cooperation of the secondary user transmitter with the secondary user receiver. In Section 3.2, the system model and the proposed method are described. Section 3.3 derives the probabilities of false alarm and detection for BPSK and QPSK SU modulated signals, while Section 3.4 provides the expression of probability of false alarm for any M-QAM SU modulated scheme. Numerical results are illustrated in Section 3.5. Finally, Section 3.6 summarizes the chapter.

3.1 Introduction

As mentioned in Chapters 1 and 2, if the cognitive radios users access the spectrum through the conventional "listen before talk" approach, the throughput of the secondary user reduces. In the literature review of Section 2.1.1.2, a detailed overview of the existing spectrum access techniques was presented, discussing their advantages and disadvantages. Then, it was shown that a promising solution to address this issue is the simultaneous spectrum sensing and data transmission through the collaboration of the secondary transmitter with the secondary receiver, where this method considers signal cancellation. However, the imperfect signal cancellation under the scenario of real constellations and not Gaussian signal is neglected in the literature.

3.1.1 Chapter Contributions

In this context, the contributions of this chapter are three-fold:

- Unlike existing works that assume perfect signal cancellation, in this chapter, the simultaneous sensing and transmission taking the imperfect signal cancellation into account is investigated. Energy detection is then applied on the remaining signal to detect the presence or absence of the primary user.
- Evaluation how the imperfect signal cancellation due to decoding errors affects the sensing performance is carried out. In addition, the sensing performance parameters i.e., probability of detection and probability of false alarm for BPSK, QPSK, and general M-QAM SU signals are derived.
- It is shown that the remaining signal, and consequently its energy follows a truncated distribution. Applying the concept of truncated distribution, the mean and variance of a truncated central or non-central chi-squared variable are derived. Further, in combination with central limit theorem, the distribution, mean and variance of the sum of N truncated central or non-central chi-squared variables are derived. This is used to model the distribution of the energy detection test statistics. Finally, the approximated expressions are evaluated by numerical results which verify the accuracy.

3.2 System model

3.2.1 Signal model

A cognitive radio system as shown in Figure 3.1 is considered, where the primary user transmitter (PU-Tx) and the secondary user transmitter/receiver (SU-Tx/Rx) are equipped with one antenna. The goal of this system is to detect if the PU is active or idle following the concept of simultaneous spectrum sensing and data transmission through the cooperation of the SU-Tx and the SU-Rx. Therefore, the detection problem can be formulated as the following binary hypothesis test, which is a baseband symbol sampled model:

$$\mathcal{H}_0: \quad \mathbf{y}=h\mathbf{s}+\mathbf{w}, \tag{3.1}$$

$$\mathcal{H}_1: \quad \mathbf{y}=\mathbf{x}_p+h\mathbf{s}+\mathbf{w}, \tag{3.2}$$

where h denotes the scalar flat fading channel from the SU-Tx to the SU-Rx, which is assumed to be known at the secondary users as in [20], and it is also assumed to be

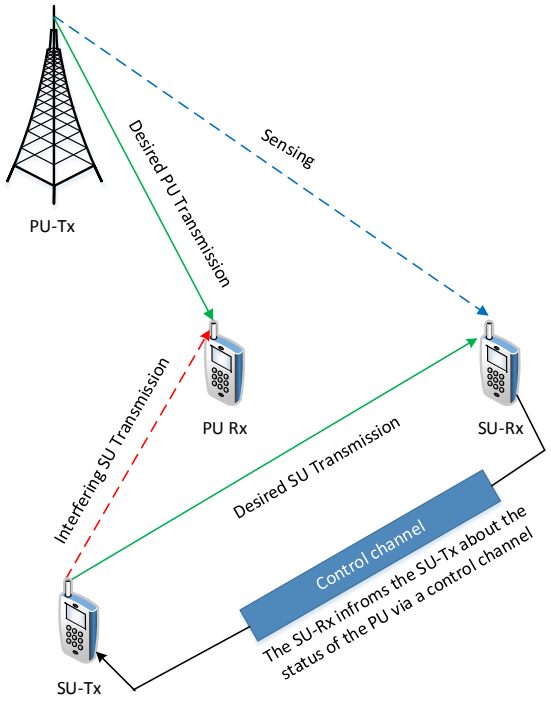

FIGURE 3.1: System model.

real after the phase compensation with channel power γ, $\mathbf{s} = [s(1) \ \cdots s(N)]^T$ denotes an $N \times 1$ vector, which is the signal transmitted by the SU-Tx with power P_s and it is a modulated signal, $\mathbf{x}_p = [x_p(1) \ \cdots x_p(N)]^T$ denotes an $N \times 1$ vector, referred to as the received (faded) signal from the PU-Tx, $\mathbf{w} = [w(1) \ \cdots w(N)]^T$ denotes an $N \times 1$ vector, which is the additive noise at the receiving antenna of the SU-Rx, modelled as an independent and identically distributed (i.i.d.) complex Gaussian vector with zero mean and covariance matrix given by $E\{\mathbf{w}\mathbf{w}^H\} = \sigma_w^2 \mathbf{I}_N$, where $\mathbf{I}_N$ denotes an identity matrix of size N, and $\mathbf{y} = [y(1) \ \cdots y(N)]^T$ denotes an $N \times 1$ vector, referred to as the total received signal at the SU-Rx.

As mentioned, this chapter assumes that the channel is known. However, in reality, the channel should be estimated. Therefore, the channel estimation error is an important factor which has to be taken into account in the analysis, constituting a valuable idea for future studies. Nevertheless, in Section 3.5, preliminary results present how this uncertainty affects the sensing performance of the proposed detector.

3.2.2 Method description

In a CR network, the goal of the SU-Tx is to access the spectrum when it is not occupied by the PU and thus avoiding interference to the PU network (this is obtained by

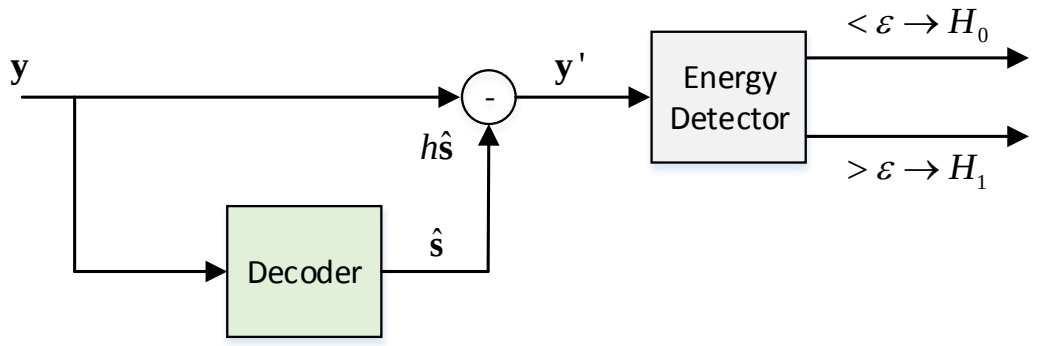

FIGURE 3.2: Receiver structure of the proposed method for spectrum sensing and data transmission at the same time.

considering a high target probability of detection). Therefore, in the beginning, namely during the very first frame of cognitive data transmission, the SU-Tx divides the frame in two time slots: 1) one sensing period (τ units of time); and 2) one data transmission period (T units of time). If the PU is detected to be idle during the sensing period, the SU-Tx changes mode and starts the data transmission to the SU-Rx. Then, in the following frames the SU-Rx decodes the signal of the SU-Tx and removes it from the total received signal. Subsequently, a detector is applied to the remaining signal for spectrum sensing. At the end of the frame, if the SU detects a change in the state of the PU (e.g. the PU starts the transmission after the sensing period), then the SU-Rx informs the SU-Tx via a control channel and the latter stops the transmission in order to avoid causing interference to the PU. Hence, in the next frame, the SU-Tx, again, divides the frame in two time slots and the above process is repeated. However, at the end of the frame, if the SU detects that the frequency band is idle (absence of the PU), there is no need to devote a period for sensing during the next frame, and then, the idea of simultaneous spectrum sensing and data transmission is applied improving the SU's throughput. The structure of the secondary receiver is depicted in Figure 3.2, while the frame structure of this method is presented in Figure 3.3.

3.2.3 Proposed algorithm

The aforementioned methodology can be applied for any modulation scheme, but in this step, for simplicity, we consider that the transmitted signal from the SU is BPSK modulated and the noise is a real (not complex) Gaussian vector. Later, it will be shown how the proposed algorithm can be applied for QPSK and any M-QAM modulated signal with complex Gaussian noise. Hence, following these assumptions the detection problem of (3.1)-(3.2) can be reformulated via the following procedure.

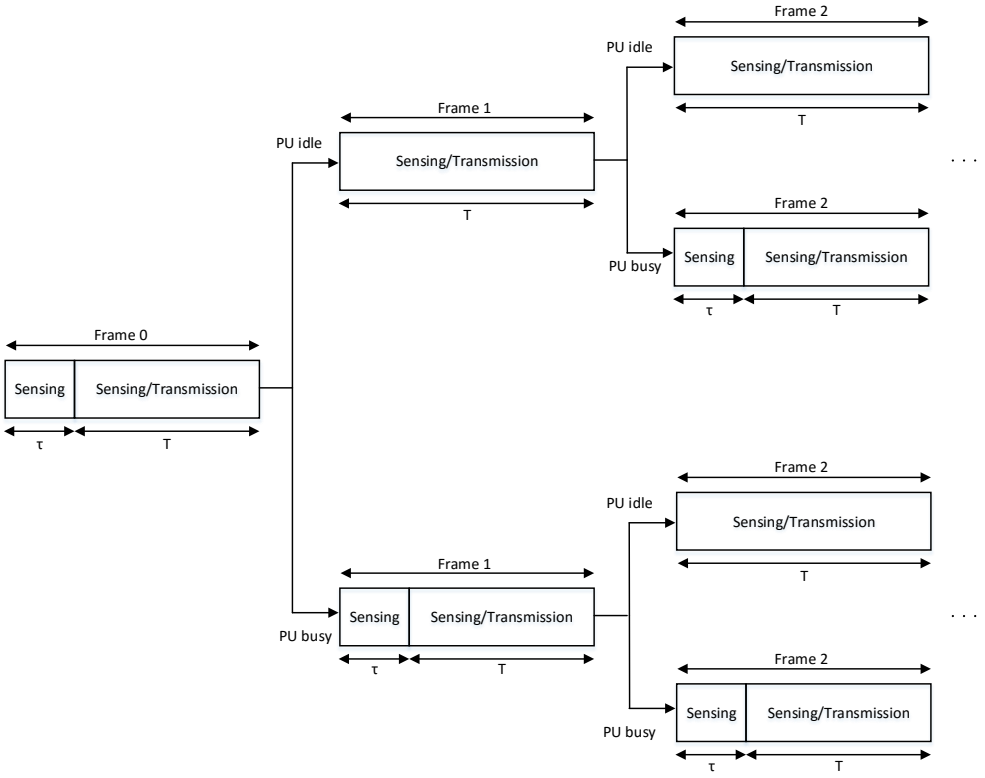

FIGURE 3.3: Frame structure of the proposed simultaneous sensing and transmission method.

1. After the initial stage of sensing, the SU-Rx tries to decode the signal transmitted by the SU-Tx, using the BPSK demodulator, which is based on the Euclidean distance [45]. Note that given that the transmitted symbol is $s = \sqrt{P_s}$, the correctly decoded signal is $\hat{s} = \sqrt{P_s}$, while the wrongly decoded signal is $\hat{s} = -\sqrt{P_s}$ or more generally

$$\hat{s} = \begin{cases} +s & \rightarrow \quad \text{correct decoding,} \\ -s & \rightarrow \quad \text{wrong decoding.} \end{cases} \tag{3.3}$$

2. Then, the decoded signal is removed from the total received signal and the new hypothesis test is expressed as follows:

$$\mathcal{H}_{0_B} = \begin{cases} \mathcal{H}_{00_B} : y'(n) = w(n) & n = 0, 1, ..., N-1, \\ \mathcal{H}_{01_B} : y'(n) = 2hs(n) + w(n) & n = 0, 1, ..., N-1, \end{cases} \tag{3.4}$$

$$\mathcal{H}_{1_B} = \begin{cases} \mathcal{H}_{10_B} : y'(n) = x_p(n) + w(n) & n = 0, 1, ..., N-1, \\ \mathcal{H}_{11_B} : y'(n) = x_p(n) + 2hs(n) + w(n) & n = 0, 1, ..., N-1, \end{cases} \tag{3.5}$$

where the index B in the hypothesis test denotes the BPSK scenario, $\mathcal{H}_{00_B}$ and $\mathcal{H}_{10_B}$ correspond to the hypothesis of correct decoding of the received signal, while

the PU is idle and active, respectively, while $\mathcal{H}_{01_B}$ and $\mathcal{H}_{11_B}$ represent the wrong decoding case, while the PU is idle and active, respectively. Now, it is clear that without considering the decoding errors (hypotheses $\mathcal{H}_{01_B}$ and $\mathcal{H}_{11_B}$), the new hypothesis test is the same as the one of quiet spectrum sensing, with the difference that here, the whole duration of the frame is used for spectrum sensing instead of a small quiet period.

3. The last step is the application of the ED in the remaining signal, examining how the decoding errors affect the sensing performance. The ED is selected as detection technique due to the fact that it does not require knowledge of the PU characteristics (modulation type, pulse shaping, etc.), which are often unknown. The ED is shown in (3.6)

$$T(\mathbf{y}) = \|\mathbf{y}\|^2 = \sum_{n=0}^{N-1} |y[n]|^2 \begin{array}{l} < \varepsilon \rightarrow \mathcal{H}_{0_B} \\ > \varepsilon \rightarrow \mathcal{H}_{1_B} \end{array}, \tag{3.6}$$

where ε denotes a properly defined threshold, responsible for the decision about the presence or absence of the PU.

3.3 Probability of False Alarm and Probability of Detection

The calculation of the detection threshold ε is independent from the transmitted primary signal and hence, the evaluation of our proposed detection scheme is obtained via the derivation of the P_{FA}. Therefore, in this section, the P_{FA} is mainly derived, first for BPSK and then for QPSK SU modulated signals. Furthermore, for the same SU modulated signals, the P_D under the assumption that the primary user is Gaussian-distributed is derived.

3.3.1 Probability of false alarm for BPSK signals

In this subsection, the probability of false alarm for the BPSK case (P_{FA_B}) is determined by Theorem 3.1, which is subsequently proved.

Theorem 3.1: Consider a secondary user with one receive antenna, which collects a large number of samples N. The SU-Rx decodes the received samples, removes them from the total received signal and applies an ED in the remaining signal. Then, the P_{FA_B} is

defined by

$$P_{FA_B} = \sum_{k=0}^{N} \left(\begin{array}{c} N \\ k \end{array} \right) P_{k_B} P_{e_B}^{k} \left(1 - P_{e_B}\right)^{N-k}, \tag{3.7}$$

where k denotes the number of wrong decoded bits, $P_{\mathrm{eB}} = Q\left(\sqrt{\frac{\gamma P_s}{\sigma_w^2}}\right)$ is the probability of bit error for BPSK [45] and P_{k_B} is the probability of false alarm for the case that k bits are decoded wrongly, which can be approximated as follows:

$$P_{k_B} = Q\left(\frac{\varepsilon - \mu_{\mathcal{H}_{0_B}}}{\sqrt{V_{\mathcal{H}_{0_B}}}}\right), \tag{3.8}$$

where $\mu_{\mathcal{H}_{0_B}}$ and $V_{\mathcal{H}_{0_B}}$ are the mean and variance of the test statistic $T\left(\mathbf{y}' \left| \mathcal{H}_{0_B} \right.\right)$, respectively.

Proof: The Binomial distribution [78] is used for the proof of the first part of Theorem 1, due to the fact that considering independent experiments, the number of wrong decoded bits is different in each of them, ranging from 0 to N with a corresponding probability. For the second part, the probability of false alarm P_{k_B} of the ED of (3.6) is determined by $P_{k_B}\left(\varepsilon\right) = \Pr\left(T\left(\mathbf{y}'\right) > \varepsilon | \mathcal{H}_{0_B}\right)$, where the derivation of the distribution of the test statistic $T\left(\mathbf{y}' \left| \mathcal{H}_{0_B} \right.\right)$ is required.

Focusing on $\mathcal{H}_{00_B}$, we can notice that the remaining signal, after the cancellation of the correct decoded signal, consists only of noise. This vector includes the set of noise values, which let the BPSK demodulator to decide correctly about the transmitted symbol. Then, the cumulative distribution function (CDF) of the remaining signal under $\mathcal{H}_{00_B}$ can be written as follows:

$$\begin{aligned} F_y\left(g \left| \mathcal{H}_{00_B} \right.\right) &= P\left\{y \leq g | \mathcal{H}_{00_B}\right\} \\ &= P\left\{y \leq g | c_B, s = +\sqrt{P_s}\right\} P\left(s = +\sqrt{P_s}\right) \\ &+ P\left\{y \leq g | c_B, s = -\sqrt{P_s}\right\} P\left(s = -\sqrt{P_s}\right) \\ &= \frac{1}{2} P\left\{w \leq g | g \geq -\sqrt{P_s}\right\} + \frac{1}{2} P\left\{w \leq g | g \leq \sqrt{P_s}\right\}, \end{aligned} \tag{3.9}$$

where the symbols are assumed to be of equal probability ($P(s = +\sqrt{P_s}) = P(s = -\sqrt{P_s}) = 1/2$), c_B denotes the correct decision event under the BPSK scenario and $F_y\left(g | \mathcal{H}_{00_B}\right)$ represents the CDF of y under $\mathcal{H}_{00_B}$. As it can be seen, the CDF is related to two cases: 1) correct decoding given that the transmitted symbol is $s = +\sqrt{P_s}$; or 2) correct decoding given that the transmitted symbol is $s = -\sqrt{P_s}$. Then, the distribution of noise for both scenarios is depicted in Figures 3.4 and 3.5. A very interesting information which can be extracted by these two figures is that the received signal is always decoded correctly in the region where $-\sqrt{\frac{\gamma P_s}{\sigma_w^2}} \leq w \leq +\sqrt{\frac{\gamma P_s}{\sigma_w^2}}$, while it

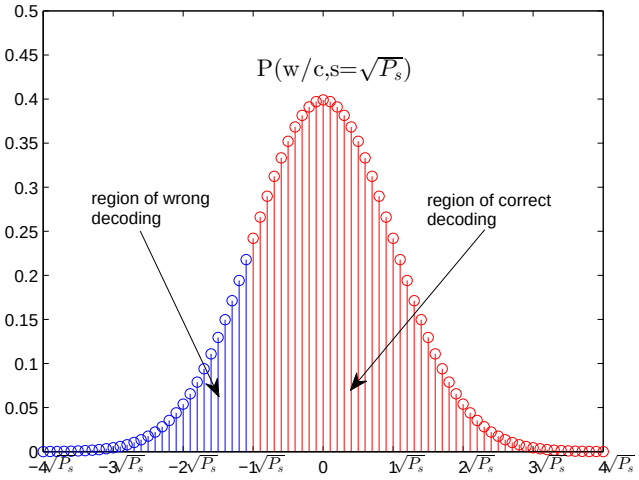

FIGURE 3.4: Distribution of noise under the hypothesis $\mathcal{H}_{00_B}$ and the correct decoding of $s = \sqrt{P_s} = 1$.

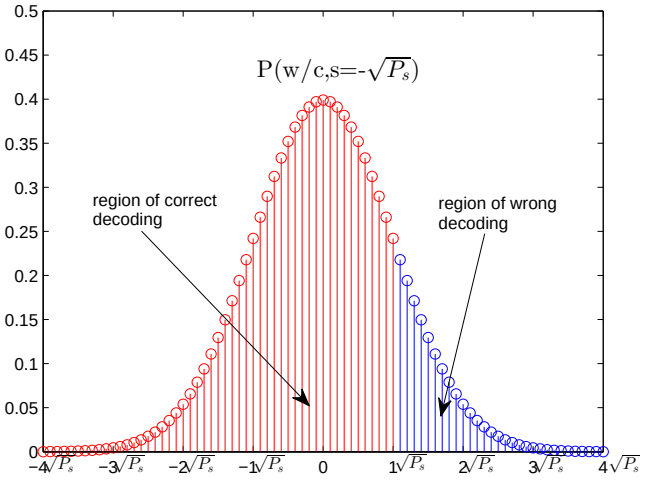

FIGURE 3.5: Distribution of noise under the hypothesis $\mathcal{H}_{00_B}$ and the wrong decoding of $s = -\sqrt{P_s} = -1$.

is sometimes decoded correctly and some other wrongly in the region where $w \geq \sqrt{\frac{\gamma P_s}{\sigma_w^2}}$ or $w \leq -\sqrt{\frac{\gamma P_s}{\sigma_w^2}}$, based on the fact if the transmitted symbol is $s = \sqrt{P_s}$ or $s = -\sqrt{P_s}$. This analysis shows that the remaining noise under $\mathcal{H}_{00_B}$ follows a truncated normal distribution [79]-[80] in the following intervals: 1) $w \leq -\sqrt{P_t}$; 2) $-\sqrt{P_t} \leq w \leq +\sqrt{P_t}$; and 3) $w \geq +\sqrt{P_t}$, where for the rest of this chapter, is is assumes that $P_t = \frac{\gamma P_s}{\sigma_w^2}$. Now, it becomes clear that we should determine what is the distribution of the sum of N truncated central and/or non-central chi-squared random variables. However, the closed form expression of this distribution is not mathematically tractable. Therefore, we should examine if the distribution of the test statistic $T(\mathbf{y}'|\mathcal{H}_{0_B})$ can be approximated by using the CLT [81].

The test statistic $T\left(\mathbf{y}'\left|\mathcal{H}_{0_B}\right.\right)$ consists of variables under one of the following cases: 1) always correct decoding; 2) always wrong decoding; and 3) sometimes correct and some other wrong decoding. The first two categories include a sequence of i.i.d random variables and hence, assuming a large number of samples the CLT can be applied. However, an independent but not identically distributed sequence is involved in the third case. Nevertheless, even in this case, the CLT can be used since the Lyapunov's and Lindeberg's conditions for non-identical variables [82] are satisfied. Thus, the mean and variance of $T\left(\mathbf{y}'\left|\mathcal{H}_{0_B}\right.\right)$ are respectively given by $\mu_{\mathcal{H}_{0B}} = (N-k)\mu_{\mathcal{H}_{00B}} + k\mu_{\mathcal{H}_{01B}}$ and $V_{\mathcal{H}_{0B}} = (N-k)V_{\mathcal{H}_{00B}} + kV_{\mathcal{H}_{01B}}$, where $\mu_{\mathcal{H}_{00_B}}$, $\mu_{\mathcal{H}_{01_B}}$, $V_{\mathcal{H}_{00_B}}$ and $V_{\mathcal{H}_{01_B}}$ are the mean and variance of the test statistic $T\left(y'\left|\mathcal{H}_{00_B}\right.\right)$ and $T\left(y'\left|\mathcal{H}_{01_B}\right.\right)$, respectively, with y' meaning only one sample. ■

Hence, the derivation of the mean and variance for $T\left(y'\left|\mathcal{H}_{00_B}\right.\right)$ and $T\left(y'\left|\mathcal{H}_{01_B}\right.\right)$ is required. However, the calculation of these parameters is obtained with the help of the following three lemmas. Lemma 3.1 is valid for all truncated central chi-squared variables, Lemma 3.2 is valid, only when the non-central chi-squared variable is truncated to the interval $[a,b]$ where $0 \leq a \leq b < \infty$, while when $b = \infty$, Lemma 3.3 is used to evaluate the truncated non-central chi-squared variable.

Lemma 3.1: The mean $\mu_c^{[a,b]}$ and variance $V_c^{[a,b]}$ of a central chi-squared variable with one degree of freedom, truncated to the interval $[a,b]$ where $0 \leq a \leq b \leq \infty$, is given by

$$\mu_c^{[a,b]} = 1 + 2\left[\frac{af_{\chi_1^2}(a) - bf_{\chi_1^2}(b)}{F_{\chi_1^2}(b) - F_{\chi_1^2}(a)}\right], \tag{3.10}$$

$$V_c^{[a,b]} = 2 - 4\left[\frac{af_{\chi_1^2}(a) - bf_{\chi_1^2}(b)}{F_{\chi_1^2}(b) - F_{\chi_1^2}(a)}\right]^2 + 2\left[\frac{a^2 f_{\chi_1^2}(a) + af_{\chi_1^2}(a) - b^2 f_{\chi_1^2}(b) - bf_{\chi_1^2}(b)}{F_{\chi_1^2}(b) - F_{\chi_1^2}(a)}\right], \tag{3.11}$$

where $F_{\chi_1^2}$ and $f_{\chi_1^2}$ denote respectively the CDF and the probability density function (PDF) of a central chi-squared variable with one degree of freedom.

Proof: Let $F_{\chi_{1T}^2}^{[a,b]}$ and $f_{\chi_{1T}^2}^{[a,b]}$ denote respectively the CDF and PDF of a central chi-squared variable with one degree of freedom, truncated to the interval $[a,b]$ where $0 \leq a \leq b \leq \infty$. For the untracated case, i.e. $a = 0$ and $b = \infty$, we drop the superscript and note only $F_{\chi_1^2}$ and $f_{\chi_1^2}$. Then, for $x \in [a,b]$, $F_{\chi_{1T}^2}^{[a,b]}(x) = \frac{F_{\chi_1^2}(x) - F_{\chi_1^2}(a)}{F_{\chi_1^2}(b) - F_{\chi_1^2}(a)}$ and $f_{\chi_{1T}^2}^{[a,b]}(x) = \frac{f_{\chi_1^2}(x)}{F_{\chi_1^2}(b) - F_{\chi_1^2}(a)}$.

According to [83], the moment generating function (MGF) for a truncated central chi-squared random variable $X \sim \chi^2_{1T}$ is given as follows:

$$M_X(t) = \left[\frac{F_{\chi^2_1}(b(1-2t)) - F_{\chi^2_1}(a(1-2t))}{F_{\chi^2_1}(b) - F_{\chi^2_1}(a)}\right](1-2t)^{-1/2}. \tag{3.12}$$

Then, the MGF can be used to calculate the mean and variance of a truncated central chi-squared variable with one degree of freedom as follows: $\mu_c^{[a,b]} = E\{X \,|a \le X \le b\} = M'_X(t)\,|_{t=0}$ and $V_c^{[a,b]} = V\{X \,|a \le X \le b\} = E\{X^2 \,|a \le X \le b\} - (E\{X \,|a \le X \le b\})^2$, where

$$\begin{aligned} &E\{X^2 \,|a \le X \le b\} = M''_X(t)\,|_{t=0} \\ &= 3 + 4\left[\frac{af_{\chi^2_1}(a) - bf_{\chi^2_1}(b)}{F_{\chi^2_1}(b) - F_{\chi^2_1}(a)}\right] + 2\left[\frac{a^2 f_{\chi^2_1}(a) + af_{\chi^2_1}(a) - b^2 f_{\chi^2_1}(b) - bf_{\chi^2_1}(b)}{F_{\chi^2_1}(b) - F_{\chi^2_1}(a)}\right]. \end{aligned} \tag{3.13}$$

■

Lemma 3.2: The mean $\mu_c^{[a,b]}$ and variance $V_c^{[a,b]}$ of a non-central chi-squared variable with one degree of freedom and non-centrality parameter λ, truncated to the interval $[a,b]$ where $0 \le a \le b < \infty$, is given by

$$\mu_{nc}^{[a,b]} = \frac{F_{\chi^2_{3,\lambda}}(b) - F_{\chi^2_{3,\lambda}}(a) + \lambda\left[F_{\chi^2_{5,\lambda}}(b) - F_{\chi^2_{5,\lambda}}(a)\right]}{F_{\chi^2_{1,\lambda}}(b) - F_{\chi^2_{1,\lambda}}(a)}, \tag{3.14}$$

$$\begin{aligned} V_{nc}^{[a,b]} = &\frac{3\left[F_{\chi^2_{5,\lambda}}(b) - F_{\chi^2_{5,\lambda}}(a)\right] + 6\lambda\left[F_{\chi^2_{7,\lambda}}(b) - F_{\chi^2_{7,\lambda}}(a)\right]}{F_{\chi^2_{1,\lambda}}(b) - F_{\chi^2_{1,\lambda}}(a)} + \frac{\lambda^2\left[F_{\chi^2_{9,\lambda}}(b) - F_{\chi^2_{9,\lambda}}(a)\right]}{F_{\chi^2_{1,\lambda}}(b) - F_{\chi^2_{1,\lambda}}(a)} \\ &- \left(\mu_{nc}^{[a,b]}\right)^2, \end{aligned} \tag{3.15}$$

where $F_{\chi^2_{1,\lambda}}$ denotes the CDF of a non-central chi-squared variable with one degree of freedom and non-centrality parameter λ.

Proof: Let $F^{[a,b]}_{\chi^2_{1T,\lambda}}$ denotes the CDF of a non-central chi-squared variable with one degree of freedom, truncated to the interval $[a,b]$ where $0 \le a \le b < \infty$ and non-centrality parameter λ. For the non-truncated case, i.e. $a = 0$ and $b = \infty$, we drop the superscript and note only $F_{\chi^2_{1,\lambda}}$. Then, for $y \in [a,b]$, $F^{[a,b]}_{\chi^2_{1T,\lambda}}(y) = \frac{F_{\chi^2_{1,\lambda}}(y) - F_{\chi^2_{1,\lambda}}(a)}{F_{\chi^2_{1,\lambda}}(b) - F_{\chi^2_{1,\lambda}}(a)}$.

According to [84], the moments of the truncated non-central chi-squared distribution can be calculated as follows

$$E\{T^i\} = \frac{h(i,p,\lambda)}{h(0,p,\lambda)}, \tag{3.16}$$

where $i \in \{0,1,2,...\}$, $h\left(0,p,\lambda\right) = F_{\chi^2_{p,\lambda}}\left(b\right) - F_{\chi^2_{p,\lambda}}\left(a\right)$ and

$$h\left(i,p,\lambda\right) = 2^i \sum_{k=0}^{i} \left(\begin{array}{c} i \\ k \end{array} \right) \left(\frac{\lambda}{2}\right)^k \frac{\Gamma\left(\frac{p}{2}+i\right)}{\Gamma\left(\frac{p}{2}+k\right)} h\left(0,p+2i+2k,\lambda\right). \tag{3.17}$$

Then, the mean and variance of a truncated non-central chi-squared variable Y with one degree of freedom is derived as follows $\mu_{nc}^{[a,b]} = E\left\{Y\left|a \le Y \le b\right.\right\} = E\left\{Y\left|a \le Y \le b\right.\right\}$ and $V_{nc}^{[a,b]} = V\left\{Y\left|a \le Y \le b\right.\right\} = E\left\{Y^2\left|a \le Y \le b\right.\right\} - \left(E\left\{Y\left|a \le Y \le b\right.\right\}\right)^2$. ■

Lemma 3.3: The mean $\mu_{nc\,\mathrm{inf}}^{[-\infty,a]}$ and $V_{nc\,\mathrm{inf}}^{[-\infty,a]}$ of a squared Gaussian variable, where the Gaussian variable is truncated to the interval $[a,\infty]$ or $[-\infty,\alpha]$, with mean μ and variance σ^2, is given by

$$\mu_{nc\,\mathrm{inf}}^{[-\infty,a]} = \mu^2 - 2\mu\sigma\frac{f_x\left(d\right)}{F_x\left(d\right)} + \sigma^2\left(1 - d\frac{f_x\left(d\right)}{F_x\left(d\right)}\right), \tag{3.18}$$

$$\begin{aligned} V_{nc\,\mathrm{inf}}^{[-\infty,a]} &= \mu^4 - 4\mu^3\sigma\frac{f_x\left(d\right)}{F_x\left(d\right)} + 6\mu^2\sigma^2\left(1 - d\frac{f_x\left(d\right)}{F_x\left(d\right)}\right) + 4\mu\sigma^3\left(-d^2\frac{f_x\left(d\right)}{F_x\left(d\right)} - 2\frac{f_x\left(d\right)}{F_x\left(d\right)}\right) \\ &+ \sigma^4\left(-d^3\frac{f_x\left(d\right)}{F_x\left(d\right)} - 3d\frac{f_x\left(d\right)}{F_x\left(d\right)} + 3\right) - \left(\mu_{nc\,\mathrm{inf}}^{[-\infty,a]}\right)^2, \end{aligned} \tag{3.19}$$

where $d = a - \mu$ and F_x, f_x denote the CDF and DPF of a normally distributed variable x.

Proof: Let $x = \mu + w$ be a normally distributed random variable with mean μ and variance σ^2, truncated to the interval $[-\infty, a]$. Then, the mean of the truncated variable x^2 is given by

$$\begin{aligned} \mu_{nc\,\mathrm{inf}}^{[-\infty,a]} &= E\left\{x^2\left|x \le a\right.\right\} = E\left\{x^2\left|x \le a\right.\right\} = E\left\{\left|\mu+w\right|^2\left|\mu+w \le a\right.\right\} = \\ &= \mu^2 + 2\mu E\left\{w\left|w \le a-\mu\right.\right\} + E\left\{w^2\left|w \le a-\mu\right.\right\}, \end{aligned} \tag{3.20}$$

while the variance is given by

$$\begin{aligned} V_{nc\,\mathrm{inf}}^{[-\infty,a]} &= V\left\{x^2\left|x \le a\right.\right\} = E\left\{x^4\left|x \le a\right.\right\} - \left(E\left\{x^2\left|x \le a\right.\right\}\right)^2 \\ &= E\left\{\left|\mu+w\right|^4\left|\mu+w \le a\right.\right\} - \left(E\left\{\left|\mu+w\right|^2\left|\mu+w \le a\right.\right\}\right)^2 \\ &= \mu^4 + 4\mu^3 E\left\{w\left|w \le a-\mu\right.\right\} + 6\mu^2 E\left\{w^2\left|w \le a-\mu\right.\right\} \\ &+ 4\mu E\left\{w^3\left|w \le a-\mu\right.\right\} + E\left\{w^4\left|w \le a-\mu\right.\right\} - \left(\mu_{nc\,\mathrm{inf}}^{[-\infty,a]}\right)^2. \end{aligned} \tag{3.21}$$

Then, according to [85], the expression of $E\left\{u^m\left|u \le a\right.\right\}$, for some fixed a is given by

$$E\left\{u^m\left|u \le a\right.\right\} = \sum_{r=0}^{m} \left(\begin{array}{c} m \\ r \end{array} \right) \mu^{m-r}\sigma^r I_r, \tag{3.22}$$

where

$$I_r = -d^{r-1}\frac{f_x(d)}{F_x(d)} + (r-1)\,I_{r-2}, \tag{3.23}$$

with the following initial conditions: i) $I_0 = 1$ and ii) $I_1 = -\frac{f_x(d)}{F_x(d)}$. Therefore, using (3.22) and (3.23) and the fact that the noise has been assumed to be Gaussian with zero mean, the first moments of the truncated distribution are derived as follows: $E\left\{w^0 \,|w \le a\right\} = I_0 = 1$, $E\left\{w^1 \,|w \le a\right\} = \sigma I_1 = -\sigma\frac{f_x(d)}{F_x(d)}$, $E\left\{w^2 \,|w \le a\right\} = \sigma^2 I_2 = \sigma^2\left(1 - d\frac{f_x(d)}{F_x(d)}\right)$, $E\left\{w^3 \,|w \le a\right\} = \sigma^3 I_3 = \sigma^3\left(-d^2\frac{f_x(d)}{F_x(d)} - 2\frac{f_x(d)}{F_x(d)}\right)$ and $E\left\{w^4 \,|w \le a\right\} = \sigma^4 I_4 = \sigma^4\left(-d^3\frac{f_x(d)}{F_x(d)} - 3d\frac{f_x(d)}{F_x(d)} + 3\right)$. Finally, using (3.20)-(3.23), the mean and variance of (3.18) and (3.19) is proven, respectively. ■

Then, with the results of Lemma 3.1, we can develop Theorem 3.2, which defines the mean $\mu_{\mathcal{H}_{00_B}}$ and variance $V_{\mathcal{H}_{00_B}}$, required for the calculation of $\mu_{\mathcal{H}_{0_B}}$ and $V_{\mathcal{H}_{0_B}}$.

Theorem 3.2: Consider a secondary user with one receive antenna, which collects a number of samples N. The SU-Rx decodes the samples, removes them from the total received signal and applies the energy detector in the remaining signal. Then, the mean and variance of $T\left(y' \,|\mathcal{H}_{00_B}\right)$ can be respectively defined as follows:

$$\mu_{\mathcal{H}_{00_B}} = \mu_c^{[0,P_t]} P_w^{\left[-\sqrt{P_t},\sqrt{P_t}\right]} + \mu_c^{[P_t,\infty]} P_w^{\left[\sqrt{P_t},\infty\right]}, \tag{3.24}$$

$$\begin{aligned} V_{\mathcal{H}_{00_B}} = {} & V_c^{[0,P_t]} P_w^{\left[-\sqrt{P_t},\sqrt{P_t}\right]} + V_c^{[P_t,\infty]} P_w^{\left[\sqrt{P_t},\infty\right]} + \left(\mu_c^{[P_t,\infty]}\right)^2 \left(1 - P_w^{\left[\sqrt{P_t},\infty\right]}\right) P_w^{\left[\sqrt{P_t},\infty\right]} \\ & + \left(\mu_c^{[0,P_t]}\right)^2 \left(1 - P_w^{\left[-\sqrt{P_t},\sqrt{P_t}\right]}\right) P_w^{\left[-\sqrt{P_t},\sqrt{P_t}\right]} - 2\mu_c^{[0,P_t]}\mu_c^{[P_t,\infty]} P_w^{\left[-\sqrt{P_t},\sqrt{P_t}\right]} P_w^{\left[\sqrt{P_t},\infty\right]}, \end{aligned} \tag{3.25}$$

where $\mu_c^{[0,P_t]}$, $V_c^{[0,P_t]}$, $\mu_c^{[P_t,\infty]}$ and $V_c^{[P_t,\infty]}$ are defined by Lemma 1, while $P_w^{\left[-\sqrt{P_t},\sqrt{P_t}\right]}$ and $P_w^{\left[\sqrt{P_t},\infty\right]}$ are expressed as follows: $P_w^{\left[-\sqrt{P_t},\sqrt{P_t}\right]} = \frac{P\left(-\sqrt{P_t} \le w \le \sqrt{P_t}\right)}{P_{c_B}} = \frac{F_y\left(\sqrt{P_t}\right) - F_y\left(-\sqrt{P_t}\right)}{P_{c_B}}$ and $P_w^{\left[\sqrt{P_t},\infty\right]} = \frac{P\left(w \ge \sqrt{P_t}\right)}{P_{c_B}} = \frac{F_y\left(-\sqrt{P_t}\right)}{P_{c_B}}$, where $F_y(\cdot)$ is the CDF of a normally distributed variable y and P_{c_B} is the probability of correct decision for BPSK [86].

Proof: The proof of (3.24) and (3.25) is described in Appendix A and B, respectively. ■

In a similar manner, following the results of Lemma 2 and 3, we develop Theorem 3.3, which defines the mean $\mu_{\mathcal{H}_{01_B}}$ and variance $V_{\mathcal{H}_{01_B}}$, required for the calculation of $\mu_{\mathcal{H}_{0_B}}$ and $V_{\mathcal{H}_{0_B}}$.

Theorem 3.3: Consider a secondary user with one receive antenna, which collects a number of samples N. The SU-Rx decodes the samples, removes them from the total received signal and applies the energy detector in the remaining signal. Then, the mean

and variance of $T\left(y'|\mathcal{H}_{01_B}\right)$ can be respectively defined as follows:

$$\mu_{\mathcal{H}_{01_B}} = \mu_{nc}^{[0,P_t]} P_w^{\left[\sqrt{P_t},3\sqrt{P_t}\right]} + \mu_{ncinf}^{\left[3\sqrt{P_t},\infty\right]} P_w^{\left[3\sqrt{P_t},\infty\right]}, \tag{3.26}$$

$$\begin{aligned} V_{\mathcal{H}_{01_B}} = \\ V_{nc}^{[0,P_t]} P_w^{\left[\sqrt{P_t},3\sqrt{P_t}\right]} + V_{ncinf}^{\left[3\sqrt{P_t},\infty\right]} P_w^{\left[3\sqrt{P_t},\infty\right]} + \left(\mu_{ncinf}^{\left[3\sqrt{P_t},\infty\right]}\right)^2 \left(1 - P_w^{\left[3\sqrt{P_t},\infty\right]}\right) P_w^{\left[3\sqrt{P_t},\infty\right]} \\ + \left(\mu_{nc}^{[0,P_t]}\right)^2 \left(1 - P_w^{\left[\sqrt{P_t},3\sqrt{P_t}\right]}\right) P_w^{\left[\sqrt{P_t},3\sqrt{P_t}\right]} - 2\mu_{nc}^{[0,P_t]} \mu_{ncinf}^{\left[3\sqrt{P_t},\infty\right]} P_w^{\left[\sqrt{P_t},3\sqrt{P_t},\right]} P_w^{\left[3\sqrt{P_t},\infty\right]}, \end{aligned} \tag{3.27}$$

where $P_w^{\left[\sqrt{P_t},3\sqrt{P_t}\right]} = \frac{P\left(\sqrt{P_t}\le w\le 3\sqrt{P_t}\right)}{P_{\text{c\_B}}} = \frac{F_x\left(3\sqrt{P_t}\right) - F_x\left(\sqrt{P_t}\right)}{P_{\text{c\_B}}}$, $P_w^{\left[3\sqrt{P_t},\infty\right]} = \frac{P\left(w\ge 3\sqrt{P_t}\right)}{P_{\text{c\_B}}} = \frac{F_x\left(-3\sqrt{P_t}\right)}{P_{\text{c\_B}}}$ and $\mu_{nc}^{[0,P_t]}$, $V_{nc}^{[0,P_t]}$, $\mu_{ncinf}^{[P_t,\infty]}$, $V_{ncinf}^{[P_t,\infty]}$ are defined by Lemma 2 and Lemma 3.

Proof: The proof of (3.26) and (3.27) is similar to that presented in Appendix A and B. ■

Therefore, all the parameters of (3.7) have been derived. However, as mentioned, the required condition for the evaluation of the detector is the proper calculation of the detection threshold ε, which is significantly complex through (3.7), particularly as N increases. For this reason, an approximated expression for the probability of false alarm is derived in this chapter as follows:

$$P_{FA_{B_{apr}}} = Q\left(\frac{\varepsilon - N\left(1 - P_{e_B}\right)\mu_{\mathcal{H}_{00_B}} - NP_{e_B}\mu_{\mathcal{H}_{01_B}}}{\sqrt{N\left(1 - P_{e_B}\right)V_{\mathcal{H}_{00_B}} + NP_{e_B}V_{\mathcal{H}_{01_B}}}}\right), \tag{3.28}$$

where the index B_{apr} denotes approximation under the BPSK scenario. This equation simplifies (3.7), based on the fact that for a large number of samples, the expected number of correct and wrong decoded bits can be approximated with the help of the probability of correct $(1 - P_{e_B})$ and wrong bits P_{e_B}, respectively. Now, according to (3.28) the computation of ε requires the inverse Q function which can be computed directly in most of the mathematical software packages.

3.3.2 Probability of False Alarm for QPSK Signals

In this subsection, the P_{FA} under the QPSK scenario is derived. Applying the algorithm proposed in Section 3.2 under the QPSK scenario, the hypothesis test of (3.1) can be

reformulated as follows:

$$\mathcal{H}_{0_Q}: \begin{cases} \mathcal{H}_{00_Q}: y(n) = \mathcal{R}\{w(n)\} + \mathcal{I}\{w(n)\}, \\ \mathcal{H}_{01_Q}: y(n) = 2h\mathcal{R}\{s(n)\} + \mathcal{R}\{w(n)\} + \mathcal{I}\{w(n)\}, \\ \mathcal{H}_{02_Q}: y(n) = 2h\mathcal{I}\{s(n)\} + \mathcal{R}\{w(n)\} + \mathcal{I}\{w(n)\}, \\ \mathcal{H}_{03_Q}: y(n) = 2h\mathcal{R}\{s(n)\} + 2h\mathcal{I}\{s(n)\} + \mathcal{R}\{w(n)\} + \mathcal{I}\{w(n)\}, \end{cases} \tag{3.29}$$

where $n = 0, 1, ..., N-1$, the index Q corresponds to the QPSK scenario, the hypothesis $\mathcal{H}_{00_Q}$ represents the case that the received signal is decoded correctly, while the hypotheses $\mathcal{H}_{01_Q}$, $\mathcal{H}_{02_Q}$ and $\mathcal{H}_{03_Q}$ correspond to the wrong decoding case ans more specifically: 1) $\mathcal{H}_{01_Q}$: the real part is decoded wrongly and the imaginary part is correctly decoded; 2) $\mathcal{H}_{02_Q}$: the real part is correctly decoded and the imaginary part is wrongly decoded; and 3) $\mathcal{H}_{03_Q}$: both the real and imaginary part are wrongly decoded.

Based on Theorem 1, for the derivation of the probability of false alarm under the BPSK scenario, the extension to QPSK case is straightforward and it is given as follows

$$P_{FA_Q} = \sum_{k=0}^{2N} \binom{2N}{k} P_{k_Q} P_{e_Q}^k \left(1 - P_{e_Q}\right)^{2N-k}, \tag{3.30}$$

where $P_{k_Q} = P_{k_B}$ and P_{e_Q} is the probability of bit error for QPSK, same as for BPSK, namely $P_{e_Q} = P_{e_B}$, while the factor 2 is due to the fact that a QPSK signal consists of two orthogonal BPSK ones. Furthermore, the corresponding approximated $P_{FA_{Q_{apr}}}$ is given by

$$P_{FA_{Q_{apr}}} = Q\left(\frac{\varepsilon - N\left(1-P_{e_Q}\right)^2 \mu_{\mathcal{H}_{00_Q}} - N\left(1-P_{e_Q}\right) P_{e_Q}\left(\mu_{\mathcal{H}_{01_Q}} + \mu_{\mathcal{H}_{02_Q}}\right) - N P_{e_Q}^2 \mu_{\mathcal{H}_{03_Q}}}{\sqrt{N\left(1-P_{e_Q}\right)^2 V_{\mathcal{H}_{00_Q}} + N\left(1-P_{e_Q}\right) P_{e_Q}\left(V_{\mathcal{H}_{01_Q}} + V_{\mathcal{H}_{02_Q}}\right) + N P_{e_Q}^2 V_{\mathcal{H}_{03_Q}}}}\right), \tag{3.31}$$

where $\mu_{\mathcal{H}_{00_Q}} = 2\mu_{\mathcal{H}_{00_B}}$ and $V_{\mathcal{H}_{00_Q}} = 2V_{\mathcal{H}_{00_B}}$ because both the real and imaginary part follow a truncated central chi-squared distribution, $\mu_{\mathcal{H}_{01_Q}} = \mu_{\mathcal{H}_{00_B}} + \mu_{\mathcal{H}_{01_B}}$ and $V_{\mathcal{H}_{01_Q}} = V_{\mathcal{H}_{00_B}} + V_{\mathcal{H}_{01_B}}$, because the real part follows a truncated non-central chi-squared distribution, while the imaginary part follows a truncated central chi-squared distribution, $\mu_{\mathcal{H}_{02_Q}} = \mu_{\mathcal{H}_{00_B}} + \mu_{\mathcal{H}_{01_B}}$ and $V_{\mathcal{H}_{02_Q}} = V_{\mathcal{H}_{00_B}} + V_{\mathcal{H}_{01_B}}$, because the real part follows a truncated central chi-squared distribution, while the imaginary part follows a truncated non-central chi-squared distribution and finally, $\mu_{\mathcal{H}_{03_Q}} = 2\mu_{\mathcal{H}_{01_B}}$ and $V_{\mathcal{H}_{03_Q}} = 2V_{\mathcal{H}_{01_B}}$, because both the real and imaginary part follow a truncated non-central chi-squared distribution.

3.3.3 Probability of detection

In this subsection, the probability of detection assuming that the primary signal follows a Gaussian distribution with zero mean and variance σ_{PU}^2 is derived. This is a valid assumption, e.g. with an OFDM (orthogonal frequency division multiplexing) signal, where independent data streams are used for the modulation of each carrier [87]. Furthermore, it is customary to assume that x_p is Gaussian-distributed, because the modulation and generally the symbols of the primary user are unknown [11]. Similar signal modeling is frequently used in cognitive radio literature, e.g. [46], [88], [89]. Therefore, under the scenario that the SU signal is BPSK modulated, the theoretical expression for the P_D is also given by (3.28) by substituting σ_w^2 with $\sigma_w^2 + \sigma_{PU}^2$ in the related parts. Specifically, the P_D is given by

$$P_{D_{B_{apr}}} = Q\left(\frac{\varepsilon - N\left(1 - P'_{e_B}\right)\mu_{\mathcal{H}_{10_B}} - NP'_{e_B}\mu_{\mathcal{H}_{11_B}}}{\sqrt{N\left(1 - P'_{e_B}\right)V_{\mathcal{H}_{10_B}} + NP'_{e_B}V_{\mathcal{H}_{11_B}}}}\right), \tag{3.32}$$

where the mean $\mu_{\mathcal{H}_{10_B}}$, $\mu_{\mathcal{H}_{11_B}}$ and variance $V_{\mathcal{H}_{10_B}}$, $V_{\mathcal{H}_{11_B}}$ are defined by (3.24), (3.25), (3.26) and (3.27), respectively, with the difference being that now, the probability of bit error and the interval of interest are not anymore related to $P_{e_B} = Q\left(\sqrt{\frac{\gamma P_s}{\sigma_w^2}}\right)$ and $P_t = \frac{\gamma P_s}{\sigma_w^2 + \sigma_{PU}^2}$, but they are based on the following parameters: $P'_{e_B} = Q\left(\sqrt{\frac{\gamma P_s}{\sigma_w^2 + \sigma_{PU}^2}}\right)$, $P_d = \frac{\gamma P_s}{\sigma_w^2 + \sigma_{PU}^2}$. Similarly, the P_D under the scenario that the SU signal is QPSK modulated is given by (3.31) by substituting again σ_w^2 with $\sigma_w^2 + \sigma_{PU}^2$ in the related parts.

As mentioned, in this chapter, the P_D under the assumption that the primary signal is Gaussian-distributed is derived. Deriving the P_D for the case that the primary signal has different distribution is a valuable idea for future studies.

3.4 Probability of False Alarm for M-QAM

The previous section discussed the derivation of the P_{FA} and P_D under the BPSK and QPSK scenarios. However, in this section, the work is generalized to higher modulation schemes, and particularly, the P_{FA} for M-QAM modulated signals is examined. The derivation of the P_D is straightforward as in Section 3.3. Furthermore, it should be noted that here the focus is on the derivation of the approximated P_{FA}, because as mentioned earlier, the calculation of the detection threshold ε through the accurate P_{FA} is complicated, especially as N increases and the situation becomes more complex under the M-QAM scenario due to the fact that under the wrong decoding case the estimated symbol can be anyone of $M - 1$ possible symbols.

The approximated probability of false alarm for the M-QAM case ($P_{FA_{M-Qapr}}$) is defined by

$$P_{FA_{M-Qapr}} = Q\left(\frac{\varepsilon - N\sum_{k=1}^{M}\sum_{t=1}^{M} P\left(s=s_k\right)P\left(\hat{s}=s_t\,|s=s_k\right)\mu_{\mathcal{H}_{0,k,t}}}{\sqrt{N\sum_{k=1}^{M}\sum_{t=1}^{M} P\left(s=s_k\right)P\left(\hat{s}=s_t\,|s=s_k\right)V_{\mathcal{H}_{0,k,t}}}}\right), \tag{3.33}$$

where s_k denotes the transmitted symbol, s_t denotes the estimated symbol, while $\mu_{\mathcal{H}_{0,k,t}}$ and $V_{\mathcal{H}_{0,k,t}}$ represent, respectively, the mean and variance of the test statistic of (3.6) under each case of correct or wrong decoding under $\mathcal{H}_0$ hypothesis, expressed as follows:

$$\mu_{\mathcal{H}_{0,k,t}} = \mu_{\frac{\mathcal{R}\{s_k\}-\mathcal{R}\{s_t\}}{\sqrt{P_s}}} + \mu_{\frac{\mathcal{I}\{s_k\}-\mathcal{I}\{s_t\}}{\sqrt{P_s}}}, \tag{3.34}$$

$$V_{\mathcal{H}_{0,k,t}} = V_{\frac{\mathcal{R}\{s_k\}-\mathcal{R}\{s_t\}}{\sqrt{P_s}}} + V_{\frac{\mathcal{I}\{s_k\}-\mathcal{I}\{s_t\}}{\sqrt{P_s}}}, \tag{3.35}$$

where $\mu_{\frac{\mathcal{R}\{s_k\}-\mathcal{R}\{s_t\}}{\sqrt{P_s}}}$, $\mu_{\frac{\mathcal{I}\{s_k\}-\mathcal{I}\{s_t\}}{\sqrt{P_s}}}$, $V_{\frac{\mathcal{R}\{s_k\}-\mathcal{R}\{s_t\}}{\sqrt{P_s}}}$, $V_{\frac{\mathcal{I}\{s_k\}-\mathcal{I}\{s_t\}}{\sqrt{P_s}}}$, are derived by Theorems 3.4 and 3.5.

For the case of correct decoding, namely when $k = t$, it is obvious that (3.34) and (3.35) are expressed as follows: $\mu_{\mathcal{H}_{0,k,t}} = \mu_0 + \mu_0$ and $V_{\mathcal{H}_{0,k,t}} = V_0 + V_0$. Therefore, the derivation of the mean and variance under the scenario of correct decoding for M-QAM signals is required and it is given by Theorem 3.4.

Theorem 3.4: Consider a secondary user with one receive antenna, which collects a number of samples N. The SU-Rx decodes the samples, removes them from the total received signal and applies the energy detector in the remaining signal. Then, the mean and variance of $T\left(y'\,|\mathcal{H}_{0,k=t,t=k}\right)$ can be respectively defined as follows:

$$\mu_{\mathcal{H}_{0,k=t,t=k}} = 2\mu_0 = E\left\{\left|y'\right|^2|\mathcal{H}_{0,k=t,t=k}\right\} = 2E\left\{\mathcal{R}^2\left\{y'\right\}|0 \le \mathcal{R}^2\left\{w\right\} \le P_t\right\}P_1 + 2\frac{2}{\sqrt{M}}E\left\{\mathcal{R}^2\left\{y'\right\}\left|\mathcal{R}^2\left\{w\right\} \ge P_t\right.\right\}P_2, \tag{3.36}$$

$$\begin{aligned} V_{\mathcal{H}_{0,k=t,t=k}} &= 2V_0 = V\left\{\left|y'\right|^2|\mathcal{H}_{0,k=t,t=k}\right\} \\ &= 2V\left\{\mathcal{R}^2\left\{y'\right\}|0 \le \mathcal{R}^2\left\{w\right\} \le P_t\right\}P_1 + 2\frac{2}{\sqrt{M}}V\left\{\mathcal{R}^2\left\{y'\right\}\left|\mathcal{R}^2\left\{w\right\} \ge P_t\right.\right\}P_2 \\ &+ 2\left(E\left\{\mathcal{R}^2\left\{y'\right\}|0 \le \mathcal{R}^2\left\{w\right\} \le P_t\right\}\right)^2P_1P_2 + 2\frac{2}{\sqrt{M}}\left(E\left\{\mathcal{R}^2\left\{y'\right\}\left|\mathcal{R}^2\left\{w\right\} \ge P_t\right.\right\}\right)^2P_1P_2 \\ &- 2\frac{4}{\sqrt{M}}E\left\{\mathcal{R}^2\left\{y'\right\}|0 \le \mathcal{R}^2\left\{w\right\} \le P_t\right\}E\left\{\mathcal{R}^2\left\{y'\right\}\left|\mathcal{R}^2\left\{w\right\} \ge P_t\right.\right\}P_1P_2, \end{aligned} \tag{3.37}$$

where $\mathcal{H}_{0,k=t,t=k}$ represents the case of correct decoding for M-QAM signals under $\mathcal{H}_0$ hypothesis, M denotes the size of the constellation, $P_{\mathrm{c_{M-Q}}}$ corresponds to the probability of correct symbol for M-QAM modulation [45] and P_1, P_2 are respectively obtained as follows:

$$\begin{aligned} P_1 &= P\left(-\sqrt{P_t} \leq \mathcal{R}\left\{w\right\} \leq \sqrt{P_t}\right) \left[\begin{array}{c} P\left(-\sqrt{P_t} \leq \mathcal{I}\left\{w\right\} \leq \sqrt{P_t}\right) + \\ +2P\left(\mathcal{I}\left\{w\right\} \geq \sqrt{P_t}\right)/\sqrt{M} \end{array}\right] \Big/ P_{\mathrm{c\_M-Q}}, \\ P_2 &= P\left(\mathcal{R}\left\{w\right\} \geq \sqrt{P_t}\right) \left[\begin{array}{c} P\left(-\sqrt{P_t} \leq \mathcal{I}\left\{w\right\} \leq \sqrt{P_t}\right) + \\ +2P\left(\mathcal{I}\left\{w\right\} \geq \sqrt{P_t}\right)/\sqrt{M} \end{array}\right] \Big/ P_{\mathrm{c_{M-Q}}}\,. \end{aligned} \tag{3.38}$$

Proof: The proof of (3.36) is presented in Appendix C, while the proof of (3.37) is similar to that of (3.36). ■

Furthermore, the derivation of the mean and variance under the scenario of wrong decoding for M-QAM signals is necessary and it is given by Theorem 3.5.

Theorem 3.5: Consider a secondary user with one receive antenna, which collects a number of samples N. The SU-Rx decodes the samples, removes them from the total received signal and applies the energy detector in the remaining signal. Then, the mean and variance of $T\left(y'\left|\mathcal{H}_{0,\mathrm{k\neq t,t\neq k}}\right.\right)$ are defined by (3.34) and (3.35), respectively, where $\mu_{\frac{\mathcal{R}\{s_k\}-\mathcal{R}\{s_t\}}{\sqrt{P_s}}} = \mu_{2l}$ and $V_{\frac{\mathcal{R}\{s_k\}-\mathcal{R}\{s_t\}}{\sqrt{P_s}}} = V_{2l}$ with $l = 1 - \frac{\sqrt{M}}{1}, ..., \sqrt{M} - 1$. The same range is also valid for $\mu_{\frac{\mathcal{I}\{s_k\}-\mathcal{I}\{s_t\}}{\sqrt{P_s}}}$ and $V_{\frac{\mathcal{I}\{s_k\}-\mathcal{I}\{s_t\}}{\sqrt{P_s}}}$. More specifically the mean μ_{2l}, for the whole range, is derived as follows:

$$\begin{aligned} \mu_{2r} = &\left(1 + \tfrac{2r}{\sqrt{M}}\right) E\left\{\left|\mathcal{R}\left\{y'\right\}\right|^2 \left| 0 \leq \left|2r\sqrt{P_t} + \mathcal{R}\left\{w\right\}\right|^2 \leq P_t \right\} P_3 \\ &+ \tfrac{2}{\sqrt{M}} E\left\{\left|\mathcal{R}\left\{y'\right\}\right|^2 \left| \left|2r\sqrt{P_t} + \mathcal{R}\left\{w\right\}\right|^2 \geq P_t \right\} P_4 \end{aligned} \qquad r = 1 - \frac{\sqrt{M}}{2}, ..., -1, \tag{3.39}$$

$$\mu_{2d} = E\left\{\left|2d\sqrt{P_t} + \mathcal{R}\left\{w\right\}\right|^2 \left| 0 \leq \left|2d\sqrt{P_t} + \mathcal{R}\left\{w\right\}\right|^2 \leq P_t \right\} P_5 \quad d = 1, ..., \frac{\sqrt{M}}{2} - 1, \tag{3.40}$$

$$\begin{aligned} \mu_{2f} = &E\left\{\left|\mathcal{R}\left\{y'\right\}\right|^2 \left| 0 \leq \left|2f\sqrt{P_t} + \mathcal{R}\left\{w\right\}\right|^2 \leq P_t \right\} P_6 \\ &+ \tfrac{2}{\sqrt{M}} E\left\{\left|\mathcal{R}\left\{y'\right\}\right|^2 \left| \left|2f\sqrt{P_t} + \mathcal{R}\left\{w\right\}\right|^2 \geq P_t \right\} P_7 \end{aligned} \qquad f = \frac{\sqrt{M}}{2}, \tag{3.41}$$

$$\begin{aligned} \mu_{2q} = &\left(2 - \tfrac{2q}{\sqrt{M}}\right) E\left\{\left|\mathcal{R}\left\{y'\right\}\right|^2 \left| 0 \leq \left|2q\sqrt{P_t} + \mathcal{R}\left\{w\right\}\right|^2 \leq P_t \right\} P_8 \\ &+ \tfrac{2}{\sqrt{M}} E\left\{\left|\mathcal{R}\left\{y'\right\}\right|^2 \left| \left|2q\sqrt{P_t} + \mathcal{R}\left\{w\right\}\right|^2 \geq P_t \right\} P_9 \end{aligned} \qquad q = \frac{\sqrt{M}}{2} + 1, ..., \sqrt{M} - 1, \tag{3.42}$$

while the variance V_{2r} is obtained as follows:

$$\begin{aligned}
V_{2r} = & \left(1+\tfrac{2r}{\sqrt{M}}\right) V\left\{|\mathcal{R}\{y'\}|^2 \left| 0 \le \left|2r\sqrt{P_t}+\mathcal{R}\{w\}\right|^2 \le P_t \right.\right\} P_3 \\
& + \tfrac{2}{\sqrt{M}} V\left\{|\mathcal{R}\{y'\}|^2 \left| \left|2r\sqrt{P_t}+\mathcal{R}\{w\}\right|^2 \ge P_t \right.\right\} P_4 \\
& + \left(1+\tfrac{2r}{\sqrt{M}}\right)\left(E\left\{|\mathcal{R}\{y'\}|^2 \left| 0 \le \left|2r\sqrt{P_t}+\mathcal{R}\{w\}\right|^2 \le P_t \right.\right\}\right)^2 P_3P_4 \\
& + \tfrac{2}{\sqrt{M}}\left(E\left\{|\mathcal{R}\{y'\}|^2 \left| \left|2r\sqrt{P_t}+\mathcal{R}\{w\}\right|^2 \ge P_t \right.\right\}\right)^2 P_3P_4 \\
& - 2\left(1+\tfrac{2r}{\sqrt{M}}\right)\tfrac{2}{\sqrt{M}} E\left\{|\mathcal{R}\{y'\}|^2 \left| 0 \le \left|2r\sqrt{P_t}+\mathcal{R}\{w\}\right|^2 \le P_t \right.\right\} \\
& \times E\left\{|\mathcal{R}\{y'\}|^2 \left| \left|2r\sqrt{P_t}+\mathcal{R}\{w\}\right|^2 \ge P_t \right.\right\} P_3P_4
\end{aligned} \qquad r = 1-\frac{\sqrt{M}}{2}, ..., -1, \tag{3.43}$$

where the probabilities $P_3, P_4, P_5, P_6, P_7, P_8$ and P_9 are given by

$$\begin{aligned}
P_3 &= P\left(-\sqrt{P_t}-2r\sqrt{P_t} \le \mathcal{R}\{w\} \le \sqrt{P_t}-2r\sqrt{P_t}\right)/P_{w_{M-Q}}, \\
P_4 &= P\left(\mathcal{R}\{w\} \ge \sqrt{P_t}-2r\sqrt{P_t}\right)/P_{w_{M-Q}}, \\
P_5 &= P\left(-\sqrt{P_t}-2d\sqrt{P_t} \le \mathcal{R}\{w\} \le \sqrt{P_t}-2d\sqrt{P_t}\right)/P_{w_{M-Q}}/P_{w_{M-Q}}, \\
P_6 &= P\left(-\sqrt{P_t}-2f\sqrt{P_t} \le \mathcal{R}\{w\} \le \sqrt{P_t}-2f\sqrt{P_t}\right)/P_{w_{M-Q}}, \\
P_7 &= P\left(\mathcal{R}\{w\} \ge \sqrt{P_t}-2f\sqrt{P_t}\right)/P_{w_{M-Q}}, \\
P_8 &= P\left(-\sqrt{P_t}-2q\sqrt{P_t} \le \mathcal{R}\{w\} \le \sqrt{P_t}-2q\sqrt{P_t}\right)/P_{w_{M-Q}}, \\
P_9 &= P\left(\mathcal{R}\{w\} \ge \sqrt{P_t}-2q\sqrt{P_t}\right)/P_{w_{M-Q}},
\end{aligned} \tag{3.44}$$

while $\mathcal{H}_{0,k\neq t,t\neq k}$ represents the case of wrong decoding for M-QAM signals under $\mathcal{H}_0$ hypothesis and $P_{w_{M-Q}}$ denotes the probability of wrong symbol detection for M-QAM modulation [45]. Finally, it should be mentioned that the derivation of the variances V_{2d}, V_{2f} and V_{2q} can be defined following the same methodology as for (3.43).

Proof: The proof of Theorem 3.5 is presented in Appendix D. ■

3.5 Numerical Results

In this section, simulation results are presented in order to 1) verify the derived expressions of (3.28), (3.31) and (3.33) for the P_{FA}; 2) compare our proposed system with the conventional one in terms of the throughput; 3) evaluate the detection reliability of the "energy detector with imperfect signal cancellation (EDISC)" for the case of perfect channel estimation; and 4) examine the P_D of our proposed method taking into account the channel estimation error.

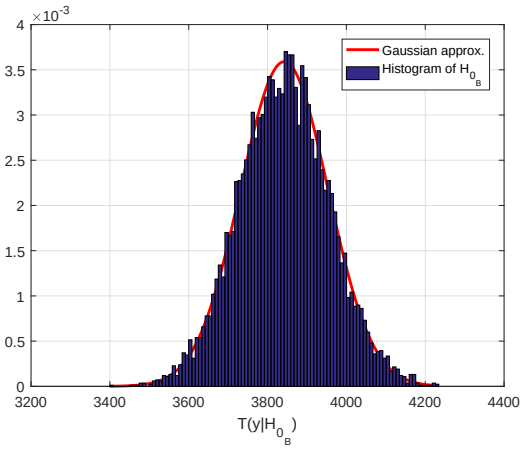

FIGURE 3.6: Theoretical and empirical distributions of $T(\mathbf{y}|\mathcal{H}_{0_B})$ with $N = 2000$, $E_s = 10$ dB and $\sigma_w^2 = 2$ dB.

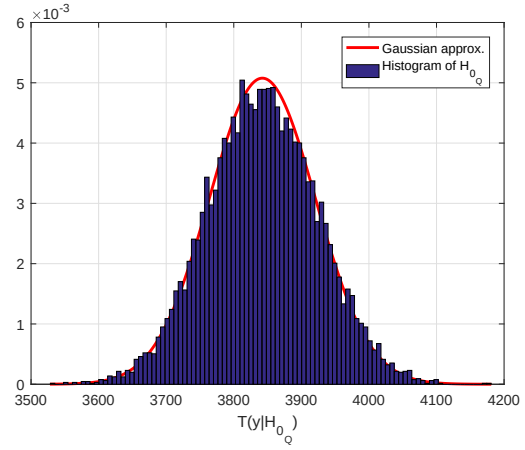

FIGURE 3.7: Theoretical and empirical distributions of $T\left(\mathbf{y}|\mathcal{H}_{0_Q}\right)$ with $N = 2000$, $E_s = 10$ dB and $\sigma_w^2 = 2$ dB.

3.5.1 Evaluation of the probability of false alarm

It should be mentioned that under the assumption of a large number of samples N and the use of the CLT, the relationship between the P_{FA} and the corresponding distribution of the test statistic is the following: $T(\mathbf{y}) \sim \mathcal{N}(\mu, V) \Rightarrow P_{FA} = Q\left(\frac{\varepsilon-\mu}{\sqrt{V}}\right)$, where $\mathcal{N}(\mu, V)$ denotes a Gaussian distribution with mean μ and variance V. Therefore, the verification of the P_{FA} under the BPSK (3.28), QPSK (3.31) and M-QAM (3.33) scenarios can be obtained through the verification of the distribution of the test statistic under the BPSK ($T(\mathbf{y}|\mathcal{H}_{0_B})$), QPSK ($T\left(\mathbf{y}|\mathcal{H}_{0_Q}\right)$) and 16-QAM ($T\left(\mathbf{y}|\mathcal{H}_{0_{16-QAM}}\right)$) scenarios. The distribution of $T(\mathbf{y}|\mathcal{H}_{0_B})$ is given by

$$T(\mathbf{y}|\mathcal{H}_{0_B}) \sim \mathcal{N}\left(N(1-P_{e_B})\mu_{\mathcal{H}_{00_B}} + NP_{e_B}\mu_{\mathcal{H}_{01_B}}, N(1-P_{e_B})V_{\mathcal{H}_{00_B}} + NP_{e_B}V_{\mathcal{H}_{01_B}}\right). \tag{3.45}$$

With similar manner, the distribution of $T\left(\mathbf{y}|\mathcal{H}_{0_Q}\right)$ and $T\left(\mathbf{y}|\mathcal{H}_{0_{16-QAM}}\right)$ can be derived.

Figures 3.6, 3.7 and 3.8 depict the histogram obtained from 10000 Monte-Carlo realizations of $T\left(\mathbf{y}|\mathcal{H}_{0_B}\right)$, $T\left(\mathbf{y}|\mathcal{H}_{0_Q}\right)$ and $T\left(\mathbf{y}|\mathcal{H}_{0_{16-QAM}}\right)$, respectively, where the number of measurement samples is set to $N = 2000$. In this figure, it is shown that the CLT provides good approximation for the distribution of $T\left(\mathbf{y}|\mathcal{H}_{0_B}\right)$, $T\left(\mathbf{y}|\mathcal{H}_{0_Q}\right)$ and $T\left(\mathbf{y}|\mathcal{H}_{0_{16-QAM}}\right)$, verifying with this way the Gaussian approximations of (3.28), (3.31) and (3.33) for the P_{FA}.

3.5.2 Performance analysis with respect to throughput

In this subsection, the proposed scheme is compared with te conventional one in terms of the average achievable throughput. Following the same model as in [20], the same approach for the evaluation of the throughput can be used, replacing the P_{FA} and P_D under the case of perfect signal cancellation with the deriving expressions for the P_{FA} and P_D under the case of imperfect signal cancellation. For conciseness, the readers can be referred to [20] for the details of the throughput derivation. The frame duration is $T = 100$ ms, the sampling frequency $f = 6$ MHz and for both cases, a target probability of detection $P_D = 0.9$ is assumed, while the secondary transmit and primary received SNR are considered as $SNR_{SU} = 7$ dB and $SNR_{PU} = -20$ dB.

Figure 3.9 depicts the average achievable throughput versus the sensing time τ, where it is obvious that the proposed cognitive radio systems exhibits higher average achievable throughput than the conventional one despite the fact of considering imperfect signal cancellation.

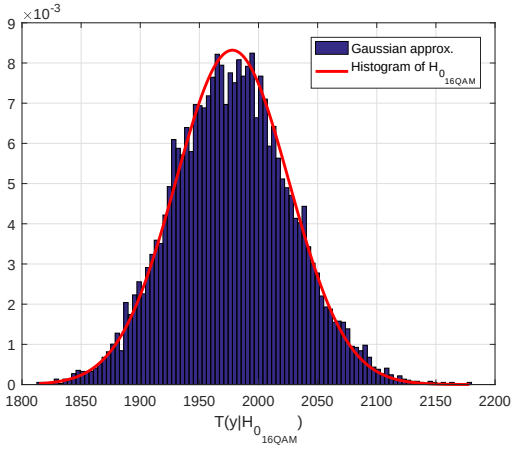

FIGURE 3.8: Theoretical and empirical distributions of $T\left(\mathbf{y}|\mathcal{H}_{0_{16-QAM}}\right)$ with $N = 2000$, $E_s = 10$ dB and $\sigma_w^2 = 2$ dB.

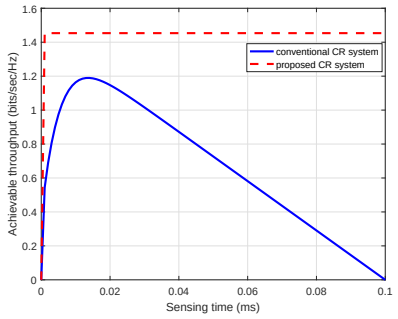

(A) Probability of PU being active $P(\mathcal{H}_0) = 0.5$.

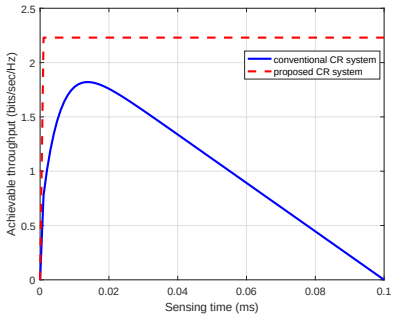

(B) Probability of PU being active $P(\mathcal{H}_0) = 0.8$.

FIGURE 3.9: Average achievable throughput of the proposed and conventional cognitive radio system versus the sensing time with secondary transmit SNR, $SNR_{SU} = 7dB$, received primary SNR, $SNR_{PU} = -20$ dB and target detection probability $P_D = 0.9$.

3.5.3 Performance analysis with respect to probability of detection

In this chapter, the PU is assumed being either absent or present for a long period as in fixed networks, e.g. TV channels and backhaul networks. Therefore, in this section, simulation results are presented to analyze the detection reliability of the EDISC for the frame that the simultaneous spectrum sensing and data transmission takes place. This scheme is compared with the "energy detector with perfect signal cancellation (EDPSC)" as proposed in [20] and with the case that the SU-Rx informs the SU-Tx about the status of the PU by using a CED as given by (5) in [25], where there is no need for decoding, and hence signal cancellation. For simplicity, it is assumed that the PU follows a Gaussian distribution with zero mean and variance σ^2_{PU}, while the transmitted signal from the SU-TX is BPSK, QPSK, 16-QAM or 64-QAM modulated. Furthermore, the channel is assumed to be of unit power, the probability of false alarm is set to $P_{FA} = 0.1$, while the received PU signal-to-interference plus noise ratio at the SU-Rx ($SINR_{PU} = \frac{\sigma^2_{PU}}{P_s+\sigma^2_w}$) varies from -25 to 5 dB. Here, it should be mentioned that by saying interference, the presence of the SU-Tx is meant.

Figures 3.10, 3.11, 3.12 and 3.13 depict the P_D as a function of the SINR of the PU comparing the aforementioned three techniques: 1) CED; 2) EDPSC; and 3) EDISC. The number of samples is set $N = 100$ and it is observed that the proposed detection scheme provides significantly better detection performance than the CED for all the cases. Furthermore, it is observed that the EDISC approaches the detection performance of the EDPSC performing slightly worse, under the BPSK and QPSK scenario, while it presents inferior performance for 16-QAM and 64-QAM compared to ones for BPSK/QPSK, but still better. This can be explained by the fact that our technique considers a more realistic scenario taking into account the decoding errors and the probability of correct decision deteriorates as higher order constellations (especially for low

SINR values) are employed. Moreover, Figures 3.10 and 3.11 show that the performance of the P_D based on the calculated decision threshold related to the approximated P_{FA} (i.e. (3.28) and (3.31) for Figure 3.10 and Figure 3.11, respectively) is very close to the P_D based on the calculated decision threshold related to the more accurate P_{FA} (i.e. (3.7) and (3.30) for Figure 3.10 and Figure 3.11, respectively), validating the reliability of (3.28) and (3.31), respectively.

Finally, from Figure 3.14 is observed that the difference in the detection performance between the simulation and approximated results decreases as the number of samples increases. The reason is that the theoretical approximated expression is based on the CLT which requires a large number of samples for better reliability.

3.5.4 Performance analysis with respect to channel estimation error

In the following experiment, the performance of the EDISC with respect to the channel uncertainty under the BPSK case is evaluated. The estimated channel $\hat{h}$ can be modeled as $\hat{h} = h + \epsilon$, where the channel estimation error ϵ follows a Gaussian distribution with zero mean and variance σ_ϵ^2 [25], [90]. Therefore, in the simulations, the channel estimation error varies in each realization.

Figure 3.15 depicts the P_D as a function of the SINR of the PU for the BPSK case considering imperfect channel estimation. This figure shows that the channel uncertainty degrades the detection performance of the EDISC. Furthermore, it is shown that when the channel estimation is more accurate $\sigma_\epsilon^2 = 0.002$, the effect of the channel estimation error reduces, but our detector, still, performs well for moderate channel uncertainty $\sigma_\epsilon^2 = 0.02$.

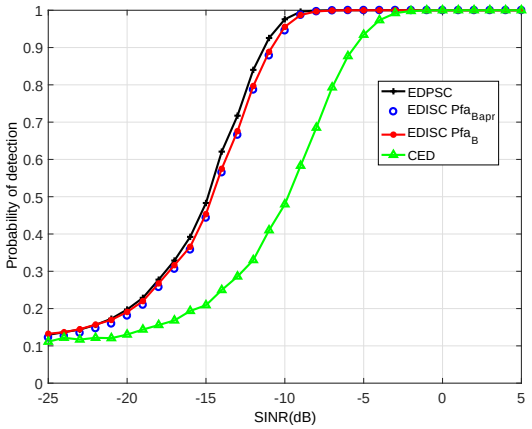

FIGURE 3.10: P_D versus the SINR of the PU, under the BPSK scenario, for $N = 100$, $E_s = 10$ dB and $\sigma_w^2 = 2$ dB.

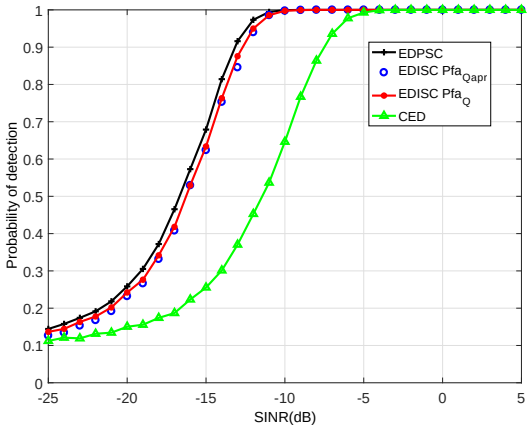

FIGURE 3.11: P_D versus the SINR of the PU, under the QPSK scenario, for $N = 100$, $E_s = 10$ dB and $\sigma_w^2 = 2$ dB.

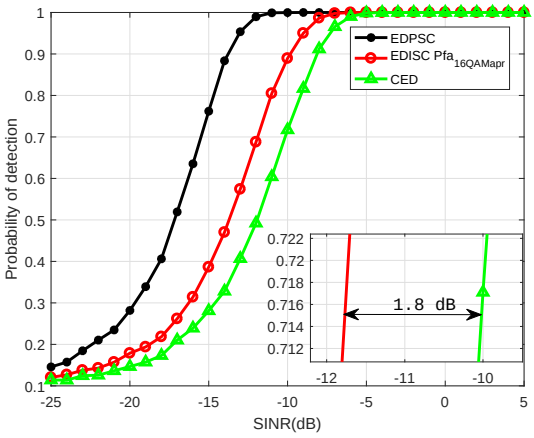

FIGURE 3.12: P_D versus the SINR of the PU, under the 16-QAM scenario, for $N = 100$, $E_s = 10$ dB and $\sigma_w^2 = 2$ dB.

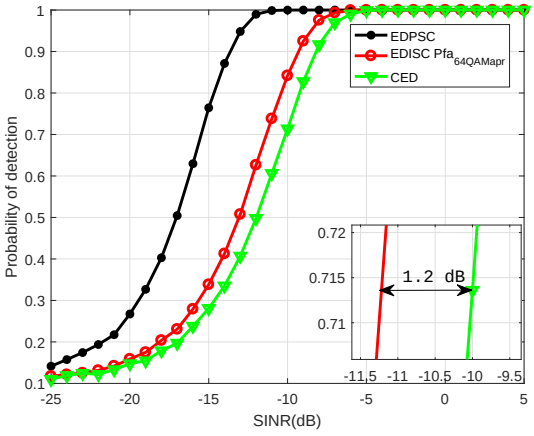

FIGURE 3.13: P_D versus the SINR of the PU, under the 64-QAM scenario, for $N = 100$, $E_s = 10$ dB and $\sigma_w^2 = 2$ dB.

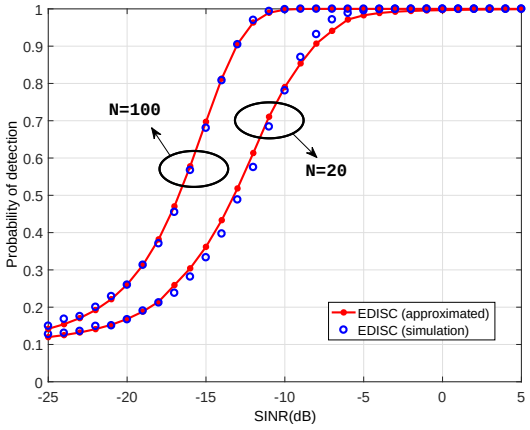

FIGURE 3.14: Comparison between the approximated and simulated performance for the proposed ED, under the QPSK scenario for $E_s = 7$dB and $\sigma_w^2 = 0$dB.

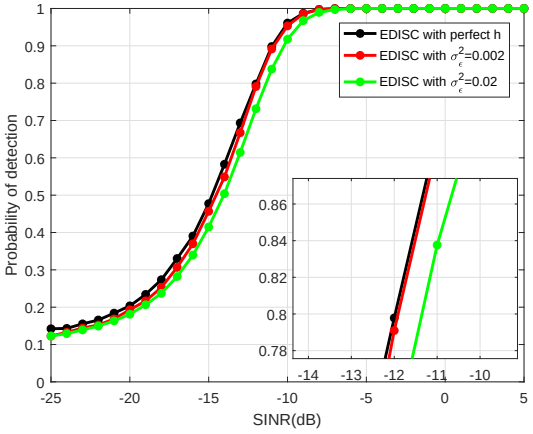

FIGURE 3.15: P_D versus the SINR of the PU, for the BPSK case considering channel uncertainty, for $N = 100$, $E_s = 10$ dB and $\sigma_w^2 = 2$ dB.

3.6 Summary

In this chapter, the idea of simultaneous spectrum sensing and data transmission considering imperfect signal cancellation in the data domain was investigated. We analyzed how the decoding errors affect the detection reliability of the system and derived the analytical expressions for the probability of false alarm assuming digitally modulated signals (i.e. BPSK, QPSK, M-QAM). Furthermore, a detailed analysis around the distribution of the sum of N truncated central or non-central chi-squared random variables was presented. Finally, the numerical results showed that the detection performance of our proposed scheme is considerably better than the conventional energy detector, verifying in this way the accuracy of the proposed study.

Chapter 4

Energy Detector with Imperfect Signal Cancellation for Interference Detection On-board the Satellite

This chapter discusses about the problem of interference on satellite communications and proposes two novel algorithms to overcome reliably this issue. Section 4.2 presents the system model and discusses about the conventional energy detector. Section 4.3 and Section 4.4 describe the algorithm of the energy detector with imperfect signal cancellation in the pilot and data domain, respectively, and derive analytical closed-form expressions for the probabilities of false alarm and detection. Numerical results are presented in Section 4.5. Finally, Section 4.6 summarizes the chapter.

4.1 Introduction

Interference has been identified as a major threat for satellite communication systems and services [21]. Interference has a financial impact on the satellite operators that can run into several million dollars [22]. The situation is likely to become worse over the next years as there are 1) a steady increase of satellites in orbit; 2) new deployment of terrestrial and space systems; and 3) a constant increase in two-way communications to support broadband/broadcast services. Therefore, interference management is a crucial issue for the commercial satellite industry.

As discussed with more details in Section 2.2, interference can be classified into two categories: intra-system interference and external interference [63], [68]. Some potential sources of intra-system interference in the satellite network are: co-channel interference, adjacent channel interference and cross-pol interference [63] - [70]. On the other hand, some examples of potential external interference sources are: adjacent system interference, in-line interference, terrestrial interference and intentional interference [63] - [72]. The satellite interference can be also classified in terms of the nature of the interference source into intentional interference and unintentional interference. Finally, the types of unintentional interference can be further classified according to the service that the interfering signals belong e.g., BSS, FSS, VSAT.

The proper handling of interference can be achieved through various steps: interference monitoring; interference detection and isolation; interference classification; interference localization; and interference mitigation [21]. This chapter focuses on the detection of interference, particularly on-board interference detection by introducing a dedicated spectrum monitoring unit within the satellite payload. The advantages of on-board interference detection with respect to ground-based solutions are summarized as follows: 1) simplification of the ground based stations in multi-beam satellites by avoiding equipment replication in multiple earth stations; 2) faster reaction time; and 3) avoidance of the additional downlink noise and possible distortions related to the satellite transponder. However, on-board implementation faces some technical challenges which have to be taken into account, with the most important being the minimization of the computational complexity and power consumption.

Almost all commercial communication satellites are transparent (bent pipe type) and made of a sequence of basic building blocks. The received signal by the satellite is amplified with a low noise amplifier (LNA), filtered to select the channel of interest, converted in frequency, high power amplified, and sent back to the ground after some clean-up filtering. Each building block is essentially a piece of expensive analog hardware, designed and manufactured with huge care and extensively tested to verify its specifications. However, there is an on-board revolution underway through the use of powerful digital signal processors (DSPs). The motivation for digitalization is first to improve payload's flexibility to an extent that is just unthinkable in analog hardware. To this end, for example, SES-12 and SES-14 satellites carry a DTP, which is the very first step in the direction of a more advanced vision that is likely to materialize in the coming years: the full payload digitalization [91]. In a fully digital payload, the promise is that most of the analog blocks will be removed and replaced by the equivalent functions implemented in a DSP. In this respect, as an example, SES-17 satellite refers to the next generation fully digital payloads, which will allow extraordinary efficiency and unrivalled

flexibility in bandwidth management capabilities. Various types of communication payloads exist (for relevant survey, see e.g., [92]), however, this chapter focuses on DTP [93], [94] and Hybrid DTP/Regenerative payload [63]. The payload of a regenerative satellite enables demodulation, decoding, encoding and modulation on-board. On the other hand, the DTP transponder is not regenerative but it is designed to allow digital signal processing such as the conversion of an analog-to-digital (A/D) signal and further processing on this digitized signal for flexible channelization and routing. Furthermore, the DTP requires much less processing capacity compared to the regenerative payloads. Finally, it is worth mentioning that generally the limitations of on-board processing is the on-board power consumed by the DSP rather than the hardware itself.

In this chapter, two advanced satellite interference monitoring modules for the communication payload based on the aforementioned two types of transponders are proposed. The interference detection module may be designed in terms of one of the common spectrum sensing techniques discussed in the literature [3], including matched filter detection [4], cyclostationary detection [9] and energy detection [5] -[8]. From these detectors, the ED is considered as our adopted detection technique of this chapter because it does not require information about the interfering signal, and its practical implementation is simple and cost effective. However, the main drawback of the ED for the detection of interference is its sensitivity to the noise variance and desired signal power uncertainties [25].

4.1.1 Chapter Contributions

To address this concern of the conventional energy detector, first, a new detection scheme based on the energy detector with signal cancellation exploiting the pilot symbols of the satellite communication standards is proposed. This proposed detector, first processes the total received signal in order to keep only the samples related to the position of the pilot symbols, subsequently removes the pilot symbols from this new received signal and then applies an energy detector on the remaining signal to decide on the presence or absence of interference. This detector does not require regenerative functionalities (i.e. demodulation, decoding, etc.) on-board the satellite and hence, the proposed interference detection unit could be part of the DSP of an on-board DTP technology, as shown in Figure 4.1.

As mentioned earlier, the proposed detector is applied only on the samples related to the position of the pilot symbols. However, the detection of weak interfering signal may require more samples than the number of pilots supported by the standards. Furthermore, if the interference is intermittent during the frame, the samples related to the position

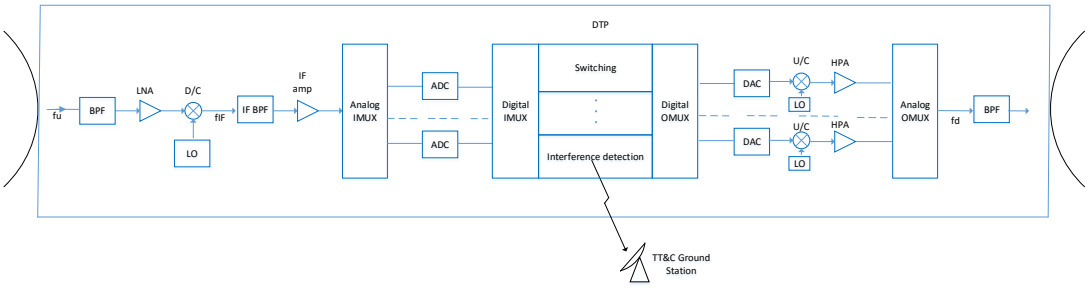

FIGURE 4.1: Digital Transparent Processor satellite payload including an interference detection module[1].

of the pilot symbols may not be affected, and thus the previous method will not provide a reliable detection of interference. To address this issue, a second more sophisticated detection scheme based on the idea of two-stage detectors [27] - [28] is also proposed. In the first stage, the energy detector with signal cancellation exploiting the pilot symbols is performed. In the second stage, the energy detector with signal cancellation is again used, where this time the processing is carried out on the data and not on the pilot symbols, decoding the data part, reconstructing it, removing it from the total received signal and applying again an ED on the remaining signal for interference detection. This proposed two-stage detector increases the computational complexity and requires a demodulation/modulation process on-board the satellite, however, it can detect very weak values of interference because it has the ability to process a large number of samples. This detector requires regenerative functionalities on-board the satellite, thus it fits well within a Hybrid DTP/Regenerative payload.

In this context, the contributions of the chapter are three-fold:

- The idea of detecting the uplink satellite interference by introducing a dedicated spectrum monitoring unit within the satellite payload is investigated. Two advanced payload architectures for this purpose are considered, based on the digital transparent processor (DTP) and Hybrid DTP/Regenerative payloads.

- Furthermore, two detectors for the detection of weak interfering signals are proposed. Both detectors are based on the energy detector and signal cancellation. The first detection scheme exploits the pilot symbols of the satellite standards, while the second detection scheme employs a two-stage detector. The first stage is again based on the pilot symbols, but the detector of the second stage processes

[1]where BPF: bandpass filter, LNA: low noise amplifier, D/C: down-conversion, LO: local oscillator, IF: intermediate frequency, ADC: analog-to digital-converter, IMUX: input multiplexer, OMUX: output multiplexer, DAC: digital-to-analog converter, U/C: up-conversion, and HPA: high power amplifier.

the received signal in the data domain. Numerical results show that both detectors provide better detection performance than the conventional energy detector, particularly for weak interfering signals and in the presence of the noise and signal power uncertainties.

- In addition, evaluation how the imperfect signal cancellation due to the channel estimation error affects the sensing performance is carried out. Analytical closed-form expressions for the probability of false alarm and probability of detection are derived and the decision threshold with the aim to maximize the probability of detection for a given false alarm rate is designed. It is worth mentioning that although this chapter focuses on the detection of interference in satellite communications, the developed techniques can be straightforwardly applied in any wireless communication system.

4.2 System Model

A common satellite interference scenario is considered, where the satellite, the desired terminal and the interferer are equipped with one antenna. Then, a binary hypothesis test can be used in order to represent the interference detection problem, as follows:

$$\mathcal{H}_0: \quad \mathbf{y}=h\mathbf{s}+\mathbf{w}, \tag{4.1}$$

$$\mathcal{H}_1: \quad \mathbf{y}=h\mathbf{s}+\mathbf{w}+\mathbf{i}, \tag{4.2}$$

where $\mathbf{y} = [y(1) \cdots y(N)]^T$, h, $\mathbf{s} = [s(1) \cdots s(N)]^T$, $\mathbf{w} = [w(1) \cdots w(N)]^T$ and $\mathbf{i} = [i(1) \cdots i(N)]^T$ denote the total received signal, the uplink channel, the transmitted signal by the desired terminal, the AWGN and the interfering signal, respectively. The desired transmitted signal $\mathbf{s}$ is a modulated signal consisted of an amount of N_p number of pilot symbols $\mathbf{s}_p$, interleaved with an N_d number of data streams $\mathbf{s}_d$. Therefore, $N = N_p + N_d$, with N denoting the total number of samples. Furthermore, it holds that, $\mathbf{w} \sim \mathcal{CN}\left(0, \sigma_w^2 \mathbf{I}_N\right)$ and $\mathbf{i} \sim \mathcal{CN}\left(0, \sigma_i^2 \mathbf{I}_N\right)$ with σ_w^2 and σ_i^2 denoting the variance of the AWGN and Gaussian interference (it can be the aggregated signal of several VSAT terminals), respectively. Similar signal models are frequently used in the literature [46], [88], [89] for cases without knowledge of the symbols of the signal as is the case for the interfering signal. It is worth mentioning that the most important factor in the design of a detection scheme is the proper selection of the decision threshold, which is derived in maximizing the P_D for a specific P_{FA} constraint.

4.2.1 Probabilities of false alarm and detection of the conventional energy detector

In this subsection, the CED is presented as a benchmark of the work. The CED computes the energy of the received baseband signal, compares it with a properly selected threshold and decides if the interference is present or not. Therefore, applying the energy detector in the hypothesis test of (4.1) and (4.2) as follows:

$$T(\mathbf{y}) = \|\mathbf{y}\|^2 = \sum_{n=1}^{N} |y(n)|^2 \begin{array}{l} < \gamma_{ced} \rightarrow \mathcal{H}_0 \\ > \gamma_{ced} \rightarrow \mathcal{H}_1 \end{array}, \tag{4.3}$$

where γ_{ced} is the decision threshold under the conventional energy detector, it is shown that the distribution of the test statistic $T(\mathbf{y})$ follows a non-central Gaussian distribution with $2N$ degrees of freedom for both hypotheses, $\mathcal{H}_0$ and $\mathcal{H}_1$, and the probability of false alarm and probability of detection, in this case $P_{FA_{ced}}$ and $P_{D_{ced}}$, can be expressed in closed form as:

$$P_{FA_{ced}} = Q_N\left(\sqrt{\rho_{\mathcal{H}_0}}, \sqrt{\frac{2\gamma_{ced}}{\sigma_w^2}}\right), \qquad P_{D_{ced}} = Q_N\left(\sqrt{\rho_{\mathcal{H}_1}}, \sqrt{\frac{2\gamma_{ced}}{\sigma_i^2+\sigma_w^2}}\right), \tag{4.4}$$

where the non-centrality parameter is given by $\rho_{\mathcal{H}_0} = \frac{2|h|^2 E_s}{\sigma_w^2}$ under the hypothesis $\mathcal{H}_0$ and $\rho_{\mathcal{H}_1} = \frac{2|h|^2 E_s}{\sigma_w^2+\sigma_i^2}$ for the hypothesis $\mathcal{H}_1$, respectively, and E_s denotes the energy of the desired transmitted signal.

The CED needs accurate information about the noise and signal power. However, accurate estimation of these parameters, in practice, is not possible. Therefore, the corresponding expressions for the case of noise variance and signal energy uncertainties are given as follows:

$$P_{FA_{u_{ced}}} = Q_N\left(\sqrt{\frac{2\eta_{E_s}|h|^2 E_s}{\eta_w \sigma_w^2}}, \sqrt{\frac{2\gamma_{u_{ced}}}{\eta_w \sigma_w^2}}\right), \qquad P_{D_{u_{ced}}} = Q_N\left(\sqrt{\rho_{\mathcal{H}_1}}, \sqrt{\frac{2\gamma_{u_{ced}}}{\sigma_i^2+\sigma_w^2}}\right), \tag{4.5}$$

where $\gamma_{u_{ced}}$ is the decision threshold under the uncertainty scenario of the conventional energy detector, while the uncertainty factor is defined as $B_w = 10\log_{10}\eta_w$ and $B_{E_s} = 10\log_{10}\eta_{E_s}$ for the noise variance and signal energy, respectively, with B_w and B_{E_s} to be expressed in dB.

It is noted that the proper decision threshold γ_{ced} is designed in order to maximize the probability of detection $P_{D_{ced}}$ for a given false alarm rate β. Then, the optimal value of

the $P_{D_{ced}}$ is obtained by $P_{FA_{ced}} = \beta$, because the $P_{D_{ced}}$ is an increasing function of the $P_{FA_{ced}}$. Similar methodology can be followed for the case with uncertainty ($\gamma_{u_{ced}}$).

Finally, it is mentioned that the conventional energy detector has low complexity and constitutes a reliable solution for the detection of strong interfering signals. However, as mentioned earlier, it faces difficulties in the detection of weak interferences.

4.3 Energy Detector with Imperfect Signal Cancellation in the Pilot Domain

In this section, an algorithm for the detection of weak interfering signals on-board the satellite exploiting the frame structure of the satellite standards is proposed. This detector is well suited to the DTP payloads. These payloads allow the use of digital signal processing techniques of the analog-to-digital converted signals, but the signals are still not demodulated or modulated on-board. Furthermore, analytical expressions for the probabilities of false alarm and detection of the developed technique are derived. Finally, the appropriate detection threshold is derived by maximizing the P_D for a specific constraint β on the P_{FA}. This shows that in this case, the detection threshold can be defined independently from the type of interference's distribution.

4.3.1 Proposed algorithm for DTP satellite payloads

The proposed payload and interference detection scheme are presented in Figure 4.1 and Figure 4.2, respectively, where after the use of analog input multiplexers each channel is digitized by a high-speed analog-to-digital converter. Then, the output of each processor is digitally filtered and subsequently, our proposed interference detection module processes the signal based on the following algorithm. Finally, the information on the presence or absence of interference is sent to the ground station through the Telemetry, Tracking and Control (TT&C) link for further actions.

Algorithm 1: Energy detector with imperfect signal cancellation exploiting the pilot symbols

1. After the initial stage of frame synchronization, the positions of the pilots in the total received signal are known. Hence, the samples related to the position of the pilot symbols can be extracted. Then, the binary hypothesis test of (4.1), (4.2) is

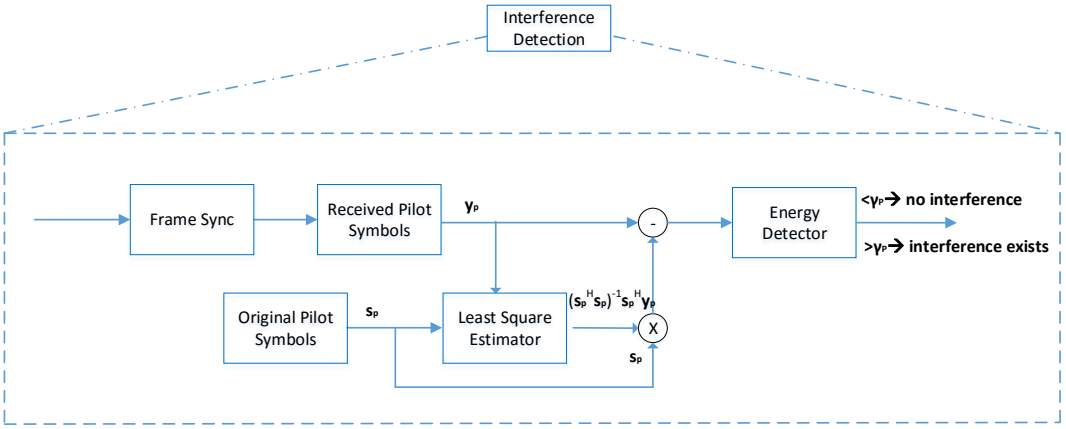

FIGURE 4.2: Interference detection module based on the first proposed algorithm.

reformulated as follows:

$$\mathcal{H}_{0_p}: \quad \mathbf{y}_p = h\mathbf{s}_p + \mathbf{w}_p, \tag{4.6}$$

$$\mathcal{H}_{1_p}: \quad \mathbf{y}_p = h\mathbf{s}_p + \mathbf{w}_p + \mathbf{i}_p, \tag{4.7}$$

where $\mathbf{y}_p = [y_p(1) \cdots y_p(N_p)]^T$, $\mathbf{s}_p = [s_p(1) \cdots s_p(N_p)]^T$, $\mathbf{w}_p = [w_p(1) \cdots w_p(N_p)]^T$ and $\mathbf{i}_p = [i_p(1) \cdots i_p(N_p)]^T$ denote the received signal related to pilots' position, the pilot symbols, the AWGN related to pilots' position and the interfering signal related to pilots' position, respectively. The pilots symbols have power P_p or energy E_p, while $\mathbf{w}_p \sim \mathcal{CN}\left(0, \sigma_{w_p}^2 \mathbf{I}_{N_p}\right)$ and $\mathbf{i}_p \sim \mathcal{CN}\left(0, \sigma_{i_p}^2 \mathbf{I}_{N_p}\right)$ with $\sigma_{w_p}^2 = \sigma_w^2$ and $\sigma_{i_p}^2 = \sigma_i^2$ denoting the variance of the $\mathbf{w}_p$ and $\mathbf{i}_p$, respectively.

2. Then, with the aid of the pilot symbols and the use of a least square estimator, the channel can be estimated. The estimated channel $\hat{h}$ ($\hat{h} = \left(\mathbf{s}_p^H \mathbf{s}_p\right)^{-1} \mathbf{s}_p^H \mathbf{y}_p$) can be modeled as:

$$\begin{aligned} \hat{h}_{\mathcal{H}_0} &= h + \varepsilon_{\mathcal{H}_0}, \\ \hat{h}_{\mathcal{H}_1} &= h + \varepsilon_{\mathcal{H}_1}, \end{aligned} \tag{4.8}$$

where $\varepsilon_{\mathcal{H}_0}$ and $\varepsilon_{\mathcal{H}_1}$ denote the channel estimation error under the hypothesis $\mathcal{H}_0$ and $\mathcal{H}_1$, respectively. They are considered to follow a Gaussian distribution, as it is shown in Appendix E, with zero mean and variance $\sigma_{\varepsilon_{\mathcal{H}_0}}^2 = \frac{\sigma_{w_p}^2}{E_p}$ and $\sigma_{\varepsilon_{\mathcal{H}_1}}^2 = \frac{\sigma_{w_p}^2 + \sigma_{i_p}^2}{E_p}$, respectively.

3. Furthermore, the original pilot symbols $\mathbf{s}_p$ are removed from the received signal of (4.6), (4.7) $(\mathbf{y}_p - \hat{h}\mathbf{s}_p)$ and the new hypothesis test can be written as:

$$\mathcal{H}'_{0_p}: \quad \mathbf{y}'_p = \mathbf{w}_p \text{-} \varepsilon_{\mathcal{H}_0} \mathbf{s}_p, \tag{4.9}$$

$$\mathcal{H}'_{1_p}: \quad \mathbf{y}'_p = \mathbf{i}_p + \mathbf{w}_p \text{-} \varepsilon_{\mathcal{H}_1} \mathbf{s}_p. \tag{4.10}$$

with covariance matrix $R_{\mathcal{H}'_{0_p}} = \sigma^2_{w_p} \mathbf{I}_{N_p} - \frac{\sigma^2_{w_p}}{E_p} \mathbf{s}_p \mathbf{s}_p^H$ and $R_{\mathcal{H}'_{1_p}} = \left(\sigma^2_{w_p} + \sigma^2_{i_p}\right) \mathbf{I}_{N_p} - \frac{\sigma^2_{w_p} + \sigma^2_{i_p}}{E_p} \mathbf{s}_p \mathbf{s}_p^H$, respectively. The proof related to the covariance matrices is presented in Appendix F. Here, it should be noted that the remaining signal $\mathbf{y}'_p$ consists of correlated Gaussian variables, because as it can be seen, the covariance matrix is not diagonal under both hypotheses.

4. Finally, an ED is applied in the remaining signal in order to detect the presence or absence of the interference, as follows:

$$T\left(\mathbf{y}'_p\right) = \left\|\mathbf{y}'_p\right\|^2 = \sum_{n=1}^{N_p} \left|y'_p\left(n\right)\right|^2 \begin{array}{l} < \gamma_p \rightarrow \mathcal{H}'_{0_p} \\ > \gamma_p \rightarrow \mathcal{H}'_{1_p} \end{array}, \tag{4.11}$$

where γ_p denotes a properly defined threshold, responsible for the detection of interference.

■

In the next two subsections, the probabilities of false alarm and detection are derived, and the detection threshold is determined.

4.3.2 Probability of false alarm of the developed detector based on the pilots symbols

As mentioned earlier, the proper selection of the detection threshold constitutes the most important parameter for the design of any detection scheme. The determination of this threshold is based on maximizing the probability of detection for a specific constraint on the probability of false alarm. Therefore, the derivation of the theoretical expressions for the probability of false alarm of the energy detector with signal cancellation exploiting the pilot symbols, in this case P_{FA_p}, which is defined as $P_{FA_p} = Pr\left(\mathbf{y}'_p > \gamma_p | \mathcal{H}'_{0_p}\right)$ [49], is provided in this subsection.

Theorem 4.1: Consider a telecommunication system (satellite, mobile phone, etc.) with one receive antenna, which collects a number of samples N. The channel is assumed quasi-static. The receiver, first extracts the received samples related to the position of

the pilot symbols, then estimates the channel, subsequently removes the pilot symbols from the new extracted received signal and finally applies an energy detector in the remaining signal. Then, the P_{FA_p} is derived as follows:

$$P_{FA_p} = \frac{\Gamma\left(N_p - 1, \frac{\gamma_p}{\sigma^2_{w_p}}\right)}{\Gamma\left(N_p - 1\right)}. \tag{4.12}$$

Proof: The computation of the P_{FA_p} is based on the knowledge of the test statistic's distribution under the hypothesis $\mathcal{H}'_{0_p}$. Therefore, the distribution of the sum of N_p correlated chi-squared variables should be derived, because as mentioned earlier, the remaining signal $\mathbf{y}'_p$ consists of correlated Gaussian variables.

The distribution of the sum of N_p chi-squared variables can be approximated by a weighted chi-squared distribution with f degrees of freedom [95]. Therefore, the distribution of the test statistic $T\left(\mathbf{y}'_p|\mathcal{H}'_{0_p}\right)$ can be modeled as:

$$T(\mathbf{y}'_p|\mathcal{H}'_{0_p}) \sim c_{\mathcal{H}_{0'_p}} \chi^2_{f_{\mathcal{H}_{0'_p}}}, \tag{4.13}$$

where

$$c_{\mathcal{H}'_{0_p}} = \frac{\mathbb{V}\{T(\mathbf{y}'_p|\mathcal{H}'_{0_p})\}}{2\mathbb{E}\{T(\mathbf{y}'_p|\mathcal{H}'_{0_p})\}} \quad \text{and} \quad f_{\mathcal{H}'_{0_p}} = \frac{2\mathbb{E}\{T(\mathbf{y}_p|\mathcal{H}'_{0_p})\}^2}{\mathbb{V}\{T(\mathbf{y}'_p|\mathcal{H}'_{0_p})\}}. \tag{4.14}$$

It is shown that the computation of the mean $\mathbb{E}\{T(\mathbf{y}'_p|\mathcal{H}'_{0_p})\}$ and variance $\mathbb{V}\{T(\mathbf{y}'_p|\mathcal{H}'_{0_p})\}$ of the test statistic $T\left(\mathbf{y}'_p|\mathcal{H}'_{0_p}\right)$ is required. This derivation can be obtained by using the MGF of a set of N_p correlated chi-squared variables [96]. In this case, the MGF of the test statistic $T\left(\mathbf{y}'_p|\mathcal{H}_0\right)$ is given by

$$M_{T(\mathbf{y}'_p|\mathcal{H}'_{0_p})}(s) = \prod_{n=1}^{N_p} \left(1 - s\left(\sigma^2_{w_p} - \frac{\sigma^2_{w_p}}{E_p}\lambda_n\right)\right)^{-1}, \tag{4.15}$$

where s in (4.15) referred to the Laplace transform and λ_n is the n-th eigenvalue of the matrix $\mathbf{s}_p\mathbf{s}_p^H$ of the covariance matrix $R_{\mathcal{H}'_{0_p}}$. Then, the mean and variance of the sum of N_p correlated chi-squared variables can be expressed as follows:

$$\mathbb{E}\{T(\mathbf{y}'_p|\mathcal{H}'_{0_p})\} = M'_{T(\mathbf{y}'_p|\mathcal{H}'_{0_p})}(s)|_{s=0} = \sum_{n=1}^{N_p}\left(\sigma^2_{w_p} - \frac{\sigma^2_{w_p}}{E_p}\lambda_n\right) \tag{4.16}$$

and

$$\mathbb{V}\{T(\mathbf{y}'_p|\mathcal{H}'_{0_p})\} = M''_{T(\mathbf{y}'_p|\mathcal{H}_0)}(s)|_{s=0} - \left(M'_{T(\mathbf{y}'_p|\mathcal{H}'_{0_p})}(s)|_{s=0}\right)^2 = \sum_{n=1}^{N_p}\left(\sigma^2_{w_p} - \frac{\sigma^2_{w_p}}{E_p}\lambda_n\right)^2, \tag{4.17}$$

where $M'_{T(\mathbf{y}'_p|\mathcal{H}'_{0_p})}(s)|_{s=0}$ and $M''_{T(\mathbf{y}'_p|\mathcal{H}'_{0_p})}(s)|_{s=0}$ denote the first and second derivative of (4.15) with respect to s, respectively.

The derivation of $c_{\mathcal{H}'_{0_p}}$ and $f_{\mathcal{H}'_{0_p}}$ is completed by substituting (4.16) and (4.17) to (4.14) as follows:

$$c_{\mathcal{H}'_{0_p}} = \frac{\sum_{n=1}^{N_p}\left(\sigma^2_{w_p} - \frac{\sigma^2_{w_p}}{E_p}\lambda_n\right)^2}{2\sum_{n=1}^{N_p}\left(\sigma^2_{w_p} - \frac{\sigma^2_{w_p}}{E_p}\lambda_n\right)} \quad \text{and} \quad f_{\mathcal{H}'_{0_p}} = \frac{\left(\sum_{n=1}^{N_p}\left(\sigma^2_{w_p} - \frac{\sigma^2_{w_p}}{E_p}\lambda_n\right)\right)^2}{2\sum_{n=1}^{N_p}\left(\sigma^2_{w_p} - \frac{\sigma^2_{w_p}}{E_p}\lambda_n\right)^2}. \tag{4.18}$$

Therefore, all the parameters of (4.13) have been derived. Finally, because the P_{FA_p} is defined as $P_{FA_p} = Pr\left(\mathbf{y}'_p > \gamma|\mathcal{H}'_{0_p}\right)$, we can use (4.13) in order to obtain the CDF, which is then employed to derive the closed form expression of the P_{FA_p} as follows:

$$P_{FA_p} = \frac{\Gamma\left(\frac{f_{\mathcal{H}'_{0_p}}}{2}, \frac{\gamma_p \sum_{n=1}^{N_p}\left(\sigma^2_{w_p} - \frac{\sigma^2_{w_p}}{E_p}\lambda_n\right)}{\sum_{n=1}^{N_p}\left(\sigma^2_{w_p} - \frac{\sigma^2_{w_p}}{E_s}\lambda_n\right)^2}\right)}{\Gamma\left(\frac{f_{\mathcal{H}'_{0_p}}}{2}\right)}, \tag{4.19}$$

where $\Gamma(\cdot)$ is the gamma function, while $\Gamma(\cdot,\cdot)$ is the incomplete gamma function. However, the pilot symbols $\mathbf{s}_p$ constitute a fixed known sequence, which implies a rank 1 signal and hence, the largest eigenvalue is $\lambda_1 = \mathbf{s}_p^H\mathbf{s}_p = E_p$, while the rest are $\lambda_2 = \lambda_3 = ... = \lambda_{N_p} = 0$. Thus, (4.19) can be simplified into the expression given by (4.12). ■

It can be noticed from (4.12) that the P_{FA_p} depends on the noise variance related to the pilots $\sigma^2_{w_p}$. However, in practice, the noise variance is often unknown and it should be estimated. For this reason, the probability of false alarm taking into account the noise uncertainty, in this case $P_{FA_{u_p}}$, is expressed as follows:

$$P_{FA_{u_p}} = \frac{\Gamma\left(N_p - 1, \frac{\gamma_{u_p}}{\eta_{w_p}\sigma^2_{w_p}}\right)}{\Gamma(N_p - 1)}, \tag{4.20}$$

where γ_{u_p} denotes the decision threshold for the scenario of noise uncertainty, while the uncertainty factor is defined as $B_p = 10\log_{10}\eta_{w_p}$, with B_p to be expressed in dB.

4.3.3 Probability of detection of the developed detector based on the pilots symbols

Here, the analytical expressions for the probability of detection of the energy detector with signal cancellation exploiting the pilot symbols are provided. Therefore, following the same approach as for P_{FA_p} and taking into account that P_{D_p} is defined as $P_{D_p} = Pr\left(\mathbf{y}'_p > \gamma_p | \mathcal{H}'_{1_p}\right)$, the P_{D_p} can be derived by substituting $\sigma^2_{w_p}$ with $\sigma^2_{w_p} + \sigma^2_{i_p}$ in the related parts of (4.12) as follows:

$$P_{D_p} = \frac{\Gamma\left(N_p - 1, \frac{\gamma_p}{\sigma^2_{w_p}+\sigma^2_{i_p}}\right)}{\Gamma\left(N_p - 1\right)}. \tag{4.21}$$

The corresponding expression for the case of noise uncertainty, in this case $P_{D_{u_p}}$, is given by

$$P_{D_{u_p}} = \frac{\Gamma\left(N_p - 1, \frac{\gamma_{u_p}}{\sigma^2_{w_p}+\sigma^2_{i_p}}\right)}{\Gamma\left(N_p - 1\right)}. \tag{4.22}$$

It is noted that the proper decision threshold γ_p is designed in order to maximize the probability of detection P_{D_p} for a given false alarm constraint β. Therefore, this problem can be formulated as follows:

$$\begin{aligned} \max_{(\gamma_p)} \quad & P_{D_p}\left(\gamma_p\right) \\ \text{s.t} \quad & P_{FA_p} \leq \beta. \end{aligned} \tag{4.23}$$

Considering the fact that P_{D_p} is an increasing function P_{FA_p}, the optimal value of the probability of detection in (4.23) is obtained by $P_{FA_p} = \beta$. Therefore, in this case where the P_{FA_p} is a function of the threshold γ_p, $P_{FA_p} = f(\gamma_p) = \frac{\Gamma\left(N_p-1, \frac{\gamma_p}{\sigma^2_{w_p}}\right)}{\Gamma(N_p-1)}$, this threshold can be easily derived as follows:

$$\gamma_p = f^{-1}(\beta). \tag{4.24}$$

Here, it is shown that the derivation of the decision threshold γ_p is independent of the interference's distribution. Similar methodology can be followed to determine the threshold γ_{u_p} for the case of noise variance uncertainty.

4.4 Two-Stage Energy Detector Including Imperfect Signal Cancellation in the Data Domain

In this section, a second algorithm for the detection of weak interfering signals on-board the satellite based on the idea of two-stage detectors is proposed. Furthermore, analytical

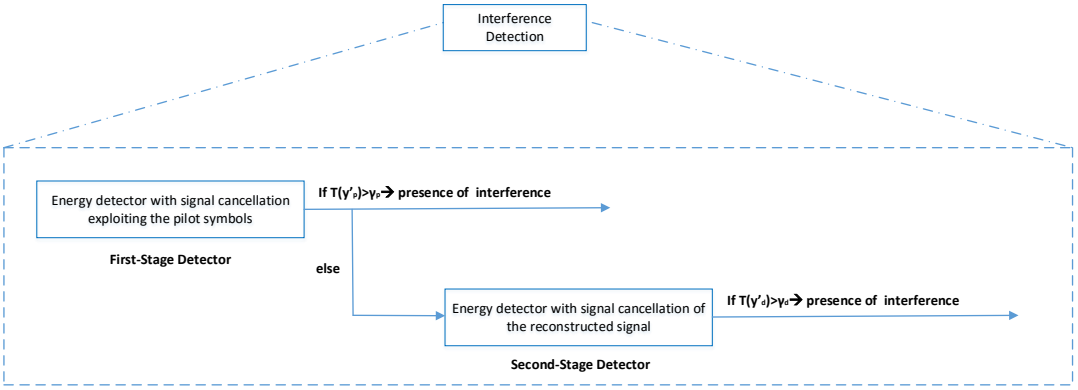

FIGURE 4.3: Two-stage interference detection scheme.

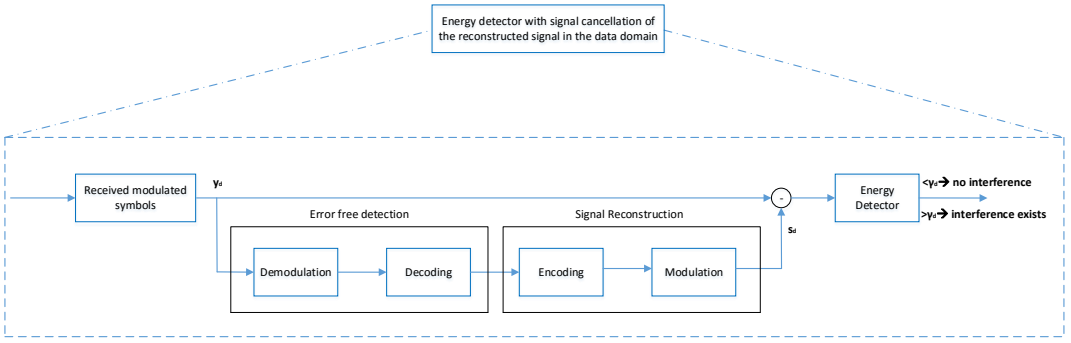

FIGURE 4.4: Energy detector with signal cancellation of the reconstructed signal in the data domain.

closed-form expressions for the probability of false alarm of this developed technique are derived. Finally, we derive closed-form expressions for the probability of detection and discuss the underlying mechanism to determine the detection threshold of each stage.

4.4.1 Proposed algorithm for Hybrid DTP/Regenerative satellite payloads

The previous developed detector is performed only on the samples related to the position of the pilot symbols. However, the detection of weak interfering signals may require more samples than the number of pilots supported by the standards. This is particularly valid for the return link, where the number of pilots are much more limited than the forward link. Furthermore, as mentioned earlier, if the interference is intermittent during the frame, the samples related to the position of the pilot symbols may not be affected, and then, an alternative algorithm is required.

To address this concern, in this subsection, a more sophisticated interference detection scheme based on the idea of two-stage detectors is proposed. As it is shown in Figure 4.3, in the first stage, energy detection with signal cancellation exploiting the pilot symbols, same as before, is performed. If the energy is above a certain threshold γ_p, the interference is declared to be present. Otherwise, an energy detector with cancellation of the reconstructed signal in the data domain is performed in the second stage. This second detector is presented in Figure 4.4. If the decision metric in this stage exceeds a certain threshold γ_d, the interference is declared to be present. Else, it is declared to be absent. This second detector uses the increased number of samples in the data domain to obtain a more accurate detection result.

Here, it is noted that the second-stage detector is used for detection of very low values of interference and it may be applied only in the channels which the satellite operators have characterized more suspicious for the appearance of interference or a higher level of protection is necessary. Therefore, this detector is well suited to Hybrid DTP/regenerative payloads, where part of the signal in time or frequency is demodulated, decoded, encoded and modulated on-board the satellite. Ultimately, digitalization also opens the perspective of regenerative payloads, demodulating the signal on-board to improve the link performances, and paves the way to higher layer on-board functionalities. In the following, the two stages of energy detection with imperfect signal cancellation shall be discussed.

Algorithm 2: Two-stage energy detector with imperfect signal cancellation.

1. In the first stage, we try to detect the presence or absence of the interference using the energy detector with imperfect signal cancellation exploiting the pilot symbols as described earlier in Section 4.3.

2. If the detector of the first stage does not sense the interference, we continue and a final decision is taken after the second stage. In this second stage, we use the estimated channel from the first stage, and we also process the received signal in the data domain. Then, the binary hypothesis test of (4.1), (4.2) is reformulated as follows:

$$\mathcal{H}_{0_d}: \quad \mathbf{y}_d = h\mathbf{s}_d + \mathbf{w}_d, \tag{4.25}$$

$$\mathcal{H}_{1_d}: \quad \mathbf{y}_d = h\mathbf{s}_d + \mathbf{w}_d + \mathbf{i}_d, \tag{4.26}$$

with $\mathbf{y}_d = [y_d(1) \cdots y_d(N_d)]^T$, $\mathbf{s}_d = [s_d(1) \cdots s_d(N_d)]^T$, $\mathbf{w}_d = [w_d(1) \cdots w_d(N_d)]^T$ and $\mathbf{i}_d = [i_d(1) \cdots i_d(N_d)]^T$ denote the received signal related to the modulated symbols, the transmitted data signal by the desired terminal, the AWGN related to the data symbols and the interfering signal related to data symbols,

respectively. The transmitted data signal has power P_d or energy E_d, while $\mathbf{w}_d \sim \mathcal{CN}\left(0, \sigma_{w_d}^2 \mathbf{I}_{N_d}\right)$ and $\mathbf{i}_d \sim \mathcal{CN}\left(0, \sigma_{i_d}^2 \mathbf{I}_{N_d}\right)$ with $\sigma_{w_d}^2 = \sigma_w^2$ and $\sigma_{i_d}^2 = \sigma_i^2$ denoting the variance of the $\mathbf{w}_d$ and $\mathbf{i}_d$, respectively.

3. Then, the received data signal is demodulated and decoded. Satellite standards, like DVB-S2X, support Adaptive Coding and Modulation (ACM) technology [97] which enables dynamic changes in the modulation and coding to ensure reliable link availability, which further implies very small probability of bit error. Therefore, assuming that the transmitted data streams are almost perfectly correctly decoded, we can use them again in order to reconstruct the transmitted signal. Subsequently, the reconstructed signal is removed from the received signal of (4.25), (4.26) and the new hypothesis test can be written as:

$$\mathcal{H}'_{0_d}: \quad \mathbf{y}'_d = \mathbf{w}_d \text{-} \varepsilon_{\mathcal{H}_0} \mathbf{s}_d, \tag{4.27}$$

$$\mathcal{H}'_{1_d}: \quad \mathbf{y}'_d = \mathbf{i}_d + \mathbf{w}_d \text{-} \varepsilon_{\mathcal{H}_1} \mathbf{s}_d. \tag{4.28}$$

4. Finally, an ED is applied in the remaining signal in order to detect the presence or absence of the interference, as follows:

$$T\left(\mathbf{y}'_d\right) = \left\|\mathbf{y}'_d\right\|^2 = \sum_{n=1}^{N_d} \left|y'_d\left(n\right)\right|^2 \begin{array}{l} < \gamma_d \rightarrow \mathcal{H}'_{0_d} \\ > \gamma_d \rightarrow \mathcal{H}'_{1_d} \end{array}, \tag{4.29}$$

where γ_d denotes a properly defined threshold, responsible for the detection of interference.

■

It should be noted that for the practical implementation of both methods, a successful frame synchronization and noise variance estimation is required. In the next two subsections, the probabilities of false alarm and detection are derived, and the detection threshold is determined.

4.4.2 Probability of false alarm of the developed two-stage detector

In the first stage, the energy detector with signal cancellation exploiting the pilot symbols is used, whose probability of false alarm is given by (4.12). However, in the second stage, an energy detector with cancellation of the reconstructed transmitted signal is employed. The average probability of false alarm of the second detector, in this case $\overline{P_{FA_d}}$, which is defined as $\overline{P_{FA_d}} = Pr\left(\mathbf{y}'_d > \gamma_d | \mathcal{H}'_{0_d}\right)$, can be expressed by the following theorem.

Theorem 4.2: Consider a a telecommunication system (satellite, mobile phone, etc.) with one receive antenna, which collects a number of samples N. The channel is assumed quasi-static. The receiver, first estimates the channel with the aid of the received samples related to the position of the pilot symbols, then demodulates and decodes the received samples related to the data symbols, subsequently reconstructs the original data transmitted signal using the decoded signal and finally applies an energy detector in the remaining signal. Then, the $\overline{P_{FA_d}}$ is derived as follows:

$$\begin{aligned}\overline{P_{FA_d}} = \frac{\Gamma(k)}{p^k} - \frac{\Gamma(k)2^k e^{\frac{-b^2}{2}} \Phi_2\left(1, k, 1; \frac{b^2}{2}, \frac{a^2b^2}{2a^2+4p}\right)}{(a^2+2p)^k} \\ + \frac{\Gamma(k)2^k e^{\frac{-b^2}{2}}}{(a^2+2p)^k} \sum_{n=0}^{m-1} \frac{b^{2n}}{n!2^n} {}_1F_1\left(k; n+1; \frac{a^2b^2}{2a^2+4p}\right),\end{aligned} \tag{4.30}$$

where $a = \sqrt{\frac{E_d}{\sigma^2_{w_d}}}$, $b = \sqrt{\frac{\gamma_d}{\sigma^2_{w_d}}}$, $p = \frac{1}{2}$, $k = \frac{1}{2}$, Φ_2 is the Humbert function [98] of the second kind and ${}_1F_1$ denote the Kummer hypergeometric function [99].

Proof: In the case of energy detector with signal cancellation of the reconstructed transmitted data signal, the test statistic under the hypothesis $\mathcal{H}'_{0_d}$ can be written as in (4.29) or more analytically by

$$T\left(\mathbf{y}'_d|\mathcal{H}'_{0_d}\right) = \left\|\mathbf{y}'_d\right\|^2 = \sum_{n=1}^{N_d} \left|w_d(n) - \varepsilon_{\mathcal{H}_0} s_d(n)\right|^2, \tag{4.31}$$

where this can be viewed as the summation of non-central squared Gaussian random variables. Therefore, the test statistic $T\left(\mathbf{y}'_d|\mathcal{H}'_{0_d}\right)$ follows a non-central chi-squared distribution with N_d degrees of freedom and non-centrality parameter $\lambda = {\varepsilon_{\mathcal{H}_0}}^2 E_d$ or

$$T\left(\mathbf{y}'_d|\mathcal{H}'_{0_d}\right) \sim \chi^2_{N_d}(\lambda). \tag{4.32}$$

Then, the probability of false alarm, in this case P_{FA_d} can be be derived as follows:

$$P_{FA_d} = Q_{N_d/2}\left(\sqrt{\frac{\varepsilon^2_{\mathcal{H}_0} E_d}{\sigma^2_{w_d}}}, \sqrt{\frac{\gamma_d}{\sigma^2_{w_d}}}\right), \tag{4.33}$$

where $Q_u(a, b)$ denotes the generalized Marcum Q-function.

However, it can be seen that P_{FA_d} depends on the squared value of the channel estimation error, which is a random variable. Therefore, the average probability of false alarm over the channel estimation error should be derived.

As showed earlier, the channel estimation error $\varepsilon_{\mathcal{H}_0}$ follows a normal distribution with zero mean and variance $\sigma^2_{\varepsilon_{\mathcal{H}_0}}$, hence, the squared channel estimation error $\varepsilon^2_{\mathcal{H}_0}$ is central

chi-squared distributed with one degree of freedom and the following PDF:

$$f\left(\varepsilon^2_{\mathcal{H}_0}\right) = \int_0^\infty \frac{1}{2^{1/2}\Gamma\left(1/2\right)} \left(\varepsilon^2_{\mathcal{H}_0}\right)^{-1/2} e^{\frac{-\varepsilon^2_{\mathcal{H}_0}}{2}} \qquad \varepsilon^2_{\mathcal{H}_0} \geq 0. \tag{4.34}$$

Thus, the average P_{FA_d} can be obtained by averaging (4.33) over (4.34) as follows:

$$\overline{P_{FA_d}} = \int_0^\infty \frac{1}{2^{1/2}\Gamma\left(1/2\right)} \left(\varepsilon^2_{\mathcal{H}_0}\right)^{-1/2} Q_{N_d/2}\left(\sqrt{\frac{\varepsilon^2_{\mathcal{H}_0} E_d}{\sigma^2_{w_d}}}, \sqrt{\frac{\gamma_d}{\sigma^2_{w_d}}}\right) d\varepsilon^2_{\mathcal{H}_0}. \tag{4.35}$$

Then, after some manipulations of the integral in (4.34) and the aid of [100] as we show in Appendix G, the final form of $\overline{P_{FA_d}}$ can be written as in (4.30). ■

The analytical expressions of the probabilities of false alarms of each stage have been computed based on Theorems 4.1 and 4.2. In the two-stage detection scheme, a false alarm occurs if, under $\mathcal{H}_0$, (i) $T\left(\mathbf{y'}_p\right) > \gamma_p$, or (ii) $T\left(\mathbf{y'}_d\right) > \gamma_d$ given that $T\left(\mathbf{y'}_p\right) \leq \gamma_p$. Therefore, the overall probability of false alarm of the two-stage detector is given by

$$\begin{aligned} P_{FA} &= Pr\left(\mathbf{y}'_p > \gamma_p | \mathcal{H}'_{0_p}\right) + \left(1 - Pr\left(\mathbf{y}'_p > \gamma_p | \mathcal{H}'_{0_p}\right)\right) Pr\left(\mathbf{y}'_d > \gamma_d | \mathcal{H}'_{0_d}\right) \\ &= P_{FA_p} + (1 - P_{FA_p})\overline{P_{FA_d}}. \end{aligned} \tag{4.36}$$

It can be noticed from (4.30) that the $\overline{P_{FA_d}}$ depends on the noise variance $\sigma^2_{w_d}$ and the energy of the transmitted modulated signal E_d. Therefore, for the more realistic scenario of noise variance and signal energy uncertainties, the average probability of false alarm, in this case $\overline{P_{FA_{u_d}}}$, is given as follows:

$$\begin{aligned} \overline{P_{FA_{u_d}}} = \frac{\Gamma(k)}{p^k} &- \frac{\Gamma(k) 2^k e^{\frac{-b_u^2}{2}} \Phi_2\left(1, k, 1; \frac{b_u^2}{2}, \frac{a_u^2 b_u^2}{2a_u^2 + 4p}\right)}{\left(a_u^2 + 2p\right)^k} \\ &+ \frac{\Gamma(k) 2^k e^{\frac{-b_u^2}{2}}}{\left(a_u^2 + 2p\right)^k} \sum_{n=0}^{m-1} \frac{b_u^{2n}}{n! 2^n} {}_1F_1\left(k; n+1; \frac{a_u^2 b_u^2}{2a_u^2 + 4p}\right), \end{aligned} \tag{4.37}$$

where $a_u = \sqrt{\frac{\eta_{E_d} E_d}{\eta_{w_d} \sigma^2_{w_d}}}$, $b_u = \sqrt{\frac{\gamma_{u_d}}{\sigma^2_{w_d}}}$ and γ_{u_d} denotes the decision threshold for the scenario of uncertainty, while the uncertainty factor is defined as $B_{w_d} = 10 \log_{10} \eta_{w_d}$ and $B_{E_d} = 10 \log_{10} \eta_{E_d}$ for the the noise variance and signal energy, respectively, with B_{w_d} and B_{E_d} to be expressed in dB.

Finally, the overall probability of false alarm of the two-stage detector for the case of variance and/or energy uncertainty is given by

$$\begin{aligned} P_{FA_u} &= Pr\left(\mathbf{y}'_p > \gamma_{u_p} | \mathcal{H}'_{0_p}\right) + \left(1 - Pr\left(\mathbf{y}'_p > \gamma_{u_p} | \mathcal{H}'_{0_p}\right)\right) Pr\left(\mathbf{y}'_d > \gamma_{u_d} | \mathcal{H}'_{0_d}\right) \\ &= P_{FA_{u_p}} + (1 - P_{FA_{u_p}})\overline{P_{FA_{u_d}}}. \end{aligned} \tag{4.38}$$

4.4.3 Probability of detection of the developed two-stage detector

Here, the analytical expressions for the P_D of the two-stage detector are provided. A correct detection occurs if, under $\mathcal{H}_1$, 1) $T\left(\mathbf{y}'_p\right) > \gamma_p$; or 2) $T\left(\mathbf{y}'_d\right) > \gamma_d$ given that $T\left(\mathbf{y}'_p\right) \leq \gamma_p$. Hence, the overall probability of detection is given by

$$\begin{aligned} P_D &= Pr\left(\mathbf{y}'_p > \gamma_p | \mathcal{H}'_{1_p}\right) + \left(1 - Pr\left(\mathbf{y}'_p > \gamma_p | \mathcal{H}'_{1_p}\right)\right) Pr\left(\mathbf{y}'_d > \gamma_d | \mathcal{H}'_{1_d}\right) \\ &= P_{D_p} + (1 - P_{D_p})\overline{P_{D_d}}, \end{aligned} \tag{4.39}$$

where under the assumption that the interfering signal follows a Gaussian distribution with zero mean and variance $\sigma^2_{i_p}$, the P_{D_p} is expressed by (4.21), while the $\overline{P_{D_d}}$ is derived by following similar methodology as for the case of P_{FA_d} and substituting $\sigma^2_{w_d}$ with $\sigma^2_{w_d} + \sigma^2_{i_d}$ in the related parts of (4.30).

The corresponding expression for the case of noise variance and signal energy uncertainty, in this case P_{D_u}, is given by

$$\begin{aligned} P_{D_u} &= Pr\left(\mathbf{y}'_p > \gamma_{u_p} | \mathcal{H}'_{1_p}\right) + \left(1 - Pr\left(\mathbf{y}'_p > \gamma_{u_p} | \mathcal{H}'_{1_p}\right)\right) Pr\left(\mathbf{y}'_d > \gamma_{u_d} | \mathcal{H}'_{1_d}\right) \\ &= P_{D_{u_p}} + (1 - P_{D_{u_p}})\overline{P_{D_{u_d}}}, \end{aligned} \tag{4.40}$$

where $P_{D_{u_p}}$ is defined by (4.22) while $P_{D_{u_d}}$ is computed similarly as in (4.37).

Now, the goal is to determine the proper decision thresholds γ_p and γ_d in order to maximize the probability of detection P_D for a given false alarm rate constraint β. It can be noticed from (4.38) that if $P_{FA} \leq \beta$ then

$$0 \leq P_{FA_p} \leq \beta \quad \text{and} \quad 0 \leq P_{FA_d} \leq \beta. \tag{4.41}$$

Therefore, this problem can be formulated as follows:

$$\begin{aligned} \max_{(\gamma_p,\gamma_d)} \quad & P_d\left(\gamma_p,\gamma_d\right) \\ \text{s.t} \quad & P_{FA}(\gamma_p,\gamma_d)=\beta, \\ & 0 \le P_{FA_p}(\gamma_p) \le \beta \\ & 0 \le P_{FA_d}(\gamma_d) \le \beta. \end{aligned} \tag{4.42}$$

It can be seen from (4.42) that when $P_{FA_d}=0$ the two-stage detector scheme is simplified to that of the first detector, namely the energy detector with signal cancellation exploiting the pilot symbols. Furthermore, when $P_{FA_p}=0$ only the second detector is used, namely the energy detector with signal cancellation of the reconstructed signal. However, for the general case that both detectors are used, the closed-form expression of this optimization problem is not mathematically tractable due to the non-convexity of the problem. Then, the selection of the proper pair of P_{FA_p} and P_{FA_d} for the determination of γ_p and γ_d, respectively, can be obtained by two-dimensions line search for each solution. Nevertheless, taking into account that the constraint $P_{FA}(\gamma_p,\gamma_d)=\beta$ can be written as

$$\begin{aligned} P_{FA}(\gamma_p,\gamma_d)=P_{FA_p}(\gamma_p)+\left(1-P_{FA_p}(\gamma_p)\right)P_{FA_d}(\gamma_d)=\beta \Rightarrow \\ P_{FA_p}(\gamma_p)=\frac{\beta-P_{FA_d}(\gamma_d)}{1-P_{FA_d}(\gamma_d)}, \end{aligned} \tag{4.43}$$

the threshold γ_p with the help of (4.24) can be derived by $\gamma_p = f^{-1}\left(\frac{\beta-P_{FA_d}(\gamma_d)}{1-P_{FA_d}(\gamma_d)}\right)$. Then, the above optimization problem can be simplified in the following one:

$$\begin{aligned} \max_{(\gamma_p,\gamma_d)} \quad & P_d\left(\gamma_p,\gamma_d\right) \\ \text{s.t} \quad & 0 \le P_{FA_d}(\gamma_d) \le \beta, \\ & \gamma_p = f^{-1}\left(\frac{\beta-P_{FA_d}(\gamma_d)}{1-P_{FA_d}(\gamma_d)}\right), \end{aligned} \tag{4.44}$$

where the problem can be solved by one dimension line search which is much faster than the two-dimensions search. Similar approach can be also followed for the case of uncertainty.

4.5 Numerical Results

In this part, several numerical results are presented in order to 1) verify that the channel estimation error can be modeled as Gaussian distributed; 2) verify the derived expressions of (4.12) and (4.33) for the probability of false alarm; and 3) assess the different

Parameter	Value
Orbit	GEO circular
Satellite height	35786 km
Satellite carrier frequency	14.25 GHz
VSAT EIRP	39.3 dBW
Uplink free space loss	206.59 dB
Total atmospheric attenuation (clear sky)	0.8 dB
Symbol rate	1 Msps

TABLE 4.1: Return link budget parameters for the uplink.

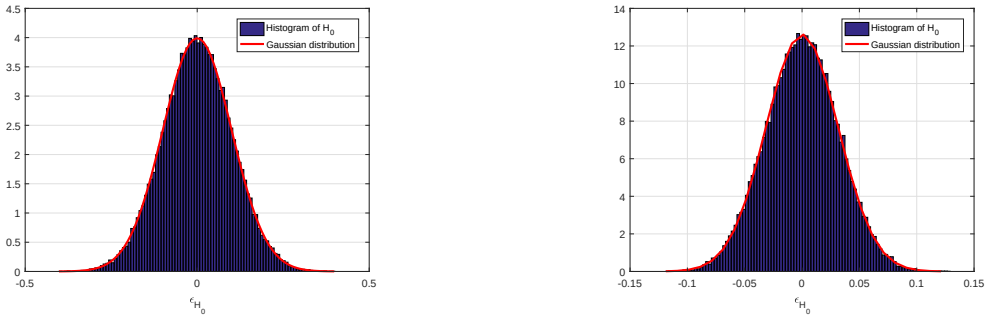

(A) Number of pilots $N_p = 10$.

(B) Number of pilots $N_p = 75$.

FIGURE 4.5: Theoretical and empirical distributions of $\varepsilon_{\mathcal{H}_0}$, with $\frac{E_p}{\sigma^2_{w_p}} = 6$ dB.

detection schemes with respect to probability of detection and compare them with the state of the art techniques such as the CED.

In all simulations, the channel is considered to be a scalar complex channel, stable for a long period (i.e. at least for the whole frame). Furthermore, the desired transmitted signal is QPSK modulated, while the noise is generated by independent identically distributed (i.i.d) complex Gaussian random variables with distribution $\mathcal{CN}\left(0, \sigma_w^2\right)$, where $\sigma_w^2 = \sigma_{w_p}^2 = \sigma_{w_d}^2$. As mentioned earlier, the reliability of the proposed detectors is based on the ability to correctly set the threshold. Therefore, for simplicity reasons, in all simulations, we assume that the interfering signal is generated by i.i.d complex Gaussian random variables with distribution $\mathcal{CN}\left(0, \sigma_i^2\right)$, where $\sigma_i^2 = \sigma_{i_p}^2 = \sigma_{i_d}^2$. Finally, it is mentioned that the interference can affect both the forward and return link, but here the presented simulation results are based on the considered return link budget of Table I, which is suitable for VSAT interference.

4.5.1 Evaluation of the channel estimation error

Here, simulation results are illustrated in order to verify that the channel estimation error $\varepsilon_{\mathcal{H}_0}$ under the hypotheses $\mathcal{H}_0$ follows a Gaussian distribution with zero mean and variance $\sigma^2_{\varepsilon_{\mathcal{H}_0}} = \frac{\sigma^2_{w_p}}{E_p}$.

Figure 4.5 depicts the histogram of the simulated channel estimation error for the scenario where the interference is absent, e.g. hypothesis $\mathcal{H}_0$. 20000 Monte-Carlo realizations are performed for the calculation of $\varepsilon_{\mathcal{H}_0}$, while the number of pilots is set to $N_p = 10$ and $N_p = 75$. These numbers are in the right range, according to DVB-RCS2 [101] for the return link, where the number of pilots for the linear modulation bursts when the adopted modulation scheme is QPSK ranges from 12 to 77. It can be observed that the simulated distribution through the histogram closely matches the theoretical Gaussian distribution for the channel estimation error. Furthermore, it can be noticed that when the number of pilots increases, the range of the values for the channel estimation error decreases. This is explained by the fact that the variance of the channel estimation error is proportionally inverse to the number of the pilots.

4.5.2 Evaluation of the probability of false alarm for both detectors

In this subsection, the theoretical expressions of (4.12) and (4.33) for the probability of false alarm of both detection schemes are verified. The relationship between the P_{FA_p} of (4.12) and the distribution of $T(\mathbf{y}'_p|\mathcal{H}'_{0_p})$ of (4.13) is the following:

$$T(\mathbf{y}'_p|\mathcal{H}'_{0_p}) \sim c_{\mathcal{H}_{0'_p}} \chi^2_{f_{\mathcal{H}_{0'_p}}} \Rightarrow P_{FA_p} = \frac{\Gamma\left(\frac{f_{\mathcal{H}'_{0_p}}}{2}, \frac{2\gamma_p}{c_{\mathcal{H}'_{0_p}}}\right)}{\Gamma\left(\frac{f_{\mathcal{H}'_{0_p}}}{2}\right)} = \frac{\Gamma\left(N_p - 1, \frac{\gamma_p}{\sigma^2_{w_p}}\right)}{\Gamma\left(N_p - 1\right)}. \tag{4.45}$$

Therefore, a reliable method for the verification of (4.12) can be obtained through the distribution of the test statistic of (4.13).

Similarly, we can verify the P_{FA_d} of (4.33) via the distribution of $T(\mathbf{y}'_d|\mathcal{H}'_{0_d})$ of (4.32) because their relationship is the following:

$$T\left(\mathbf{y}'_d|\mathcal{H}'_{0_d}\right) \sim \chi^2_{N_d}\left(\lambda\right) \Rightarrow P_{FA_d} = Q_{N_d/2}\left(\sqrt{\frac{\lambda}{\sigma^2_{w_d}}}, \sqrt{\frac{\gamma_d}{\sigma^2_{w_d}}}\right). \tag{4.46}$$

Figures 4.6 and 4.7 present the histogram of $T(\mathbf{y}'_p|\mathcal{H}'_{0_p})$ and $T(\mathbf{y}'_d|\mathcal{H}'_{0_d})$, respectively. 20000 Monte-Carlo realizations are performed, the number of pilots is set to $N_p = 10$ and $N_p = 75$, while the number of QPSK symbols is set to $N_d = 75$. It can be noticed that in both figures, the simulated distribution through the histogram aligns perfectly with the theoretical distributions of (4.13) and (4.32), verifying with this way the derived expressions for the probability of false alarm.

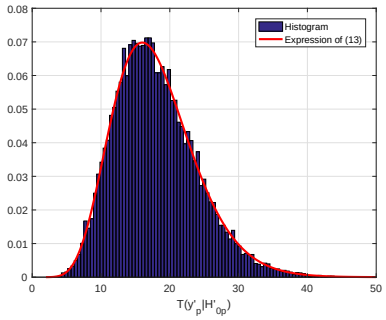

(A) $N_p = 10$.

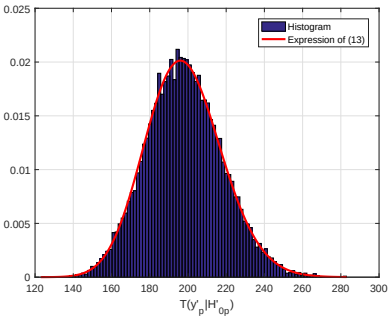

(B) $N_p = 75$.

FIGURE 4.6: Theoretical and empirical distributions of $T(\mathbf{y}'_p|\mathcal{H}'_{0_p})$, with $\frac{E_p}{\sigma^2_{w_p}} = 6$ dB.

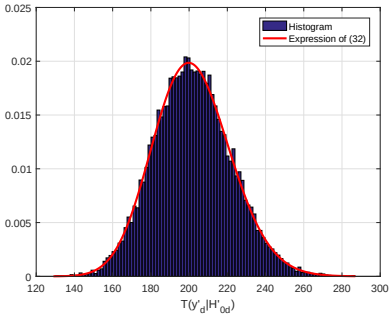

(A) $N_p = 10$ and $N_d = 75$.

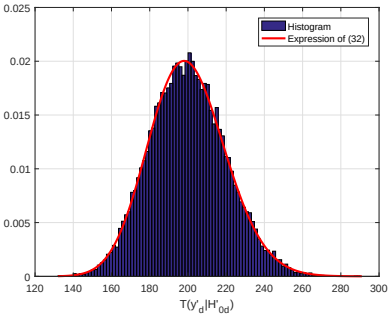

(B) $N_p = 75$ and $N_d = 75$.

FIGURE 4.7: Theoretical and empirical distributions of $T(\mathbf{y}'_d|\mathcal{H}'_{0_d})$, with $\frac{E_p}{\sigma^2_{w_p}} = \frac{E_d}{\sigma^2_{w_d}} = 6$ dB.

CED	Conventional energy detector
EDPSC	Energy detector with perfect signal cancellation
EDISC with pilots	Energy detector with imperfect signal cancellation exploiting the pilot symbols
EDISC with data	Energy detector with imperfect signal cancellation using the data
EDISC with two-stage	Two-stage energy detector with imperfect signal cancellation

TABLE 4.2: Acronyms.

4.5.3 Performance analysis with respect to probability of detection

In this part, numerical results are illustrated in order to evaluate the interference detection performance of the proposed detectors, as they are presented in Table 4.2. As mentioned earlier, it is assumed that the interfering signal follows a Gaussian distribution, while the desired transmitted signal is QPSK modulated. Furthermore, the received interference-to-signal plus noise ratio varies from -25 to 5 dB, the channel is assumed to be of unit power, while the probability of false alarm is set to $P_{FA} = 0.1$.

Figures 4.8 and 4.9 depict the probability of detection as a function of the received ISNR comparing the following detection schemes: 1) CED; 2) EDISC with pilots, 3)

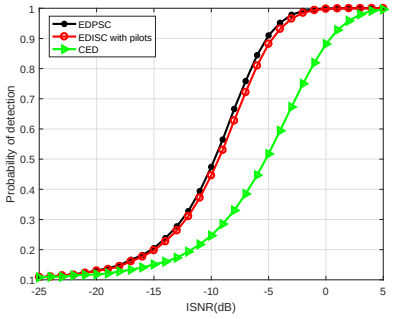

(A) $N_p = 10$.

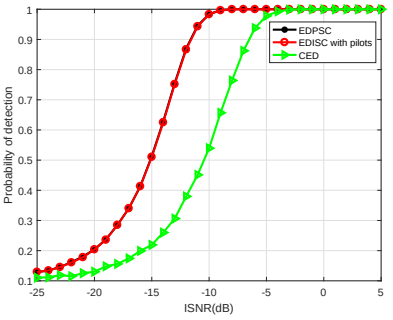

(B) $N_p = 75$.

FIGURE 4.8: Probability of interference detection versus the ISNR for the QPSK comparing the EDISC with pilots, the EDPSC and the CED, where $\frac{E_p}{\sigma^2_{w_p}} = 6$ dB.

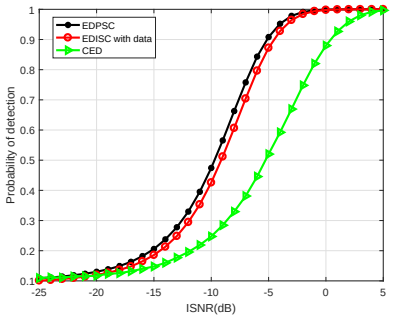

(A) $N_p = 10$, $N_d = 10$.

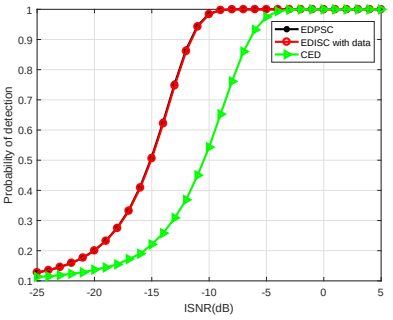

(B) $N_p = 75$, $N_d = 75$.

FIGURE 4.9: Probability of interference detection versus the ISNR for the QPSK scenario comparing the EDISC with data, the EDPSC and the CED, where $\frac{E_p}{\sigma^2_{w_p}} = \frac{E_d}{\sigma^2_{w_d}} = 6$ dB.

EDISC with data; and 4) EDPSC, for the case that the desired transmitted signal is QPSK modulated. In Figure 4.8, the number of pilots is set $N_p = 10$ and $N_p = 75$, while in Figure 4.9, the number of data symbols and pilots is set $N_d = 10$, $N_p = 10$, $N_d = 75$ and $N_p = 75$, respectively. It is observed that in both figures, the EDISC with pilots or data obtains significantly better interference detection performance than the CED. Furthermore, it can be noticed that the proposed detection schemes perform slightly worse than the case of perfect signal cancellation due to the effects of the channel estimation error. However, it can be seen that when the number of pilots increases, the interference detection performance of the EDISC with pilots or data performs closely to EDPSC. As mentioned earlier, this can be justified by the fact that the variance of the channel estimation error is inverse proportionally to the number of the pilots. Therefore, a larger number of pilots has smaller effects in the interference detection performance.

Figure 4.10 displays the probability of detection as a function of the received ISNR comparing the following detection schemes: 1) EDISC with two-stage; 2) EDISC with pilots; and 3) EDISC with data for the case that the desired transmitted signal is QPSK

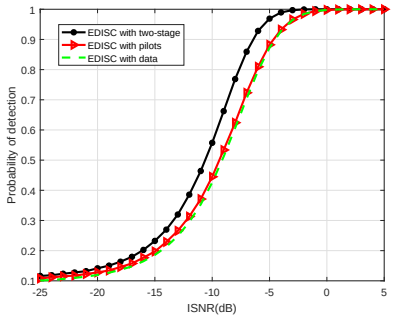

(A) $N_p = 10$, $N_d = 10$.

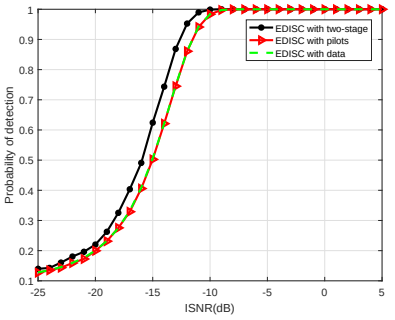

(B) $N_p = 75$, $N_d = 75$.

FIGURE 4.10: Probability of interference detection versus the ISNR for the QPSK scenario comparing the EDISC with two stage, the EDISC with pilots and the EDISC with data, where $\frac{E_p}{\sigma^2_{w_p}} = \frac{E_d}{\sigma^2_{w_d}} = 6$ dB.

modulated. In this figure, it can be seen that for an ISNR less than -5 dB (Figure 4.10a) or -10 dB (Figure 4.10b), the two-stage interference detection scheme performs better than either the EDISC with pilots or EDISC with data. Furthermore, Figure 4.10 shows that the EDISC with data behaves similar to EDISC with pilots, but as mentioned earlier its computational complexity is higher. On the other hand, the EDISC with pilots is restricted to work with a limited number of pilots. Therefore, there is a trade-off between computation complexity and interference detection performance in terms of the use of EDISC with pilot symbols or data.

Figure 4.11 presents the probability of detection as a function of the received ISNR comparing the following detection schemes: 1) EDISC with two-stage; 2) EDISC with pilots; 3) EDISC with data; and 4) CED taking into account the noise variance and signal energy uncertainties. In practice, the uncertainty factor in receiver is typically $1-2$ dB [87]. Here, it is considered that $B_p = B_{w_d} = B_{E_d} = 1$ dB, while the number of modulated symbols and pilots is set $N_d = 75$ and $N_p = 75$ for a fair comparison in Figure 4.11a, while in Figure 4.11b, they are set to $N_d = 460$, $N_p = 56$ and $N = 516$ representing a more realistic waveform according to DVB-RCS2 standard. It is observed that in both figures the interference detection performance decreases due to the uncertainty. The latter may lead to the ISNR wall phenomenon [7], where beyond a certain ISNR value the detectors cannot robustly detect the interference. Furthermore, it can be seen that the proposed interference detection schemes under the more practical scenario of uncertainty still perform considerably better than the CED with uncertainty, improving the ISNR wall by more than 5 dB.

Finally, Figure 4.12 examines the interference detection reliability of the EDISC with two-stage, the EDISC with pilots, the EDISC with data and the CED in terms of the receiver operating characteristic (ROC) curves. The ROC curves are plotted for $N_p = 75$, $N_d = 75$ and ISNR$=-12$ dB, assuming that the desired transmitted signal is

QPSK modulated. It is again observed that the proposed detection schemes perform better than the CED and that the two-stage algorithm is the most reliable interference detection scheme between them.

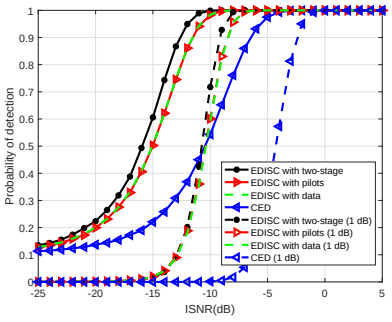

(A) $N_p = 75$, $N_d = 75$.

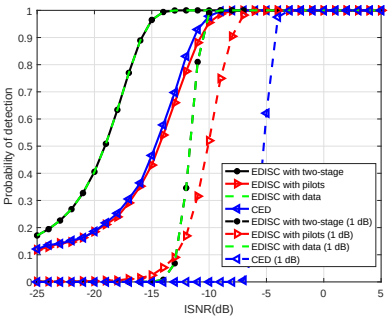

(B) $N_p = 56$, $N_d = 460$, $N = 516$.

FIGURE 4.11: Probability of interference detection versus the ISNR for the QPSK scenario comparing the EDISC with two stage, the EDISC with pilots, the EDISC with data and the CED taking into account 1 dB of noise variance and signal energy uncertainties, where $\frac{E_p}{\sigma^2_{w_p}} = \frac{E_d}{\sigma^2_{w_d}} = 6$ dB.

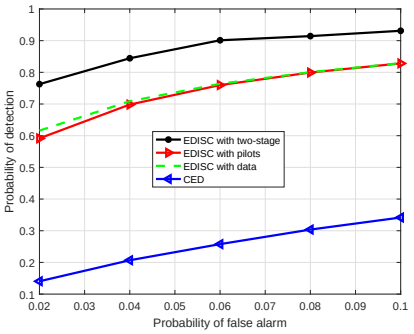

FIGURE 4.12: ROC curves for the EDISC with two-stage, the EDISC with pilots, the EDISC with data and the CED, where $N_p = 75$, $N_d = 75$, ISNR=-12 dB, $\frac{E_p}{\sigma^2_{w_p}} = \frac{E_d}{\sigma^2_{w_d}} = 6$ dB.

4.6 Summary

In this chapter, the detection of interference in the satellite communication signals was investigated and interference detection algorithms that can be implemented as a spectrum monitoring unit on-board a satellite were developed. Furthermore, two algorithms for the detection of weak interfering signals were proposed, as the handling of the aggregated low power VSAT interference is the most crucial for the commercial satellite industry. The first algorithm is well suited to DTP satellite payloads, whereas the second algorithm is well suited to Hybrid DTP/Regenerative satellite payloads. Both algorithms are based on energy detection with imperfect signal cancellation exploiting

the pilot or data symbols, respectively. Analysis how the imperfect signal cancellation due to the channel estimation error affects the sensing reliability of both detection schemes was carried and the theoretical expressions for the probabilities of false alarm and probability of detection were derived. Numerical results demonstrated that both detection schemes obtain better interference detection performance compared to conventional energy detector (more than 5 dB gain is achieved by the proposed algorithms). Finally, it was shown that the two-stage detector can achieve better performance than the detector based on the pilots as it uses a larger number of samples, however, it is more computationally complex.

Chapter 5

Lab Demonstration of Interference Detection

While the developed algorithms have been evaluated using powerful simulations extensively, the objective of this chapter is to go one step further and evaluate the performance of the developed algorithms experimentally using SDR. An SDR is a communications platform that uses software for fast prototyping of digital communications algorithms, while allowing analog transmissions over a physical medium. In this thesis, the NI USRP platforms have been utilized as the SDR. USRPs are computer-hosted software radios which provide a powerful hardware platform for lab experiments. Due to their simple programmability as well as inexpensiveness, they have been used extensively by research labs and universities for radio technology experiments. They can perform as radio transceivers and the required signal processing algorithms can be programmed using generic programming languages including MATLAB, LabVIEW and C.

5.1 Universal Software Radio Peripheral

The USRPs [102], [103] are inexpensive programmable radio platforms which can be used in a plethora of applications such as, spectrum monitoring, record and playback, communications, cognitive radio, physical layer prototyping and wireless communications teaching and research. The USRP consists of two main features: 1) the hardware; and 2) the software. The latest models of USRP offer larger bandwidth, more RF ports, and a faster processor. For the used model of the USRP, the software is programmed by the user, who defines the complete communication system and sets important parameters.

FIGURE 5.1: NI USRP-2954R (courtesy of NI [104]).

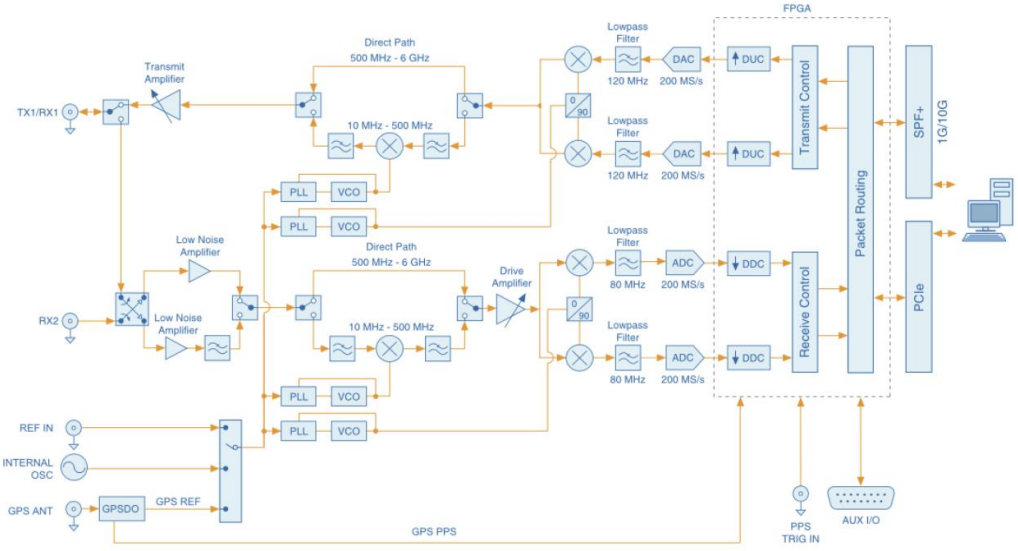

FIGURE 5.2: Functional block diagram of NI USRP-2954R (courtesy of NI [105]).

5.1.1 USRP hardware

The NI USRP-2954R is used, which is considerable choice for wireless communications designers in terms of cost and performance. This USRP, depicted in Figure 5.1, consists of a 2x2 multiple input, multiple output (MIMO) RF transceiver with a LabVIEW programmable DSP oriented Kintex-7 field programmable gate array (FPGA), proper for high-rate and low-latency applications [104]. LabVIEW provides a friendly design flow for wireless communications researchers, helping them to prototype faster and obtain results on shorter time.

More details about the functionality of the NI USRP-2954R are presented in Figure 5.2. Signals transmitted by the NI USRP-2954R are upsampled, reconstructed, filtered,

Parameter	**Value**
Frequency range	10 MHz to 6 GHz
Maximum output power (P_{out})	50 mW to 100 mW (17 dBm to 20 dBm)
Maximum input power (P_{in}	-15 dBm
Maximum instantaneous real-time bandwidth	160 MHz
Maximum I/Q sample rate	200 MS/s
Digital-to-analog converter	2 channels, 200 MS/s, 16 bit
Analog-to-digital converter	2 channels, 200 MS/s, 14 bit

TABLE 5.1: Hardware characteristics of NI-USRP-2954R [106].

upconverted and amplified before being transmitted. On the other hand, signals received by the NI USRP-2954R are amplified, downconverted, filtered, digitized and decimated before being passed to the host computer.

For the transmission, the host computer synthesizes the baseband in-phase (I) and quadrature-phase (Q) signals and transmits the signals to the device over a standard PCIe connection. The signal is mixed, filtered and interpolated to 200 MS/s by a digital up-converter (DUC). Then, the signal is converted to analog through a DAC and a low-pass filter (LPF) is used to reduce the noise and the high frequency components in the signal. The signal is upconverted by a mixer, while the phase-locked loop (PLL) controls the voltage-controlled oscillators (VCO) so that the device clocks and LO can be frequency-locked to a reference signal. Subsequently, the signal travels through either a direct conversion path or a down conversion path, depending on the frequency. Finally, the signal is amplified and transmitted through the antenna.

In the receiver's side, the incoming signal is amplified through either an LNA or an LNA-LPF combination, depending on the incoming frequency. Then, the signal travels through either a direct conversion path or an up-conversion path, depending again on the frequency, and the signal is amplified by a final driver amplifier. The PLL controls the VCO so that the device clocks and LO can be frequency-locked to a reference signal. Subsequently, the signal is downconverted to the baseband I and Q components by the quadrature mixer and the LPF is used to reduce the noise and the high frequency components in the signal. Then, the signal passes through the ADC, which digitizes the I and Q data. Finally, the signal is mixed, filtered and decimated to a user's specified rate by a digital down-converter (DDC) and the down-converted samples are transported to the host computer over a standard PCIe connection.

Furthermore, another interesting characteristic of the NI USRP-2954R is its hardware characteristics, which are summarized in Table 5.1.

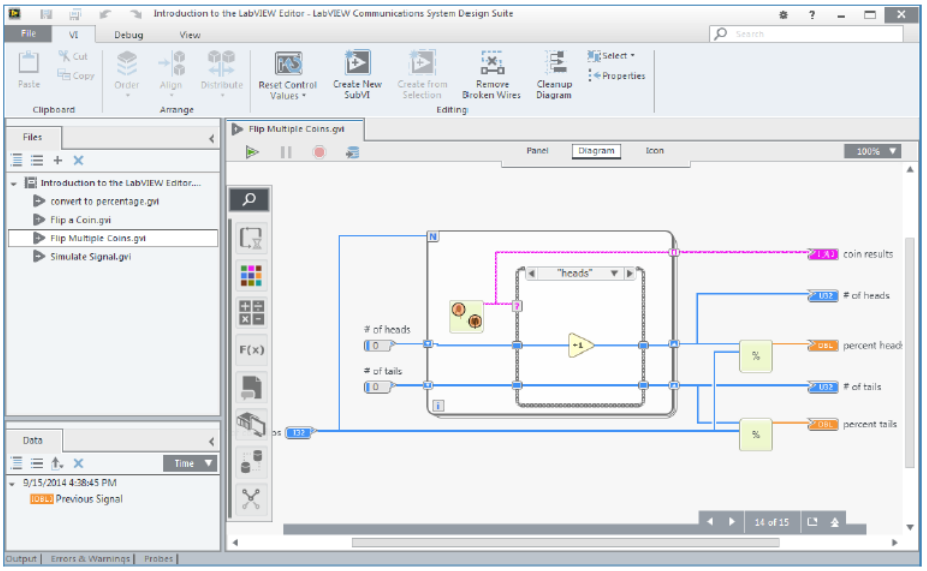

FIGURE 5.3: Editor of LabVIEW Communications System Design Suite 2.0.

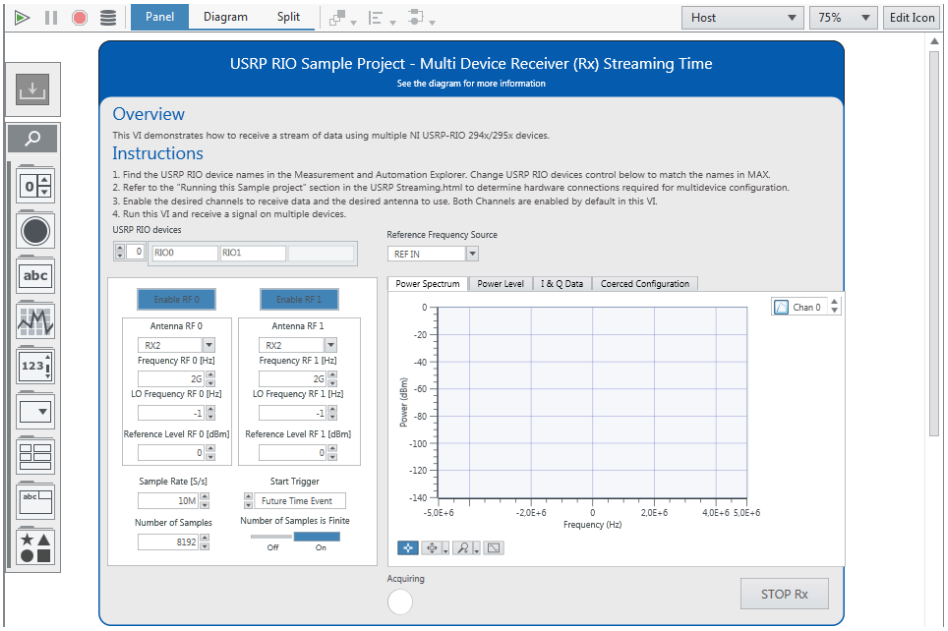

FIGURE 5.4: Example of a GUI automatically created through LabVIEW Communications System Design Suite 2.0.

5.1.2 USRP software

The software platform in order to program the USRPs is the LabVIEW Communications System Design Suite 2.0 [107], [108]. It provides a friendly design environment closely

Parameter	Value
Modulation type	QPSK
Sample rate	1M samples/second
Bandwidth	400KHz
TX to Emulator carrier frequency	10 MHz
Emulator to RX carrier frequency	10 MHz
RX carrier frequency	10 MHz
Over-sampling factor	4
Pulse-shaping filter	root-raised cosine with 0.5 roll-off
Multi-tone preamble	320 samples
Data	500 symbols or 2000 data samples

TABLE 5.2: Experimental parameters for the transmission and reception in a single input-single output (SISO) system.

integrated with NI SDR hardware for faster prototyping communications systems. Furthermore, it enables users to program both the processor and FPGA. In this thesis, the main part of the processing is done based on observations obtained by USRPs in powerful computers since the implementation does not suffer from latency issues. The environment for editing of LabVIEW Communication System Design Suite 2.0 is shown in Figure 5.3.

Furthermore, Figure 5.4 shows an example of the graphical user interface (GUI) in this integrated development environment (IDE). This comes basically for free since the project created, automatically associates the I/O blocks on the developed model based code to the already implemented I/O plots/bar/windows in a panel which can be further improved by the user.

5.2 Building a Real Communication System with USRPs

In this section, a demonstrator of a realistic communication system with USRPs is built. The demonstrator consists of one transmitter, one channel emulator and one receiver. Furthermore, a Hub is used in order to enable the same computer to process more than one USRPs simultaneously. A picture of this experimental set-up is depicted in Figure 5.5. Now, we will analyze it with more details starting by building up the transmitter, then the channel emulator and we will conclude with the receiver. Table 5.2 shows a summary of the parameters of this demonstrator. Here, it should be mentioned that the selected carrier frequencies of the transmitter and receiver are set to 10 MHz in order to decrease the mutual coupling between the transmission and reception links.

5.2.1 Transmitter

The full transmitter is shown in the flowchart in Figure 5.6. It consists of two parts: 1) the components generated by the host with the aid of LabVIEW; and 2) the components which take place in the NI USRP-2954R. Starting on the left of Figure 5.6, a random sequence of bits is generated. Then, these bits are mapped to QPSK constellation. Next, the baseband signal is upsampled to our desired sample rate and then run the data through the pulse-shaping filter. After the host has synthesized the I/Q signals, they are ready to pass to the transmitted device. There, as mentioned earlier, the digital up-converter mixes, interpolates and filters the signal, while the DAC converts it to analog signal. Then, the signal is upconverted and finally, is amplified and transmitted through the cables to the channel emulator.

5.2.1.1 Generating bits and mapping symbols

Producing the bits is a very simple task by using the LabVIEW function "MT Generate Bits". This function generates Galois pseudonoise bit sequences, where the selected pattern is repeated by the node until the generation of the number of total bits that we specify, as shown in Figure 5.7.

Once we have the bits, we are ready to map them to our modulation symbols. For this lab demonstrator, QPSK is the chosen modulation scheme. The mapping is obtained by

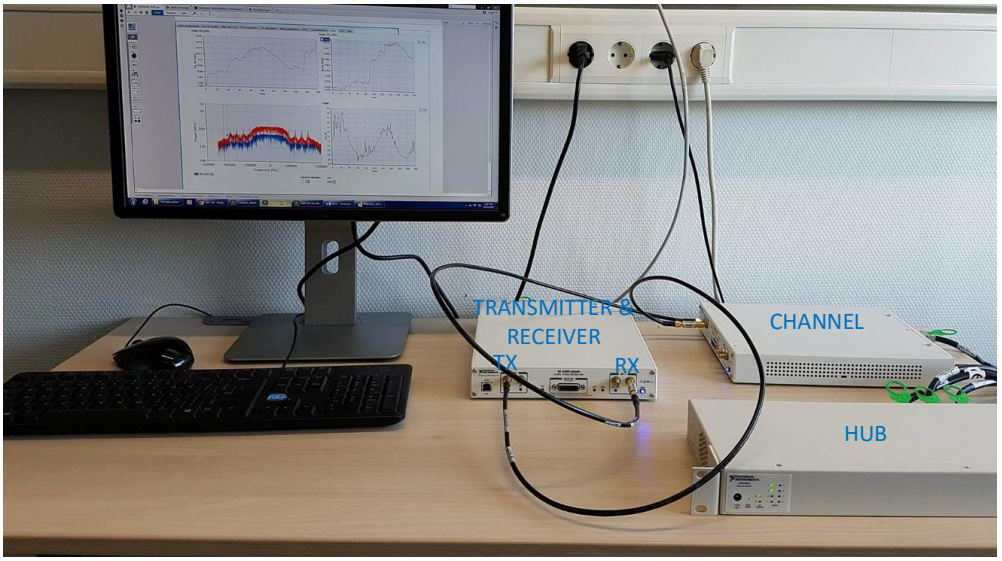

FIGURE 5.5: Experimental set-up, where the SDR platform used for transmitter, channel emulator and receiver is the NI USRP-2954R.

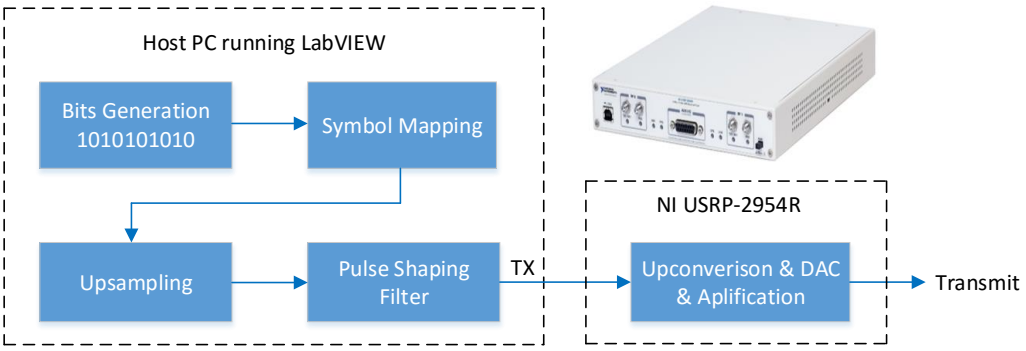

FIGURE 5.6: Flowchart showing the generation of a digitally modulated waveform and the transmitted signal.

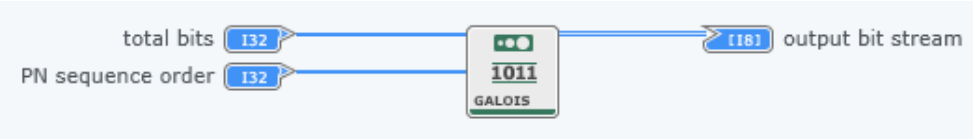

FIGURE 5.7: Bits generation in LabVIEW.

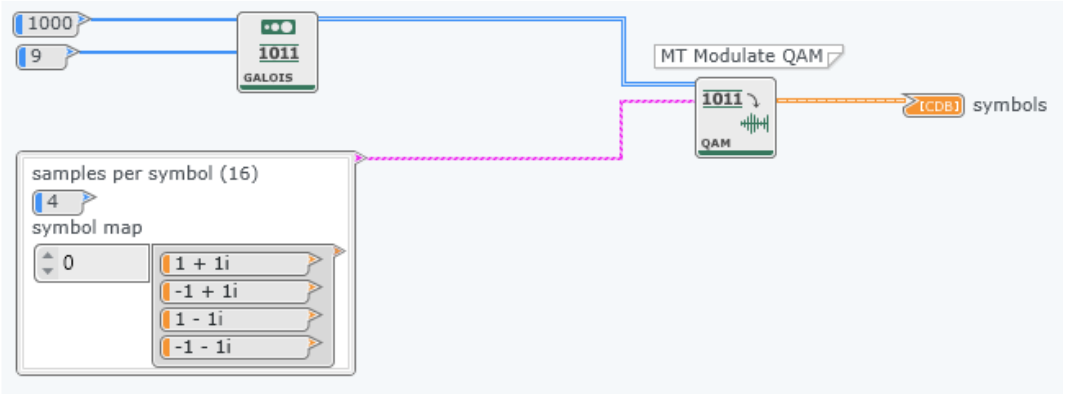

FIGURE 5.8: QPSK symbol mapper in LabVIEW.

using the LabVIEW function "MT Modulate QAM". This function receives a sequence of data bits and one of its operations is to map the bits to QAM symbols. This is obtained by using a symbol table which is formed with the symbols in Gray encoded order and the proper symbol is selected by indexing this array of symbols with the bits to transmit. Figure 5.8 shows this QPSK symbol mapper.

5.2.1.2 Upsampling and Pulse-shaping filter

Then, we design a pulse-shaping filter for a given length, sample rate, symbol rate and roll-off factor. The pulse-shaping filter is used to combat the intersymbol interference

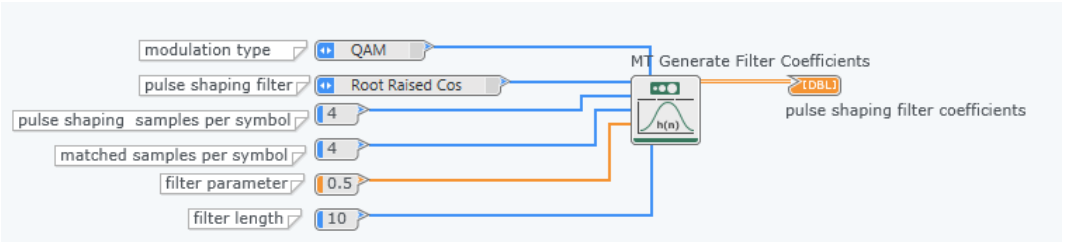

FIGURE 5.9: Design of root-raised cosine filter in LabVIEW.

(ISI) [45]. Nyquist has developed a criterion for choosing a filter that is guaranteed to have zero ISI. One such filter is the root-raised cosine filter [45] with the following impulse response $g(t)$:

$$g(t) = \begin{cases} \frac{1}{T_s}\left(1+\alpha\left(\frac{4}{\pi}-1\right)\right), & t=0 \\ \frac{\alpha}{T_s\sqrt{2}}\left(\left(1+\frac{2}{\pi}\right)\sin\left(\frac{\pi}{4\alpha}\right)+\left(1-\frac{2}{\pi}\right)\cos\left(\frac{\pi}{4\alpha}\right)\right), & t=\pm\frac{T_s}{4\alpha} \\ \frac{1}{T_s}\dfrac{sin\left(\pi\frac{t}{T_s}(1-\alpha)\right)+4\alpha\frac{t}{T_s}cos\left(\pi\frac{t}{T_s}(1+\alpha)\right)}{\pi\frac{t}{T_s}\left(1-\left(4\alpha\frac{t}{T_s}\right)^2\right)}, & otherwise \end{cases}.$$

The root-raised cosine filter coefficients are obtained by using the LabVIEW function "MT Generate Filter Coefficients" as shown in Figure 5.9.

5.2.1.3 Transmitted waveform to the USRP

Subsequently, we generate the modulated complex baseband waveform, which should be ready to pass to the transmitted device. This is achieved by the combination of the

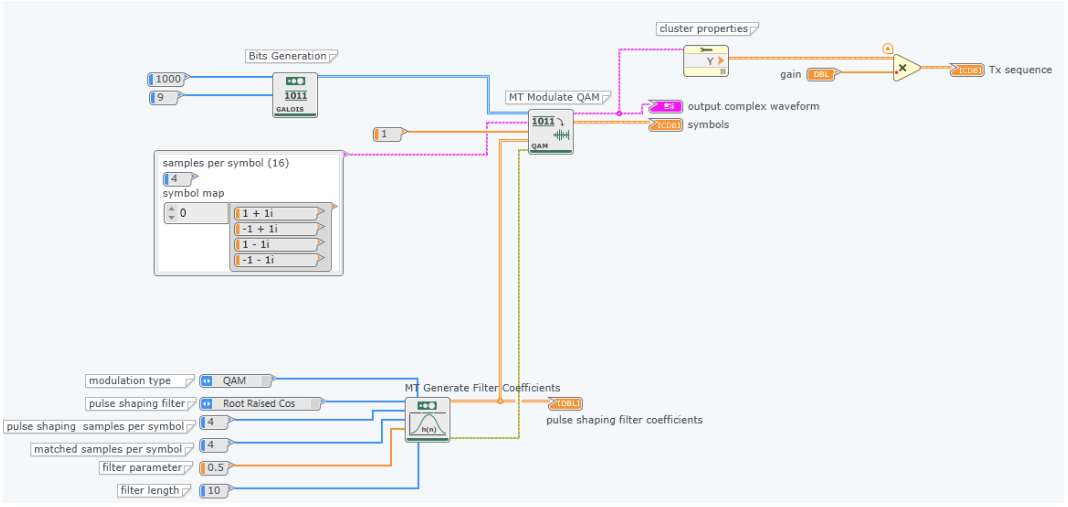

FIGURE 5.10: Generation of the modulated complex baseband waveform.

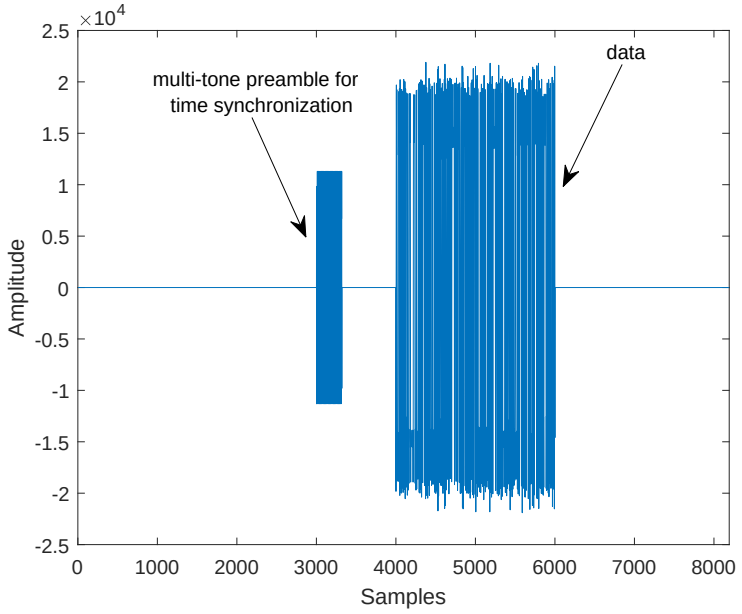

FIGURE 5.11: Transmitted waveform before passing to the USRP.

aforementioned blocks, as shown in Figure 5.10. Furthermore, Figure 5.11 illustrates the transmitted waveform before passing to the device. In this figure, we can notice that there are two distinct signals: 1) the signal related to frame synchronization; and 2) the data.

Preamble

One of the most important functions of the receiver is the synchronization. As we will discuss later in this chapter the synchronization issues have two aspects: 1) time; and 2) frequency synchronization. One method to address the time synchronization is to insert a known preamble at the beginning of a transmission. A proposed method is the design of a multi-tone preamble, which offers robustness in frequency-selective fading channels [109], [110], [111]. Therefore, this is the reason that we can see the two different waveforms in Figure 5.11, one for the multi-tone preamble and another one for the information data. At the receiver, the time synchronization is obtained by finding the instant at which the cross-correlation of the known multi-tone preamble and the received signal reaches in its peak.

5.2.1.4 Transmitted signal from the USRP

Finally, one important task is to open and configure the USRP and prepare it to process the synthesized by the host I/Q signals, as shown in Figure 5.12. Then, the process

of up-conversion, DAC and amplification is performed in the USRP and the signal is transmitted through the cables to the channel emulator.

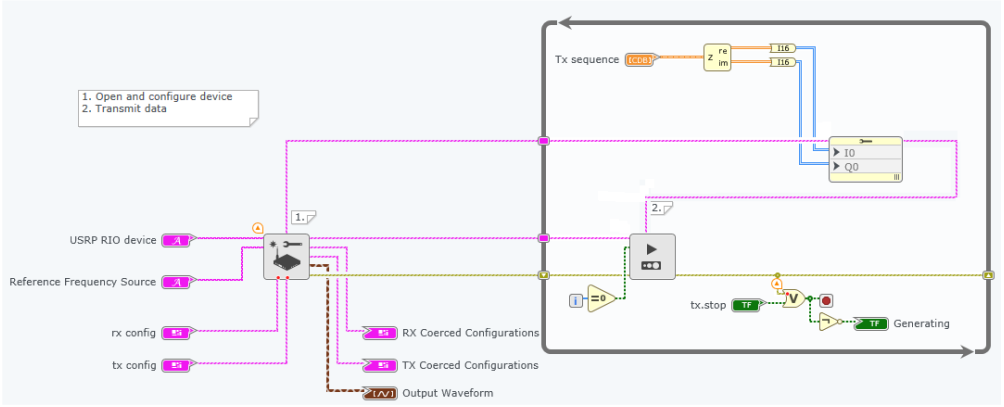

FIGURE 5.12: Configuration of the USRP and ready for transmission.

5.2.2 Channel emulator

The transmitted signal is sent to the channel emulator, which injects to the signal an AWGN with a controlled power and then is sent to the receiver. The channel functionalities are implemented in an FPGA which is integrated to the SDR platform. This implementation has been done by the SIGCOM (Signal Processing and Communications) Research group from the University of Luxembourg, so here, we used it as a built-in function.

5.2.3 Receiver

The functionality of the receiver is shown in Figure 5.13. It is the reverse process of the transmitter with the additional pieces of synchronization. Again, the receiver consists of two parts: 1) the components which take place in the NI USRP-2945R; and 2) the components generated by the host and the aid of LabVIEW. At the receiver, the incoming signal is amplified by an LNA and downconverted to the baseband in-phase and quadrature phase components. Then, the signal passes through the analog-to-digital converter and transported to the host computer. In the host, the first thing the receiver needs to do is the time synchronization in order to know where the waveform begins and where to start the pulse shaping filter. Then, we downsample the signal and finally, we attempt to recover the transmitted waveform and detect the symbols and bits.

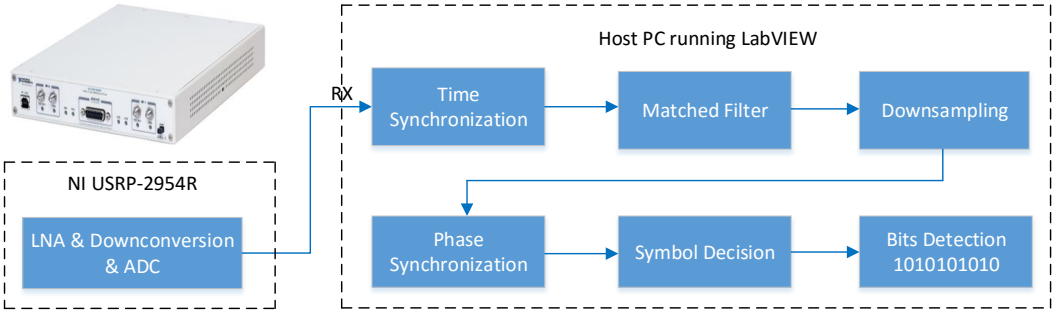

FIGURE 5.13: Flowchart showing the demodulation process of a digitally modulated waveform.

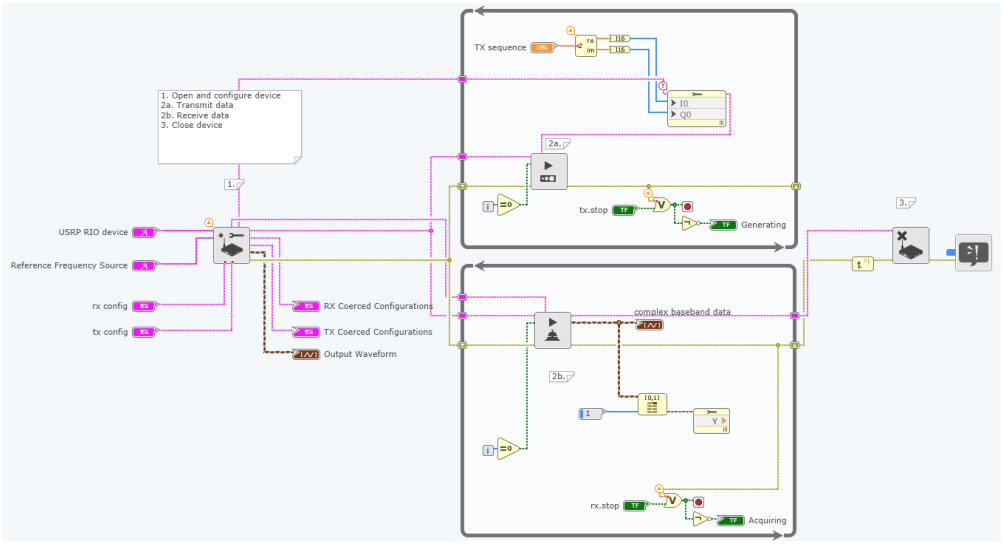

FIGURE 5.14: Configuration of the USRP in preparation for reception.

5.2.3.1 Received signal from the USRP

We showed earlier how to configure the USRP and prepare it in order to transmit the signal. Now, another important task is to enable the USRP to receive and process the signal from the transmitter. This is obtained as shown in Figure 5.14. Then, the incoming signal is amplified, downconverted and analog-to digital converted inside the USRP, where finally, the samples are transported to the host computer for further processing. This received signal at the host is presented in Figures 5.15 and 5.16 for two different signal-to-noise ratio (SNR): 1) 30 dB; and 2) 8 dB, respectively. In both cases, obviously, we can see that the beginning of the transmitted signal is different compared to that of the received signal in Figure 5.11. Therefore, the time synchronization is necessary.

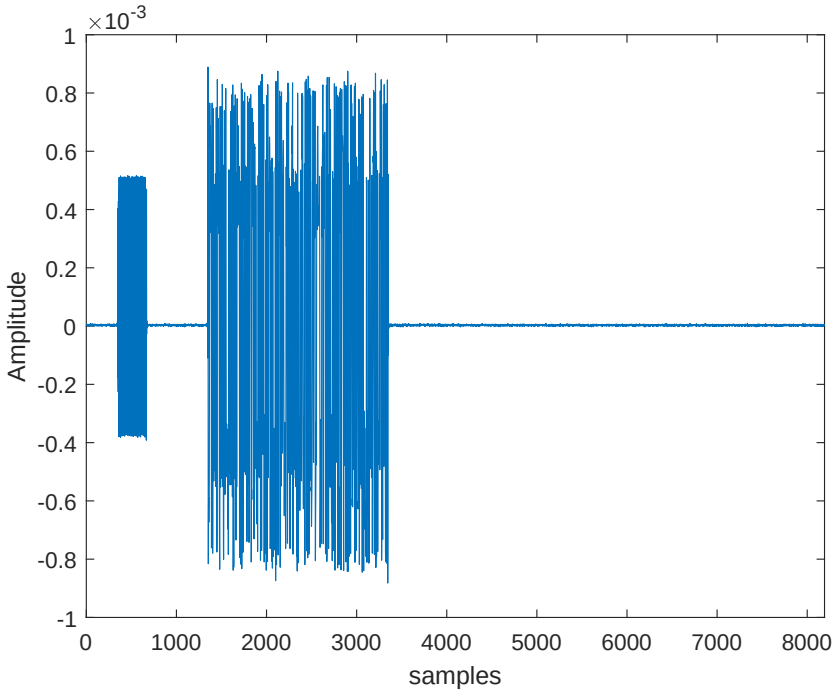

FIGURE 5.15: Received signal at the host with SNR=30 dB.

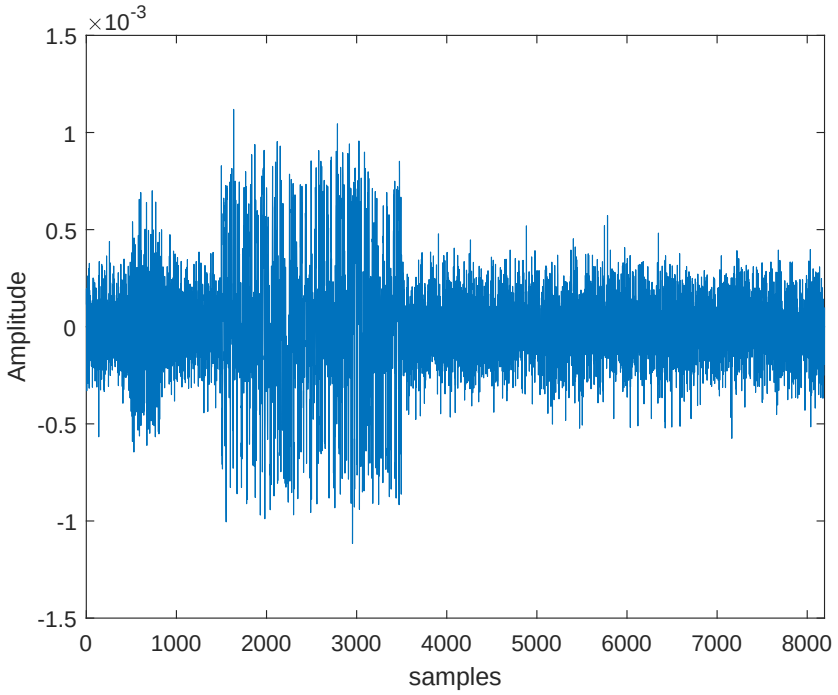

FIGURE 5.16: Received signal at the host with SNR=8 dB.

5.2.3.2 Synchronization

Synchronization is a very important part in digital communications [45] as the receiver needs to know where the waveform begins and where to start the pulse-shaping filter.

If the receiver starts receiving somewhere in the middle of a transmission or if we do not know which symbol was in the beginning of a transmission, we understand that the proper recovery of the bits is almost impossible. There two important aspects related to synchronization: 1) time; and 2) frequency synchronization.

To overcome the issue of time synchronization, a signal, known as preamble, can be embedded at the beginning of a transmission [112], [113]. This signal should be different from our data signals, otherwise we will get false matches. Therefore, we should choose a very distinct signal, which has almost no correlation with any of our data symbols and is known and just append that signal to the beginning of every transmission. Then, a matched filter is used at the receiver, where the peak of its output will give a good estimate about the position of our embedded synchronization symbol and thus the beginning of our transmission [108].

As for the frequency synchronization, it is as important as the time synchronization mentioned previously. Any frequency error will result in a phase rotation on the recovered symbols. For the estimation of the frequency error, we can embed a specific symbol at known places in our transmission. These symbols will have known phases, which can be employed as references to compute the phase error of the recovered symbols. Then, the frequency offset can be estimated by adding the phase error over the duration of the transmission.

5.2.3.3 Matched filter and downsampling

As discussed earlier, the choice of the root-raised cosine filter at the transmitter satisfies the Nyquist criterion and therefore guarantees ISI-free transmission. However, at the receiver side, the best option is the use of a matched filter, which guarantees optimal error performance at the receiver output, maximizing the signal-to-noise ratio [45]. The matched filter coefficients are obtained by using again the LabVIEW function "MT Generate Filter Coefficients" as shown in Figure 5.17. Next we downsample the signal to arrive at what should be the transmitted symbols.

5.2.3.4 Phase synchronization and symbol decision

Finally we have come to the point where we can attempt to recover our transmitted waveform. This is obtained by using the LabVIEW function "MT Demodulate QAM" as shown in Function 5.18. This function needs as inputs: 1) the baseband oversampled complex waveform after the time synchronization; 2) the QPSK system parameters, namely a symbol table and a specific symbol rate; 3) the matched filter coefficients ;

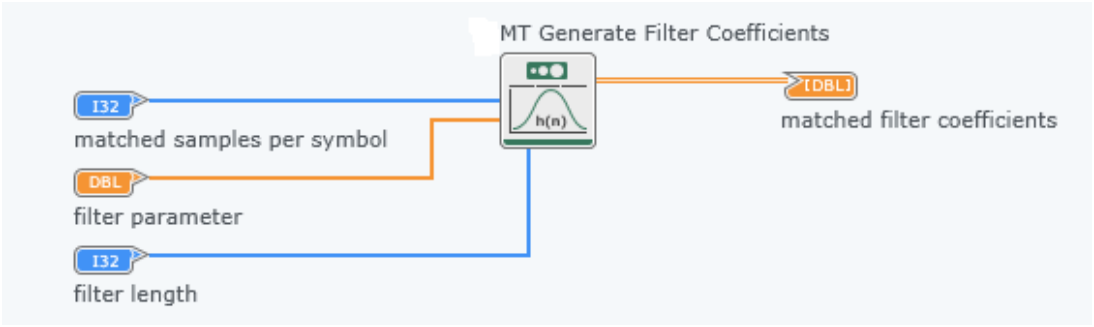

FIGURE 5.17: Design of matched filter coefficients in LabVIEW.

and 4) the synchronization parameters proper for the phase synchronization, namely known symbols at known places in our transmission. After providing these inputs, the function demodulates the QPSK modulated complex baseband waveform and returns the time and phase aligned downsampled complex waveform and the demodulated bit stream. Figures 5.19 and 5.20 present the constellation of our signal after the process of matched filtering and time and phase synchronization for SNR=8 dB and SNR=30 dB, respectively.

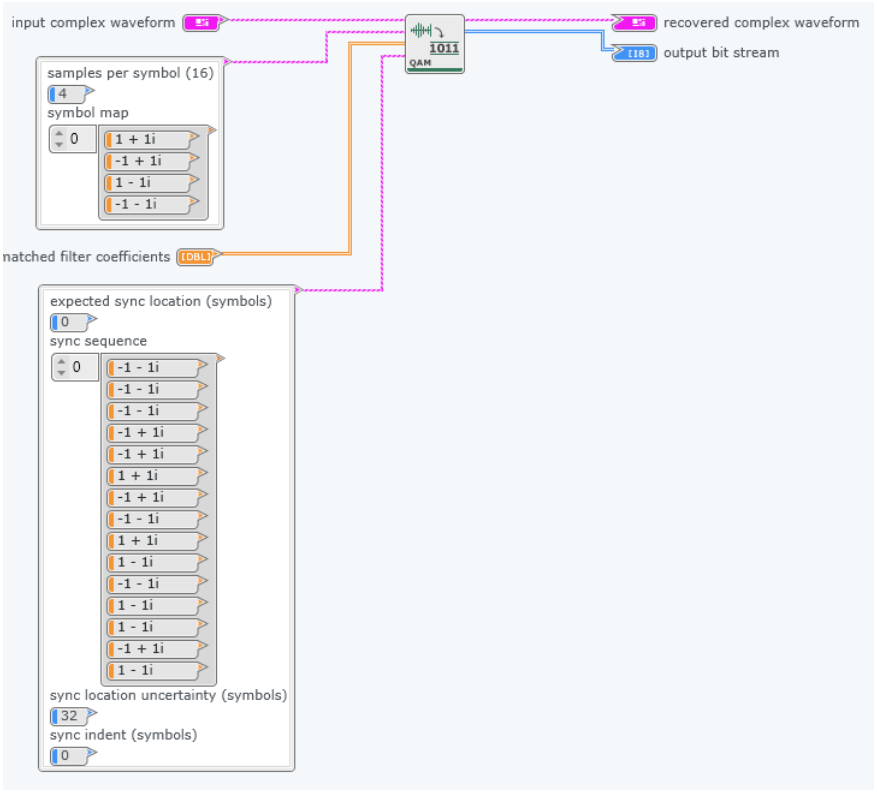

FIGURE 5.18: QPSK Demodulator.

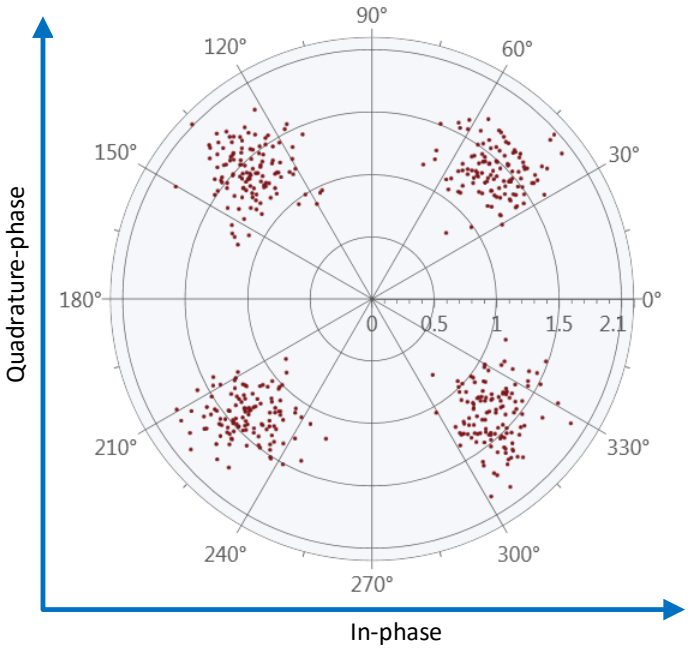

FIGURE 5.19: QPSK RX constellation for SNR=8dB with phase synchronization.

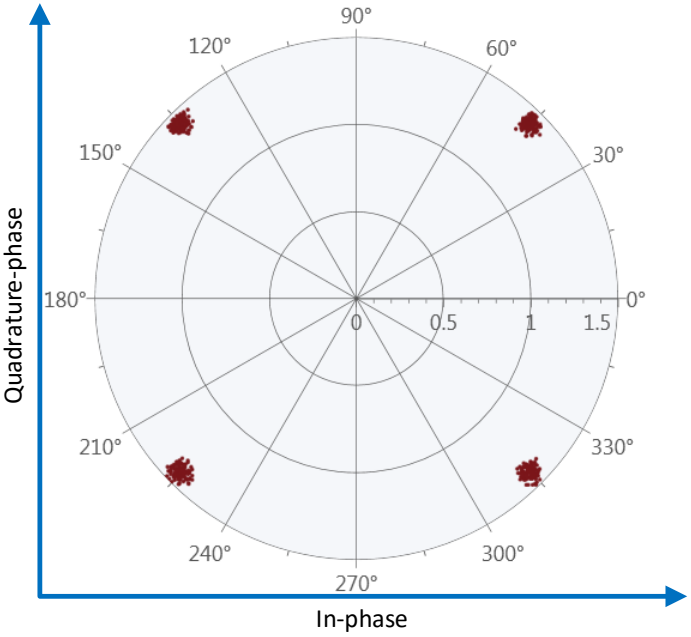

FIGURE 5.20: QPSK RX constellation for SNR=30dB with phase synchronization.

5.3 Building a Real Communication System for Interference Detection using USRPs

In this section, we build a demonstrator of a real communication system for the detection of interference using USRPs. The demonstrator consists of one transmitter, one interferer, one channel emulator and one receiver. A picture of this experimental set-up is depicted in Figure 5.21. The NI USRP-2954R has two RF transmitters. Therefore, as shown in Figure 5.21, the TX1 port is used for the generation of the desired signal, while the TX2 port is used for the generation of the interference. Furthermore, the desired signal is sent to the channel emulator, which injects to the signal AWGN noise with a controlled power. With this controlled artificial noise, we can adjust the desired SNR. Then, this signal and the interference added in their analog waveforms through a connector and the resulting signal is sent to the RX port of the USRP for further processing.

Most of the pieces in Figure 5.21 were described in the previous section, so here, we focus on the design of the interference and the implementation of the developed algorithms for its detection. The experimental parameters are same as in Table 5.2.

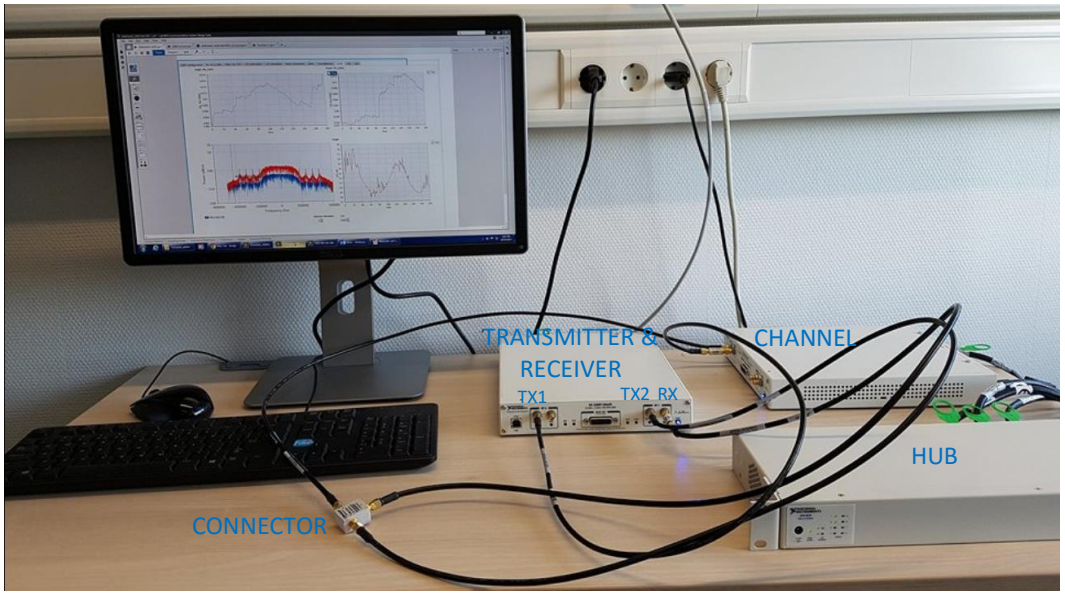

FIGURE 5.21: Experimental set-up for interference detection, where the SDR platform used for transmitter, interferer, channel emulator and receiver is the NI USRP-2954R.

5.3.1 Implementation for the calculation of the probability of false alarm in real time

The goal of this thesis is to develop some novel algorithms for the detection of interference. As mentioned many times earlier, the most important factor for the design of these detection algorithms is the proper derivation of the decision threshold, which is independent from the distribution of the interfering signal. Therefore, for the calculation of the decision threshold we focus on the hypothesis $\mathcal{H}_0$, where the interference is absent. Hence, in the beginning (until the derivation of the decision threshold), the TX2 port of Figure 5.21 does not generate interference and then, the adopted experimental set-up is more similar with that in Figure 5.5.

Now, using this set-up, we implement the methodology for the derivation of the threshold and the probability of false alarm of three algorithms. First, we start with the energy detector with imperfect signal cancellation exploiting the pilot symbols, we continue with the energy detector with imperfect signal cancellation taking into account the decoding errors and we conclude with the conventional energy detector.

5.3.1.1 Probability of false alarm for the EDISC exploiting the pilot symbols

Once we acquire the time and phase aligned downsampled complex waveform, we know the positions of the pilots in this received signal. Therefore, we extract the samples related to the position of the pilot symbols. Then, we estimate the channel using a least square estimator and remove the original pilots from the extracted received signal. Finally, we apply an ED in the remaining signal. This methodology is described in the block diagram of Figure 5.22.

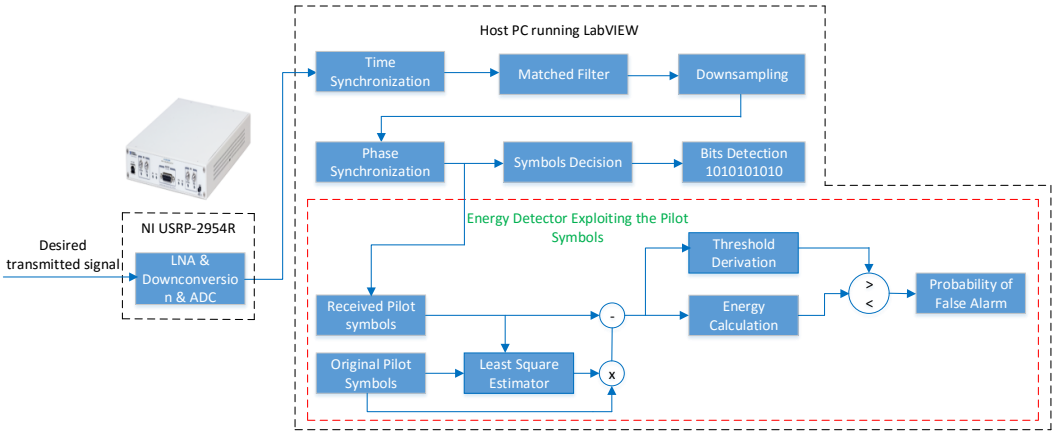

FIGURE 5.22: Flowchart showing the methodology for the calculation of the probability of false alarm of the EDISC exploiting the pilots.

Least Square Estimator

The least square estimator for the channel estimation is obtained in LabVIEW as shown in Figure 5.23. This program requires two inputs: 1) the received pilot symbols which we know once we have the time and phase aligned downsampled complex waveform; and 2) the known sequence of the original pilots. Then, this program returns the estimation of the channel.

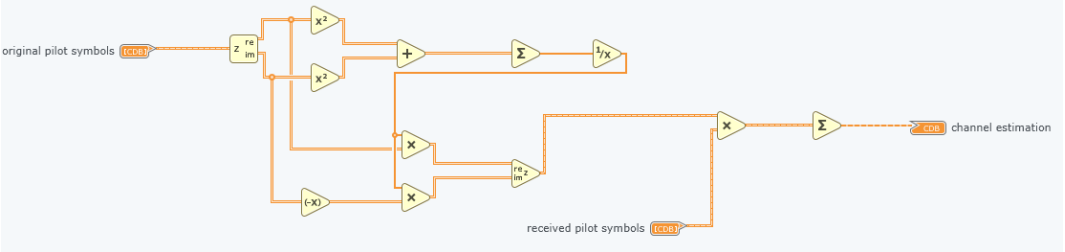

FIGURE 5.23: Least square estimator in LabVIEW.

Energy Calculation

The energy of a signal is obtained in LabVIEW as shown in Figure 5.24. This program needs as input a sequence of samples, which in this case are the remaining samples after the pilots cancellation and it returns the energy of this sequence.

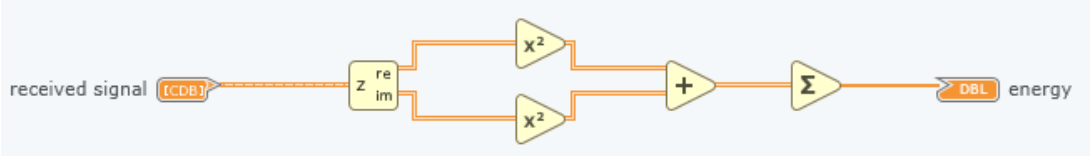

FIGURE 5.24: Energy calculation in LabVIEW.

Regarding the block of the threshold derivation, two methods have been used: 1) derivation of the decision threshold based on the theoretical formula; and 2) derivation of the decision threshold based on a more practical approach.

Implementation for the derivation of the decision threshold based on the theoretical formula

We showed in previous chapters that the probability of false alarm of the energy detector with signal cancellation exploiting the pilot symbols, in this case P_{FA_p}, is given by

$$P_{FA_p} = \frac{\Gamma\left(N_p - 1, \frac{\gamma_p}{\sigma^2_{w_p}}\right)}{\Gamma\left(N_p - 1\right)}. \tag{5.1}$$

The derivation of the threshold γ_p based on (5.1) requires the inverse incomplete gamma function. However, the implementation of the latter in LabVIEW is very difficult. For this reason, we derive an approximated formula for the P_{FA_p} using the central limit theorem. Then, the approximated probability of false alarm of the energy detector with signal cancellation exploiting the pilot symbols, in this case $P_{FA_{papr}}$, is given by

$$P_{FA_{papr}} = Q\left(\frac{\gamma_p - \left(N_p - 1\right)\sigma^2_w}{\sqrt{\left(N_p - 1\right)\sigma^2_w\sigma^2_w}}\right), \tag{5.2}$$

and the threshold is derived as follows:

$$\gamma_p = Q^{-1}\left(P_{FA_{papr}}\right)\sqrt{\left(N_p - 1\right)\sigma^2_w\sigma^2_w} + \left(N_p - 1\right)\sigma^2_w. \tag{5.3}$$

Therefore, we have to implement one function in LabVIEW, which calculates the inverse Q function. This is obtained as shown in Figure 5.25.

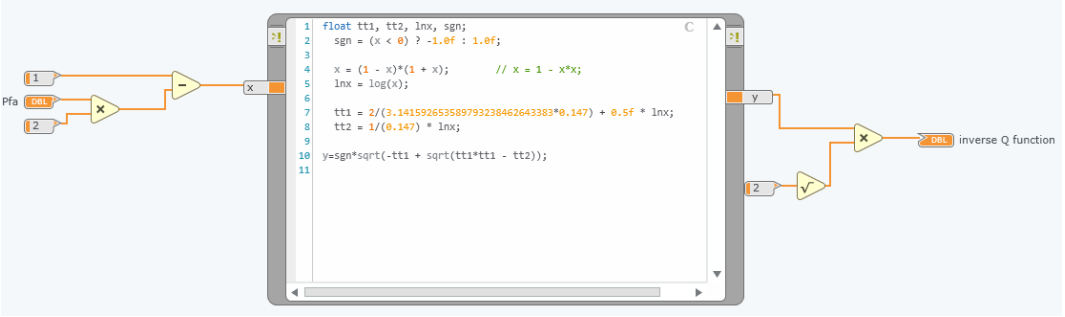

FIGURE 5.25: Inverse Q function in LabVIEW.

Furthermore, from (5.3), it is obvious that the threshold γ_p depends on the noise variance σ^2_w, which is unknown in practice, and hence has to be estimated. As mentioned earlier, after the frame synchronization, the original pilot symbols are removed from the received samples related to the position of the pilot symbols and then, the hypothesis $\mathcal{H}_0$ is

written as:

$$\mathcal{H}'_{0_p}: \quad \mathbf{y}'_p = \mathbf{w}_p - \varepsilon_{\mathcal{H}_0} \mathbf{s}_p. \tag{5.4}$$

For a large number of pilots ($N_p > 100$) the channel estimation is almost accurate, hence the channel estimation error $\varepsilon_{\mathcal{H}_0}$ is negligible and the above hypothesis can be simplified into the following one:

$$\mathcal{H}'_{0_p}: \quad \mathbf{y}'_p = \mathbf{w}_p. \tag{5.5}$$

In this case, the log-likelihood function (LLF) under $\mathcal{H}'_{0_p}$ can be expressed as

$$\ln p\left(\mathbf{y}'_p | \mathcal{H}'_{0_p}, \sigma_w^2\right) = -\frac{N_p}{2} \ln\left(2\pi\sigma_w^2\right) - \frac{1}{2\sigma_w^2} \sum_{n=1}^{N_p} \left|y'_p(n)\right|^2. \tag{5.6}$$

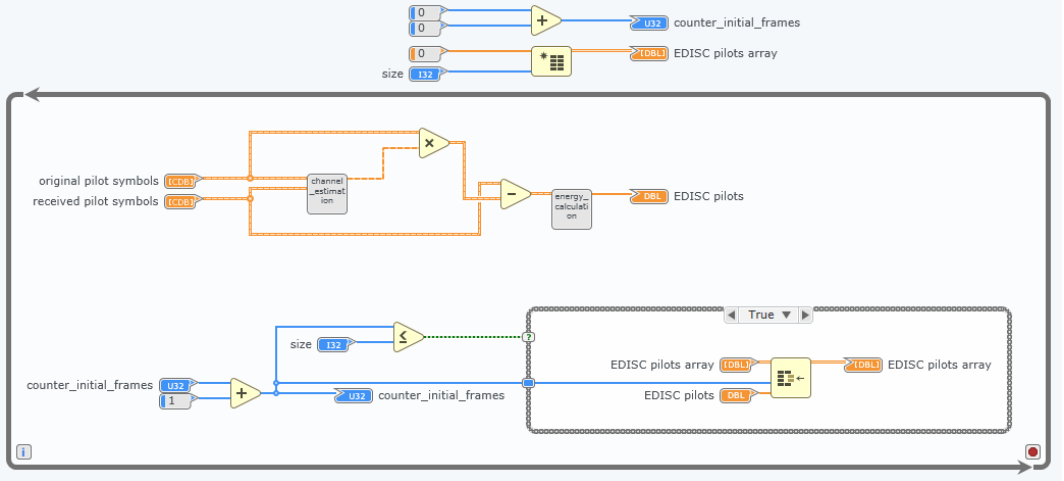

FIGURE 5.26: We devote a number of frames, where in each of them we calculate the energy of the remaining signal after the pilot cancellation and save it in an array in LabVIEW.

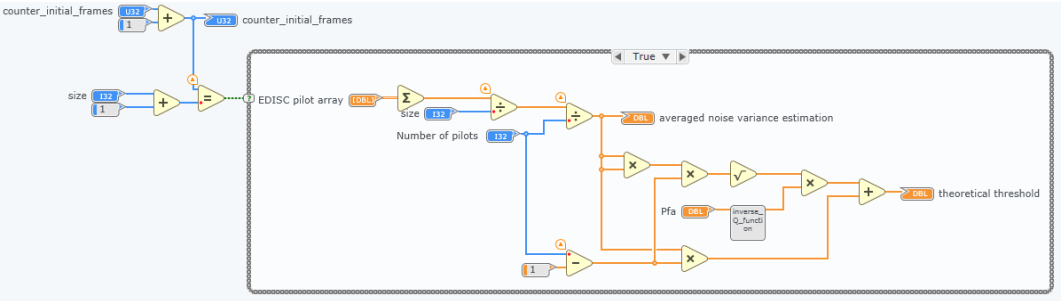

FIGURE 5.27: Averaged noise variance estimation and theoretical threshold calculation in LabVIEW.

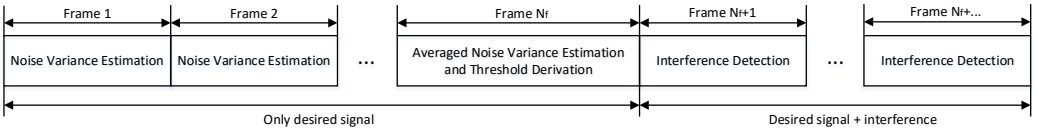

FIGURE 5.28: Frame structure for the noise variance estimation.

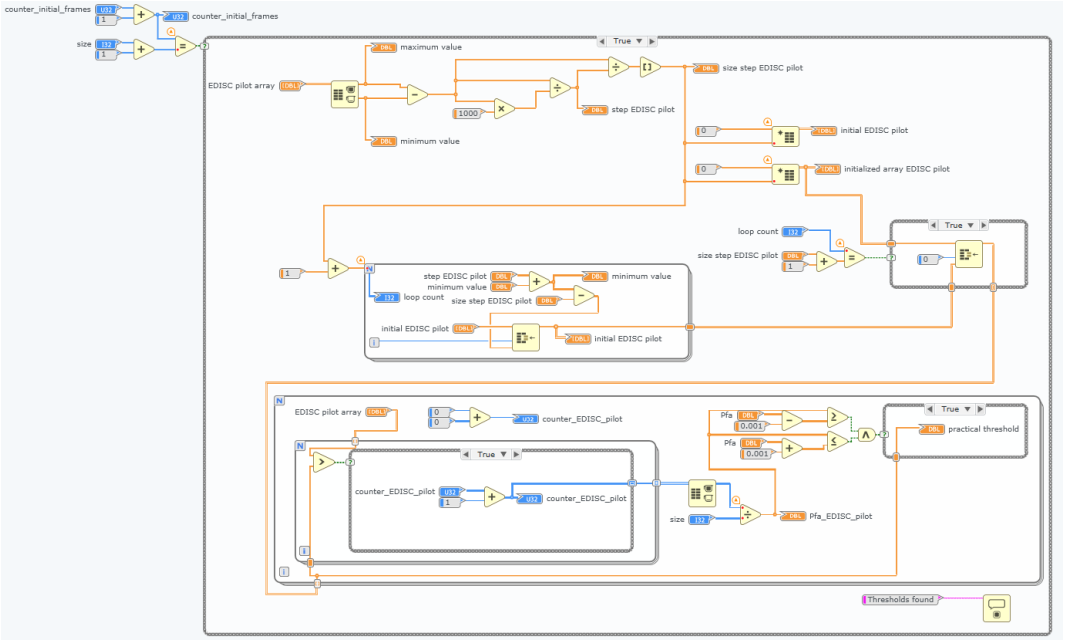

FIGURE 5.29: Derivation of the practical threshold in LabVIEW by applying line search, which selects the threshold which satisfies a given P_{FA_p}.

The maximum likelihood estimate (MLE) of σ_w^2 under $\mathcal{H}'_{0_p}$ minimizes (5.6) and is given by

$$\hat{\sigma}_w^2 = \frac{1}{N_p} \sum_{n=1}^{N_p} \left| y'_p(n) \right|^2. \tag{5.7}$$

Therefore, from (5.7) we can see that the estimation of the noise variance is obtained by taking the summation of N_p squared samples (remaining samples after the signal cancellation) and then dividing by the number N_p. However, in our lab set-up the noise variance changes over the time, and hence in order to achieve a more reliable estimation of the noise variance, we devote a number of frames N_f only for this purpose. Namely, we estimate the noise variance in each frame and when the devoted period expires, we derive the averaged estimated noise variance. Then, the latter and (5.3) are utilized for the derivation of the decision threshold. This methodology is obtained in LabVIEW as shown in Figures 5.26, 5.27. In the next frames, the TX2 port of Figure 5.21 starts to transmit an interfering signal and then, we apply the EDISC exploiting the pilots and use this derived threshold to detect the presence or absence of interference. The whole process of the frame structure is presented in Figure 5.28 .

Implementation for the derivation of the decision threshold based on a more practical approach

Here, we derive the decision threshold based on a practical approach. This method can be used in the case that the theoretical expression for the derivation of the decision threshold is unknown.

In this method, same as before, we devote a number of frames N_f only for the derivation of the decision threshold. In each frame, we calculate the energy of the remaining samples after the signal cancellation and save it in a buffer. At the end of the devoted period, we find the maximum and minimum value in the buffer and we apply line search in order to determine the threshold γ_p, which guarantees a given P_{FA_p}. This methodology is implemented in LabVIEW as shown in Figures 5.26, 5.29.

Probability of false alarm in real time

After the derivation of the decision threshold, we can calculate the probability of false alarm in real time. In each frame where the energy of the remaining signal after the pilots cancellation is higher than the decision threshold, we increase an initialized to zero counter by one and then, we divide the new result by the current number of frame. Therefore, in each frame we update the probability of false alarm and provide a visualization of it in real time. This methodology is implemented in LabVIEW as shown in Figure 5.30.

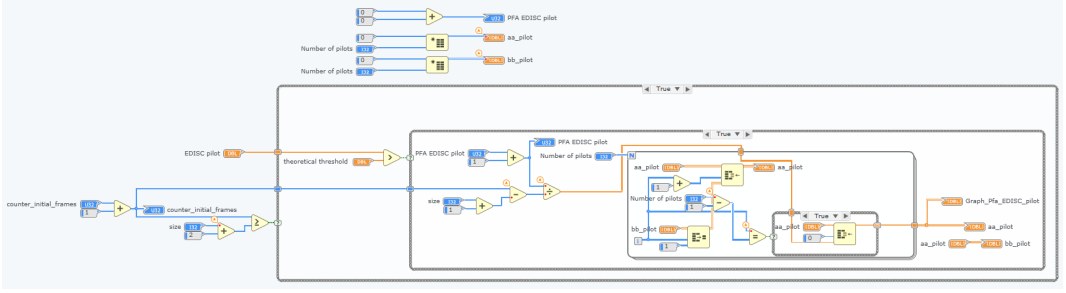

FIGURE 5.30: Calculation and visualization of the probability of false alarm in real time.

5.3.1.2 Probability of false alarm for the EDISC taking into account the decoding errors

In this algorithm, we estimate the channel by using again the pilot symbols, then we decode the received signal and we remove the decoded signal from the total received

signal. Finally, we apply an ED in the remaining signal. This methodology is described in the block diagram of Figure 5.31. In this algorithm, we calculate the probability

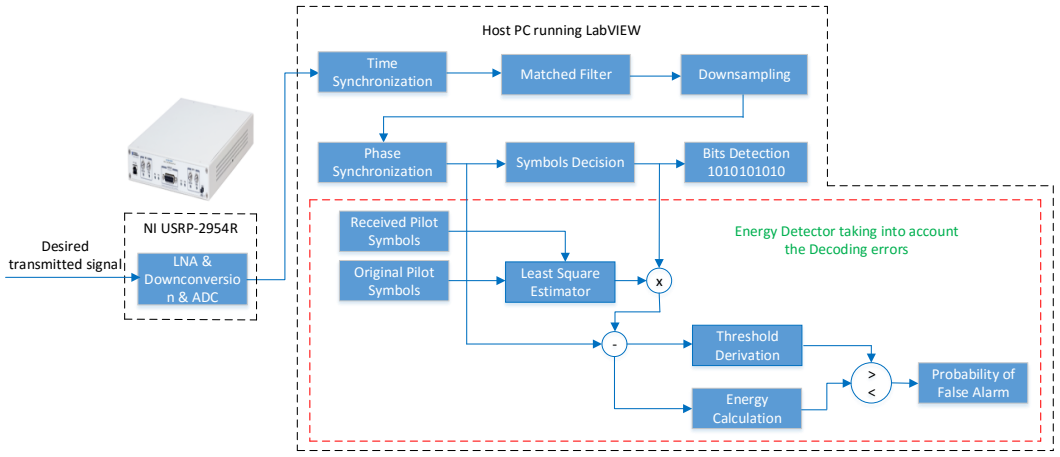

FIGURE 5.31: Flowchart showing the methodology for the calculation of the probability of false alarm of the EDISC with decoding errors.

of false alarm and derive the threshold based on the practical approach that described earlier. Therefore, the implementation in LabVIEW is similar as before, and the only part that needs an explanation is how we demodulate the QPSK signal in LabVIEW, which is shown in Figure 5.32.

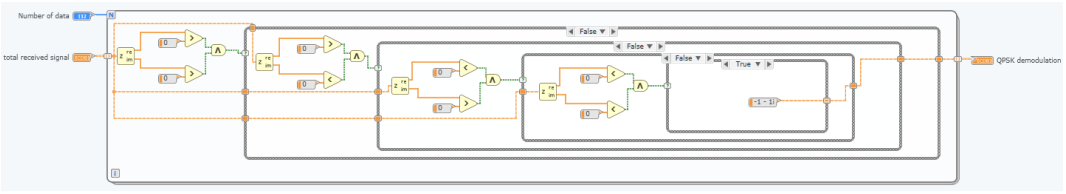

FIGURE 5.32: QPSK demodulation in LabVIEW.

5.3.1.3 Probability of false alarm for the CED

In this algorithm, there is no need for signal cancellation, therefore we determine the threshold immediately after the time synchronization (there is need to know the beginning of the frame). Then, we apply an ED in the total received signal. This methodology is described in the block diagram of Figure 5.33. In this algorithm, we calculate the probability of false alarm, derive the threshold based on the methodology of the practical approach and implemented them in LabVIEW as before.

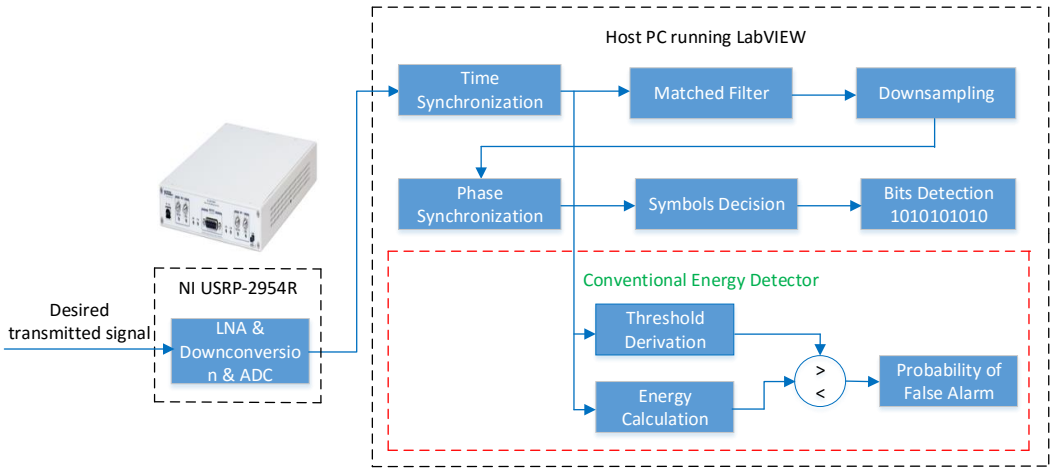

FIGURE 5.33: Flowchart showing the methodology for the calculation of the probability of false alarm of the CED.

5.3.2 Generation of interference and implementation for the calculation of the probability of detection in real time

After the derivation of the decision threshold, the TX2 port of Figure 5.21 starts to generate interference. The block diagram of this experimental set-up for the EDISC exploiting the pilot symbols is presented in 5.34.

In this thesis, we assume that the interference follows a Gaussian distribution and as mentioned in Section 4.2, this adopted model can be considered as a valid one. It can be the aggregated signal of several VSAT terminals and also, because the modulation and symbols of the interference are unknown, it is customary in the literature to assume this type of interference modeling.

5.3.2.1 Generating Gaussian interference

Producing a Gaussian interference is a simple task by using the LabVIEW function "Gaussian White Noise". This function takes two inputs: 1) the number of samples; and 2) the standard deviation and then, it generates white Gaussian noise. Since the standard deviation is the square root of the signal power, we divide by $\sqrt{2}$. Then, the interfering signal is prepared in order to pass to the transmitted device. This process is depicted in Figure 5.35.

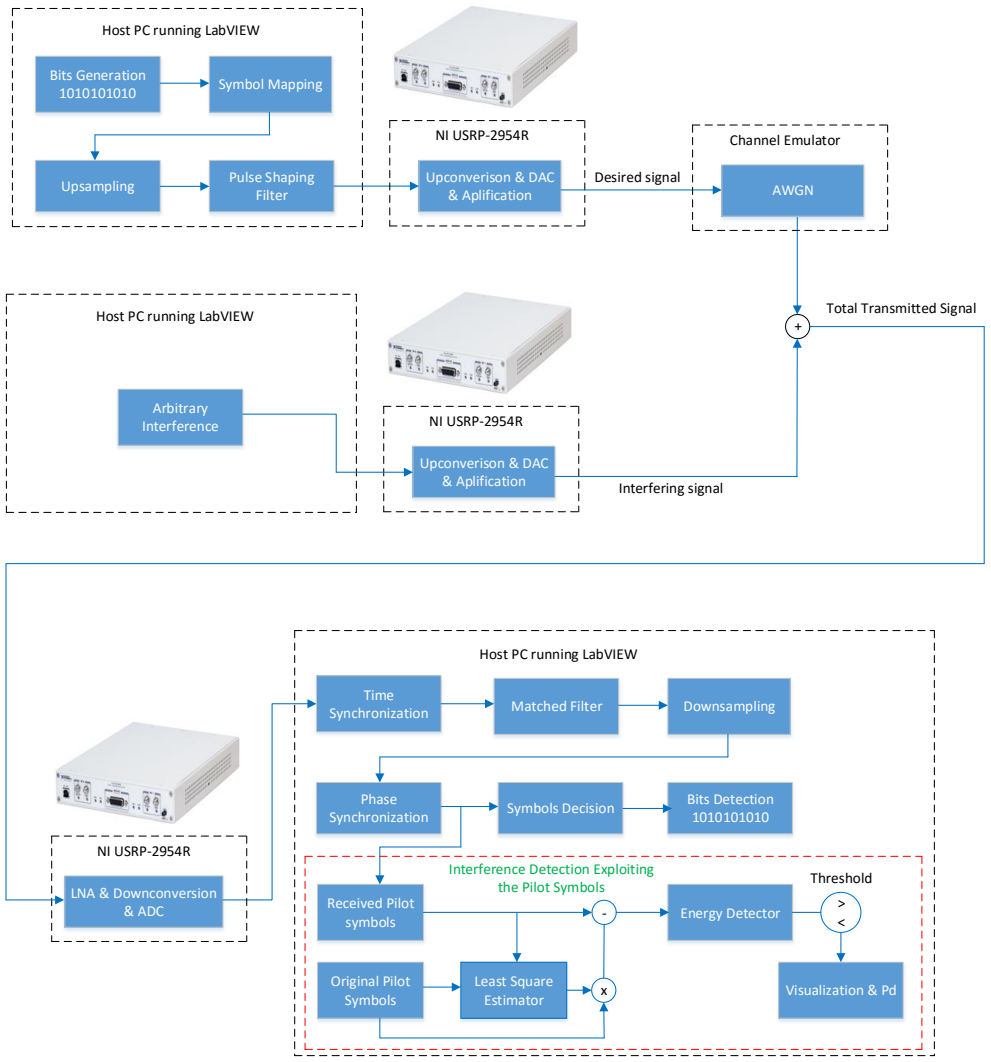

FIGURE 5.34: Flowchart of the complete interference detection system.

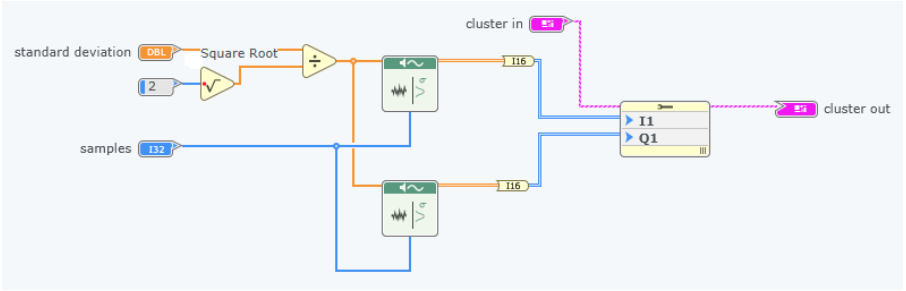

FIGURE 5.35: Generation of Gaussian interference, ready to pass to the transmitted device.

5.3.2.2 Probability of detection in real time

As mentioned earlier, after the derivation of the decision threshold, we assume the experimental set-up of Figure 5.21, where the TX2 port transmits interference which is

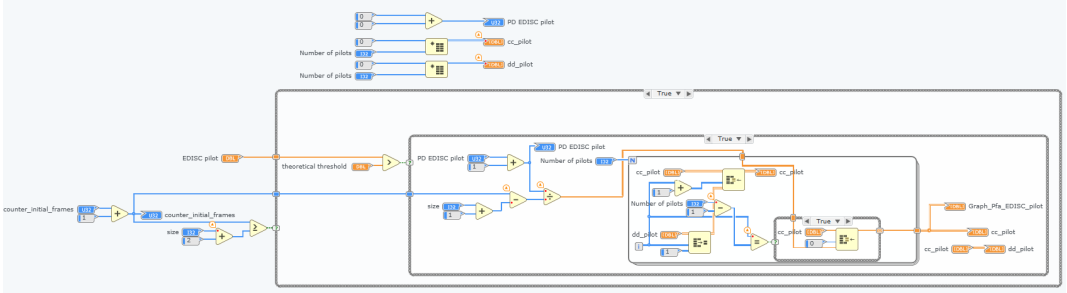

FIGURE 5.36: Calculation and visualization of the probability of detection in real time.

added to desired signal generated by the TX1 port. Then, we can apply the three aforementioned algorithms and the calculation of the P_D in real time is obtained following the same methodology as for the case of the P_FA.

In the beginning we focus on the EDISC exploiting the pilot symbols. Then, in each frame where the energy of the remaining signal after the pilots cancellation is higher than the decision threshold, we increase an initialized to zero counter by one and then, we divide the new result by the current number of frame. Therefore, in each frame we update the probability of detection and provide a visualization of it in real time. This methodology is implemented in LabVIEW as shown in Figure 5.36. Similar methodology and implementation performed for the EDISC with decoding errors and the CED.

5.4 Results

In this part, we present experimental results in order to 1) verify that the theoretical and practical approaches for the derivation of the decision threshold can guarantee $P_{FA} = 0.1$; 2) depict the probabilities of false alarm and detection in real time; and 3) present the detection or not of interference through squared light emitting diodes (LEDs).

As mentioned earlier, the TX1 port of Figure 5.21 generates the desired transmitted signal, which is QPSK modulated. In order to set a specific SNR, the desired signal is sent to the channel emulator, which injects on it artificial AWGN noise. This SNR is set to 8 dB. Then, the TX2 port of Figure 5.21 generates Gaussian interference and these signals are added in their analog waveforms and sent to RX port of Figure 5.21 for further processing. For the evaluation of the algorithms, the number of pilots is set to $N_p = 200$, while the number of data symbols $N_d = 200$. Here, we have to mention that the EDISC exploiting the pilots uses N_p samples, while the EDISC with decoding errors and the CED use $N_p + N_d$ samples. Furthermore, the probability of false alarm is set to $P_{FA} = 0.1$.

5.4.1 Evaluation of the decision threshold and performance analysis with respect to P_{FA} and P_d

Figure 5.37 presents the first panel for the evaluation of the probabilities of false alarm and detection of the aforementioned algorithms. Our first step is to run the program and then, we devote a number of frames, in this case $N_f = 6102$, in order to estimate the averaged noise variance and derive the decision threshold of the detectors. For the EDISC exploiting the pilots we derive the threshold based on both the theoretical and practical method. However, for the EDISC taking into account the decoding errors and the CED we implement only the practical approach which is more accurate. As we see, in Figure 5.38, when $N_f = 6102$ the thresholds have been found. Furthermore, it is observed that the derived theoretical threshold is very close to the derived threshold with the practical approach. After the derivation of the thresholds, we devote again a new number of frames in order to calculate the probability of false alarm in real time. Figure 5.39 shows that the derived thresholds can guarantee $P_{FA} = 0.1$. Obtaining this goal, we verify the reliability of the methods for the derivation of the decision thresholds. Finally, we see that the theoretical formula for the P_{FA} of the EDISC exploiting the pilots can be applied in a practical system offering a reliable decision threshold.

After the calculation of the probability of false alarm, we continue with the calculation of the probability of detection. In this step, we start to introduce interference by increasing the standard deviation of interference from the horizontal slider and observing the effects in the Figures of the probability of detection and interference-to-noise ratio (INR). From Figure 5.40 is observed that the EDISC with pilots or decoding errors obtains much more

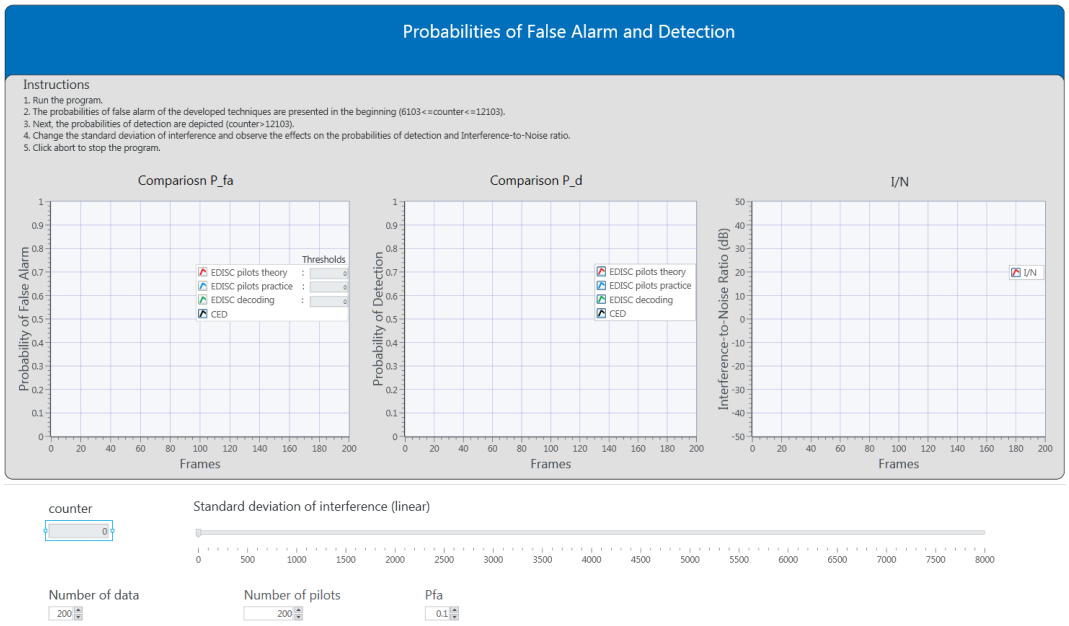

FIGURE 5.37: Panel for the visualization of the probabilities of false alarm and detection in real time.

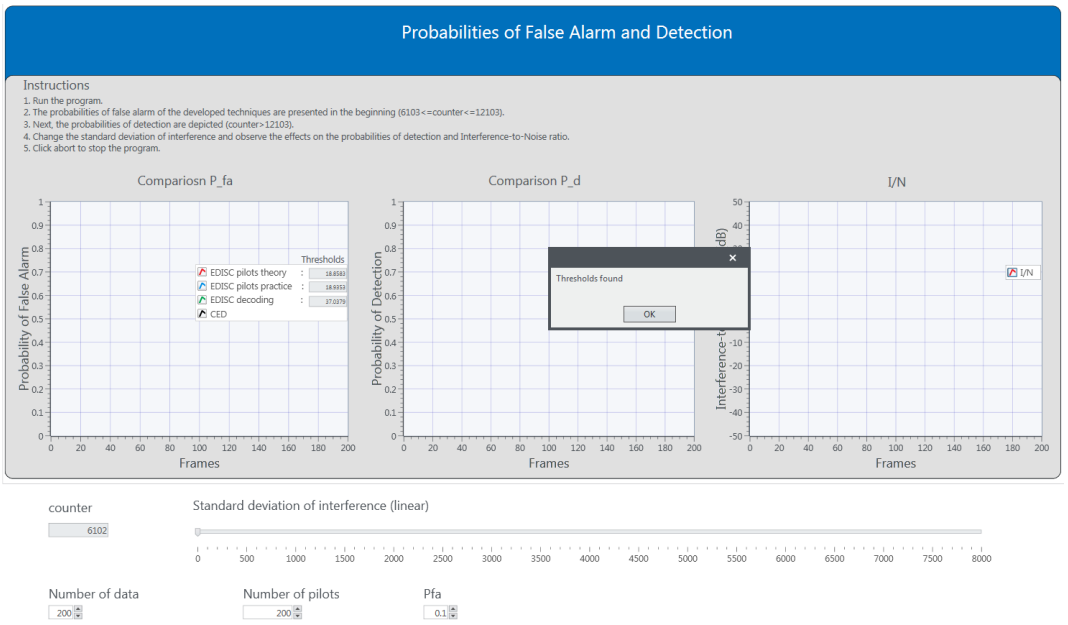

FIGURE 5.38: Thresholds found.

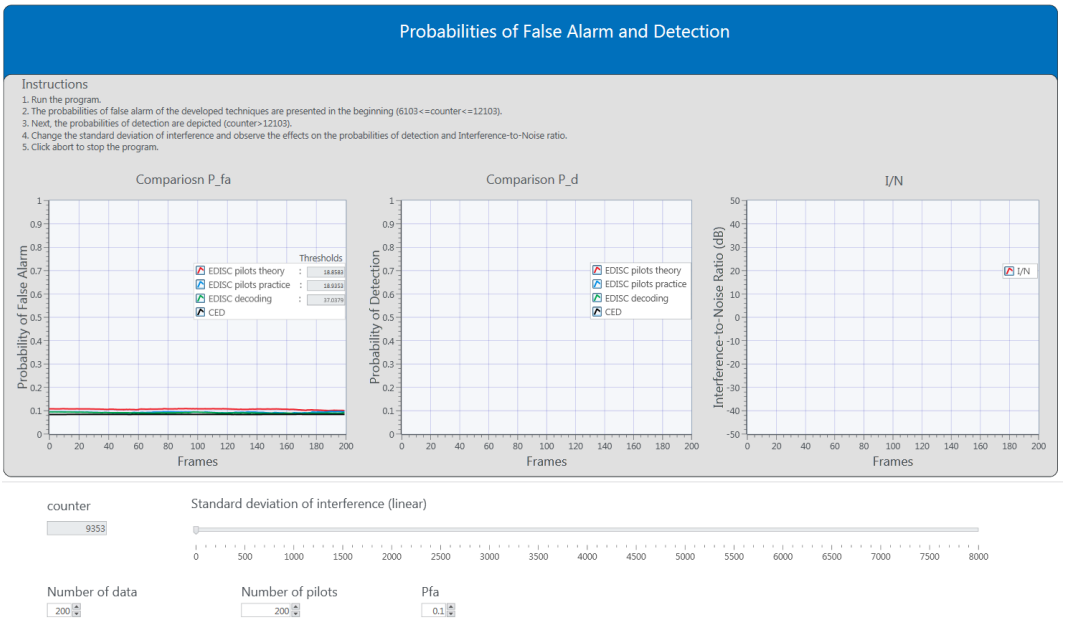

FIGURE 5.39: Visualization of the probability of false alarm of EDISC with pilots, EDISC with decoding errors and CED for $SNR \approx 8$ dB

reliable interference detection performance than the CED, particularly for low values of interference $INR \approx -10$ dB. Furthermore, we can notice that the EDISC with decoding errors performs better than the EDISC with pilots. It is explained by the fact that the EDISC with decoding errors has the ability to use the total number of symbols, while the EDISC with pilots is limited only on the number of pilots. Moreover, in Figure 5.41 we can see that the EDISC with pilots or decoding errors obtain $P_d \approx 1$ for $INR \approx -8$

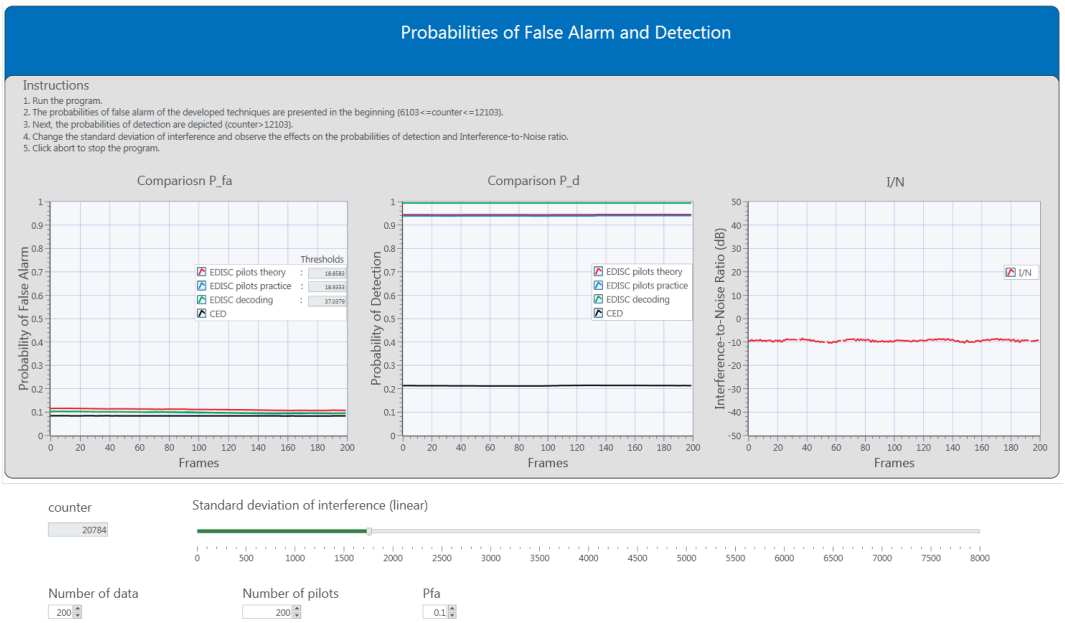

FIGURE 5.40: Visualization of the probability of detection of EDISC with pilots, EDISC with decoding errors and CED for $INR \approx -10$ dB.

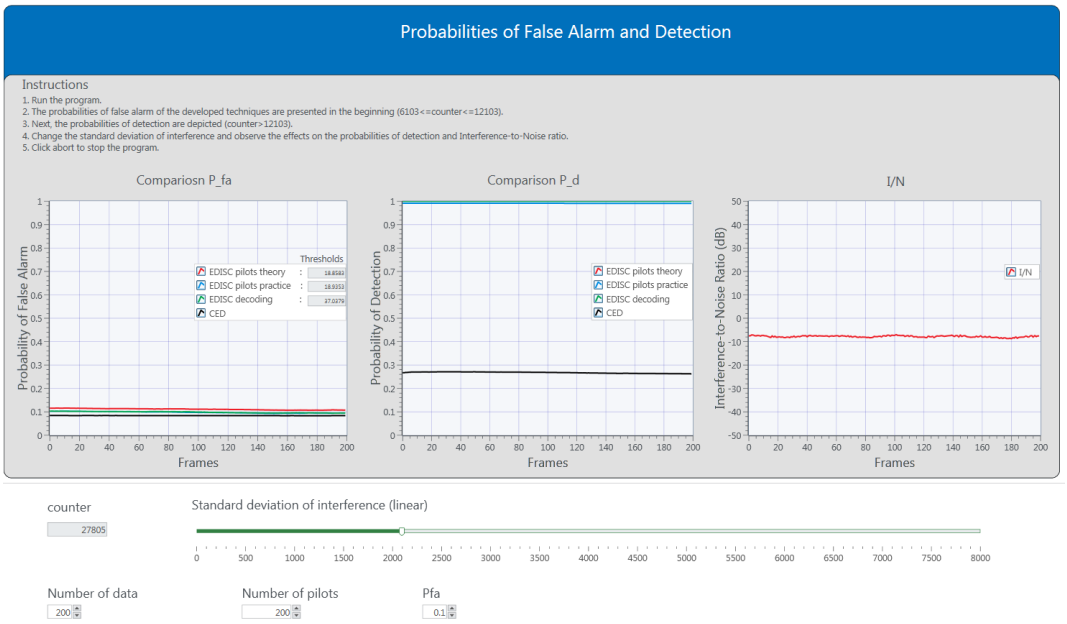

FIGURE 5.41: Visualization of the probability of detection of EDISC with pilots, EDISC with decoding errors and CED for $INR \approx -8$ dB.

dB, while the CED under the same scenario achieves $P_d \approx 0.27$. Finally, Figure 5.42 presents that the CED succeeds to obtain $P_d \approx 1$ when the $INR \approx 0$ dB. Therefore, it is obvious that our proposed algorithms can detect around 8 to 10 dB lower values of interference compared to CED.

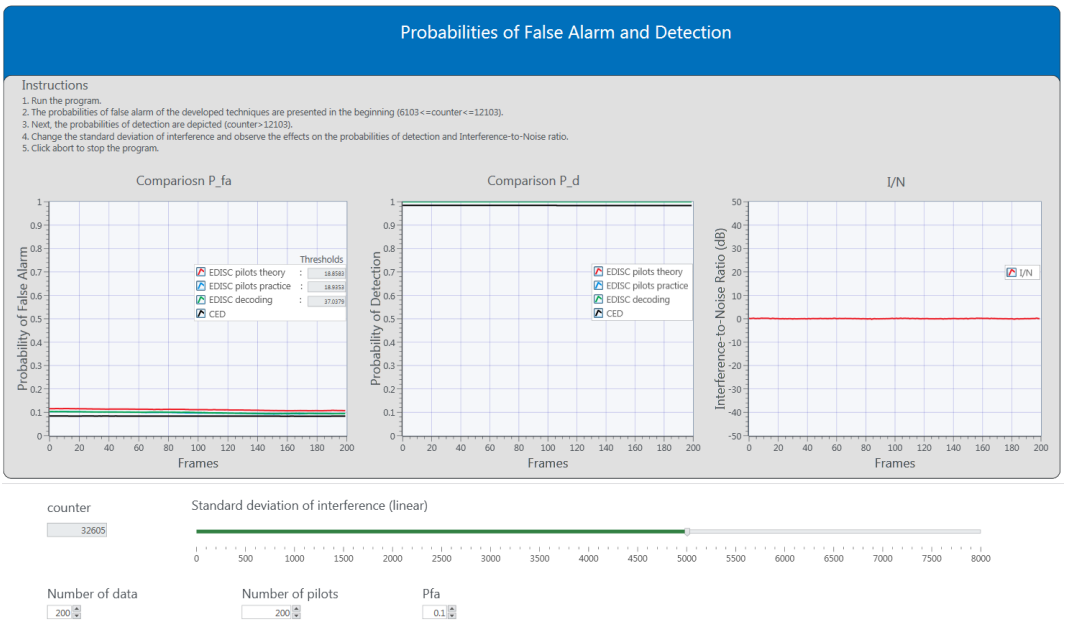

FIGURE 5.42: Thresholds found.

5.4.2 Visualization panel for the hypothesis testing

Figure 5.43 presents the second panel for the detection of interference. Except the probability of detection, another way to depict the detection of interference in real time is through a flush in squared LEDs. As shown in this figure, there are two LEDs which represent the case that the detection or not of interference is obtained using the CED and EDISC with the pilots. Both LEDs are white in the beginning. The white color corresponds in the absence of interference. In each frame the detectors try to detect the presence or not of the interference and if the interference is present the LEDs flush or change color and from white they become red. Therefore, the red color corresponds to presence of interference. Now, in the case where the interference is absent, the LEDs return to or keep the white color.

Figure 5.44 illustrates that when we change the standard deviation of interference from the horizontal slider and introduce strong interference, namely $INR \approx 0$ dB, both LEDs are red. However, if we reduce the level of the interference to $INR \approx -8$ dB, it is observed that the LED of the CED is most of the time white, while the LED of the EDISC with pilots is still red, as shown in Figure 5.45. Therefore, also from this panel with the flush of the LEDs, we can notice that the EDISC with pilots performs much better than the CED, especially for the detection of weak interference.

Finally, in this panel, we see that there is a graph which presents the estimated received signal-to-noise ratio, which is for the whole duration of the program 8 dB.

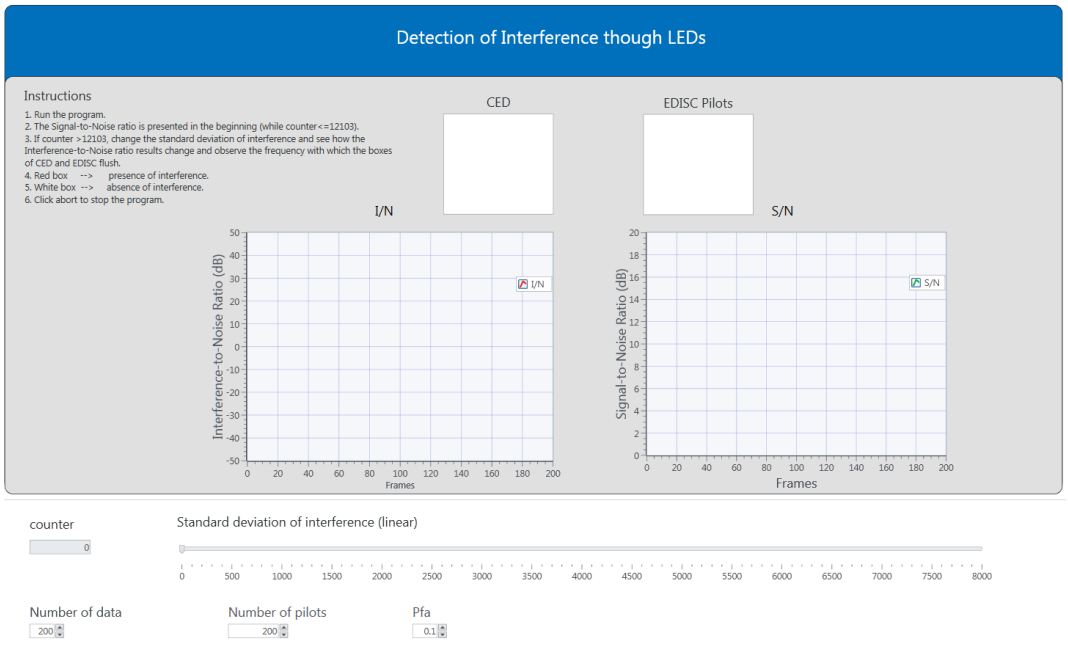

FIGURE 5.43: Interference detection through squared LEDs.

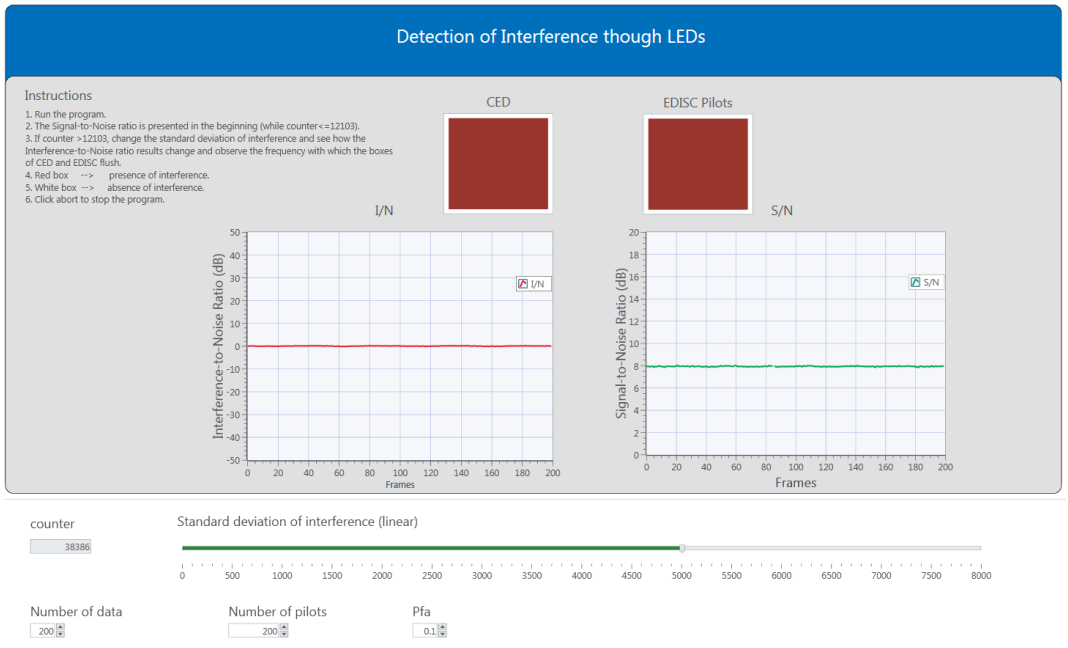

FIGURE 5.44: Interference detection through squared LEDs for $INR \approx 0$ dB.

5.5 Summary

In this chapter, a realistic communication system for the detection of interference using software defined radios, particularly USRPs, was built. We programmed the USRPs using the LabVIEW Communications System Design Suite 2.0. software tool of National Instruments and we explained with details how we implemented each piece of

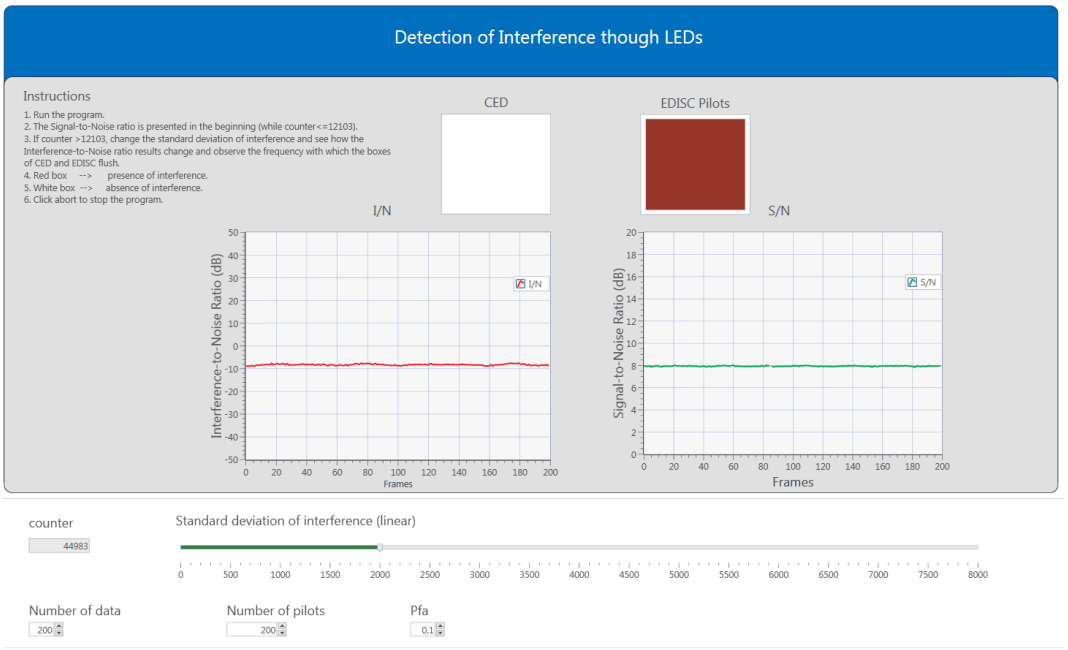

FIGURE 5.45: Interference detection through squared LEDs for $INR \approx -8$ dB.

this detection system. A little more attention was given in the implementation of the decision threshold, which is the most critical part in the design of a detector. Then, the developed algorithms for the detection of interference were evaluated and compared with the conventional energy detector. Finally, two panels were demonstrated. The first one presented in real time the probabilities of false alarm and detection in relation to the interference-to-noise ratio and the second panel showed how the interference can be detected through squared LEDs, again in relation to interference-to-noise ratio. Finally, both panels showed that the proposed and developed detectors perform significantly better than the CED in the detection of weak interference, offering the capability of detecting 8 to 10 dB lower values of interference.

Chapter 6

Conclusions and Open Issues

6.1 Conclusions

In this thesis, the idea of spectrum monitoring in wireless and satellite communications was investigated, focusing on two main applications: 1) spectrum monitoring in a cognitive radio system in order to allow the more efficient use of the radio frequency spectrum; and 2) spectrum monitoring in satellite communications for interference detection.

In the first part, an algorithm for simultaneous spectrum sensing and data transmission through the collaboration of the secondary transmitter with the secondary receiver was provided. That algorithm considered energy detector with imperfect signal cancellation taking into account the decoding errors. Then, the closed-form expressions for the probability of false alarm were derived assuming digitally modulated signals (i.e. BPSK, QPSK, M-QAM) in contrast to the widely used Gaussian signaling in the literature. Performance analysis of the developed algorithm was carried out, which showed that the detection performance of the proposed scheme obtained significantly better performance than the conventional energy detector.

In the second part, the detection of interference on-board the satellite was discussed. The introduction of a spectrum monitoring unit within the satellite transponder will bring many benefits compared to the ground based solutions such the avoidance of replication of monitoring equipments in multi-beam systems. Then, two algorithms for the detection of interference on-board the satellite were proposed. Both algorithms were based on the energy detector with imperfect signal cancellation exploiting the pilot or data symbols of the standards and taking into account the channel estimation error. The theoretical expressions for the probabilities of false alarm and detection and the simulation results showed that both proposed detection schemes perform better than

the conventional energy detector. Finally, it was shown that the two-stage detector can achieve better performance than the detectors based on the pilots or data but we have to pay the cost of increased computational complexity.

Finally, this thesis went one step further evaluating the proposed algorithms for the detection of interference experimentally using USRPs, programmed by LabVIEW. Two panels were demonstrated, where the first one presented the probabilities of false alarm and detection in real time, while the second panel showed how the detection of interference is obtained through squared LEDs. This work validated the accuracy of the theoretical and numerical analysis of this thesis.

6.2 Open Issues

In the following subsections, we present open research problems related to the topics discussed in this thesis.

6.2.1 Cognitive Radio

Consideration of M-PSK Modulation and Channel Estimation Error

- This thesis derived the closed-form expressions for the probabilities of false alarm and detection for M-QAM modulated signals. Therefore, a further analysis should also include other modulation schemes such as M-PSK in order to provide a full coverage of all possible scenarios. Furthermore, this thesis considered that the channel is known. However, in reality, the channel should be estimated. Hence, the channel estimation error is an important factor which has to be taken into account in the analysis, constituting a valuable idea for future studies in order to see how this uncertainty affects the sensing performance of the proposed detectors.

Consideration of non-Gaussian Primary Signal

- This thesis assumed that the primary signal or the interference follow a Gaussian distribution. This model could be considered as a valid one for the performance evaluation of the developed detectors. However, a valuable suggestion should be to derive the probability of detection of the proposed detectors for the case that the primary signal has distribution different from Gaussian and evaluate the affects (if any) in the sensing performance.

Dynamic Traffic Pattern

- Another idea that could be considered as future work is the adaptation of the proposed scheme in a more dynamic traffic pattern, where we divide the PU traffic into slots in accordance with SU's sensing process, and then, we derive the probability that PU changes its state in a stochastic slot.

6.2.2 Interference Detection

Synchronization errors

- This thesis considered that the synchronization is perfect in order to extract perfectly the received samples related to position of the pilot symbols. Therefore, a valuable idea for further studies is the consideration of synchronization errors and evaluation how this uncertainty will affect the sensing performance of the proposed detectors.

Multiple Antennas

- This thesis studied single input - single output systems, hence the derivation of the analytical expression for the probabilities of false alarm and detection in a multiple antennas scenario is considered as good suggestion. Furthermore, we showed that the proposed detector obtains better detection performance than the conventional energy detector, however, the issue of noise variance uncertainty still remains. The evaluation of the combination of signal cancellation with other detection schemes such as eigenvalue detectors, more robust on the noise variance uncertainty should be considered.

6.2.3 Lab

DVB-S2 signal, Digitally Modulated Interference and Rain Attenuation

- This thesis considered a simple QPSK signal and a multi-tone preamble for the lab demonstration. However, a more realistic signal for satellite scenarios should be considered e.g. desired signal with DVB-S2 structure. Furthermore, the effects of a digitally modulated interference should be evaluated and as well as the rain attenuation in the satellite channel should be modeled and taken into account.

Oversampling Effect and Quantization Error

- When we receive a signal, we will use an ADC sampling rate with certain resolution e.g. 16 bits. This will essentially define the dynamic range e.g. the ratio between the weakest and the strongest signal that can be reliably represented in the digital domain. However, may there is power imbalance between the commercial traffic and the interference. Both of them have to be comfortably included within this dynamic range. If not, we may have some problems: 1) commercial traffic too close to the upper bound of the dynamic range which means that you will have clipping and that you will not be able to reliably remove it; and 2) interference too close to the lower bound which means that even with perfect signal cancellation, the interference signal will be affected by the quantization noise. This is a discrete noise much different than the Gaussian noise that we considered in this thesis, so it has not been taken into account in our analysis and it might have serious implication in the sensing process.

  Furthermore, the demonstration of our proposed detectors in the lab took place in the baseband domain. A valuable idea could be the use of these detectors on the samples in the oversampling domain and then the evaluation of its effects in the sensing performance.

Appendix A

Derivation of the mean $\mu_{\mathcal{H}_{00_B}}$

The derivation of the mean $\mu_{\mathcal{H}_{00_B}}$ is based on the law of the total expectation [114], because it is related to the mean given that the transmitted symbol is $s[n] = \sqrt{P_s}$ and the mean given that the transmitted symbol is $s[n] = -\sqrt{P_s}$, which can be written as follows:

$$
\begin{aligned}
&E\left\{\|\mathbf{y}\|^2|\mathcal{H}_{00_B}\right\} = E\left\{\sum_{n=0}^{N-1}|y\,[n]|^2|\mathcal{H}_{00_B}\right\} = \sum_{n=0}^{N-1}E\left\{|y\,[n]|^2|\mathcal{H}_{00_B}\right\} \\
&= \sum_{n=0}^{N-1}E\left\{|y\,[n]|^2\,\middle|s\,[n] = +\sqrt{P_s}\;,\;\hat{s}\,[n] = +\sqrt{P_s}\right\}P\left(s\,[n] = +\sqrt{P_s}\right)P\left(\hat{s}\,[n] = +\sqrt{P_s}\,|c_B\right) \\
&+ \sum_{n=0}^{N-1}E\left\{|y\,[n]|^2\;\middle|s\,[n] = -\sqrt{P_s}, \hat{s}\,[n] = -\sqrt{P_s}\right\}P\left(s\,[n] = -\sqrt{P_s}\right)P\left(\hat{s}\,[n] = -\sqrt{P_s}\,|c_B\right).
\end{aligned}
\tag{A.1}
$$

However, we assume that these symbols are transmitted equiprobably, hence, $P(s\,[n] = \sqrt{P_s}) = P\left(s\,[n] = -\sqrt{P_s}\right) = 1/2$. Furthermore, as was mentioned in Section 3.3, the received signal can be decoded correct under the following two cases: 1) when $w[n] \geq -\sqrt{P_t}$ given that the transmitted symbol is $s[n] = \sqrt{P_s}$; or 2) when $w[n] \leq \sqrt{P_t}$ given that the transmitted symbol is $s[n] = -\sqrt{P_s}$. Therefore, the expression of (A.1) can be further extended as follows:

$$
\begin{aligned}
E\left\{\|\mathbf{y}\|^2|H_{\,00}\right\} &= \frac{1}{2}\sum_{n=0}^{N-1}E\left\{|y\,[n]|^2\,|w\,[n]\;\geq -\sqrt{P_t}\right\}P\left(w\,[n] \geq -\sqrt{P_t}\,|c_B\right) \\
&+ \frac{1}{2}\sum_{n=0}^{N-1}E\left\{|y\,[n]|^2\,|w\,[n]\;\leq +\sqrt{P_t}\right\}P\left(w\,[n] \leq +\sqrt{P_t}\,|c_B\right).
\end{aligned}
\tag{A.2}
$$

But, as was mentioned again in Section 3.3, the remaining noise under $\mathcal{H}_{00_B}$ does not follow any more a normal distribution, but a truncated normal distribution in the following intervals: 1) $w[n] \leq -\sqrt{P_t}$; 2) $-\sqrt{P_t} \leq w[n] \leq \sqrt{P_t}$; and 3) $w[n] \geq \sqrt{P_t}$. Thus,

(A.2) can be further written as follows:

$$
\begin{aligned}
E\left\{\|\mathbf{y}\|^2|H_{00_B}\right\} &= \frac{1}{2}\sum_{n=0}^{N-1} E\left\{|y[n]|^2 \left|-\sqrt{P_t} \le w[n] \le \sqrt{P_t}\right.\right\} P\left(-\sqrt{P_t} \le w[n] \le \sqrt{P_t}\,|c_B\right) \\
&+ \frac{1}{2}\sum_{n=0}^{N-1} E\left\{|y[n]|^2 |w[n] \ge \sqrt{P_t}\right\} P\left(w[n] \ge \sqrt{P_t}\,|c_B\right) \\
&+ \frac{1}{2}\sum_{n=0}^{N-1} E\left\{|y[n]|^2 \left|-\sqrt{P_t} \le w[n] \le \sqrt{P_t}\right.\right\} P\left(-\sqrt{P_t} \le w[n] \le \sqrt{P_t}\,|c_B\right) \\
&+ \frac{1}{2}\sum_{n=0}^{N-1} E\left\{|y[n]|^2 |w[n] \le -\sqrt{P_t}\right\} P\left(w[n] \le -\sqrt{P_t}\,|c_B\right). \qquad \text{(A.3)}
\end{aligned}
$$

However, because of symmetry, the above expression can be simplified into the following one:

$$
\begin{aligned}
E\left\{\|\mathbf{y}\|^2|H_{00_B}\right\} &= \sum_{n=0}^{N-1} E\left\{|y[n]|^2 \left|-\sqrt{P_t} \le w[n] \le \sqrt{P_t}\right.\right\} P\left(-\sqrt{P_t} \le w[n] \le \sqrt{P_t}\,|c_B\right) \\
&+ \sum_{n=0}^{N-1} E\left\{|y[n]|^2 |w[n] \ge \sqrt{P_t}\right\} P\left(w[n] \ge +\sqrt{P_t}\,|c_B\right), \qquad \text{(A.4)}
\end{aligned}
$$

where according to Baye's Theorem [115]

$$
P\left(-\sqrt{P_t} \le w[n] \le \sqrt{P_t} \le \sqrt{P_t}\,|c_B\right) = \frac{P\left(-\sqrt{P_t} \le w[n] \le \sqrt{P_t}\right)}{P_{c_B}} \qquad \text{(A.5)}
$$

and

$$
P\left(w[n] \ge +\sqrt{P_t}\,|c_B\right) = \frac{P\left(w[n] \ge \sqrt{P_t}\right)}{P_{c_B}}. \qquad \text{(A.6)}
$$

Then, we are interested in finding the interval of $|w[n]|^2$, thus, (A.4) is also written as follows:

$$
\begin{aligned}
\mu_{\mathcal{H}_{00_B}} = E\left\{\|\mathbf{y}\|^2 |H_{00_B}\right\} &= \sum_{n=0}^{N-1} E\left\{|w[n]|^2 \left|0 \le |w[n]|^2 \le P_t\right.\right\} \frac{P\left(-\sqrt{P_t} \le w[n] \le \sqrt{P_t}\right)}{P_{c_B}} \\
&+ \sum_{n=0}^{N-1} E\left\{|w[n]|^2 \left||w[n]|^2 \ge P_t\right.\right\} \frac{P\left(w[n] \ge \sqrt{P_t}\right)}{P_{c_B}}, \qquad \text{(A.7)}
\end{aligned}
$$

Finally, according to Lemma 3.1, (A.7) takes its final shape which is given by (3.24).

Appendix B

Derivation of the variance $V_{\mathcal{H}_{00_B}}$

The derivation of the variance $V_{\mathcal{H}_{00_B}}$ is based on the law of the total variance [114] and Baye's Theorem, because it is related to the variance given that the transmitted symbol is $s[n] = \sqrt{P_s}$ and the variance given that the transmitted symbol is $s[n] = -\sqrt{P_s}$, which can be written as follows:

$$
\begin{aligned}
&V\left\{\|\mathbf{y}\|^2 | H_{\,00_B}\right\} = V\left\{\sum_{n=0}^{N-1} |y\,[n]|^2 | H_{\,00_B}\right\} = \sum_{n=0}^{N-1} V\left\{|y\,[n]|^2 | H_{\,00_B}\right\} \\
&= \sum_{n=0}^{N-1} V\left\{|y\,[n]|^2 \left| s_{tr}^{+}\,,\; s_{est}^{+}\right.\right\} P\left(s_{est}^{+}\right) P\left(s_{est}^{+}\,|c_B\right) + V\left\{|y\,[n]|^2 \left| s_{tr}^{-}\,,\; s_{est}^{-}\right.\right\} P\left(s_{est}^{-}\right) P\left(s_{est}^{-}\,|c_B\right) \\
&+ \sum_{n=0}^{N-1} E\left\{|y\,[n]|^2 \;\left| s_{tr}^{+}, s_{est}^{+}\right.\right\}^2 \left(1 - P\left(s_{tr}^{+}\right) P\left(s_{est}^{+}\,|c_B\right)\right) P\left(s_{tr}^{+}\right) P\left(s_{est}^{+}\,|c_B\right) \\
&+ \sum_{n=0}^{N-1} E\left\{|y\,[n]|^2 \;\left| s_{tr}^{-}\,,\; s_{est}^{-}\right.\right\}^2 \left(1 - P\left(s_{est}^{-}\right) P\left(s_{est}^{-}\,|c_B\right)\right) P\left(s_{est}^{-}\right) P\left(s_{est}^{-}\,|c_B\right) \\
&- 2\sum_{n=0}^{N-1} E\left\{|y\,[n]|^2 \;\left| s_{tr}^{+}\,,\; s_{est}^{+}\right.\right\} P\left(s_{est}^{+}\right) P\left(s_{est}^{+}\,|c_B\right) E\left\{|y\,[n]|^2 \;\left| s_{tr}^{-}\,,\; s_{est}^{-}\right.\right\} P\left(s_{est}^{-}\right) P\left(s_{est}^{-}\,|c_B\right),
\end{aligned}
\tag{B.1}
$$

where $s_{tr}^{+} = \left(s\,[n] = +\sqrt{P_s}\right)$, $s_{est}^{+} = \left(\hat{s}\,[n] = +\sqrt{P_s}\right)$, $s_{tr}^{-} = \left(s\,[n] = -\sqrt{P_s}\right)$ and $s_{est}^{-} = \left(\hat{s}\,[n] = -\sqrt{P_s}\right)$. Then, following the same methodology as that for the derivation of the

mean $\mu_{\mathcal{H}_{00_B}}$ the expression of (B.1) is simplified to the following one:

$$
\begin{aligned}
V_{\mathcal{H}_{00_B}} &= V\left\{\|\mathbf{y}\|^2 |H_{00}\right\} = \sum_{n=0}^{N-1} V\left\{|w[n]|^2 \left| 0 \le |w[n]|^2 \le P_t \right.\right\} P_{w_n}^{\left[-\sqrt{P_t},\sqrt{P_t}\right]} + \sum_{n=0}^{N-1} V\left\{|w[n]|^2\right. \\
&\left. |w[n]|^2 \ge P_t\right\} P_{w_n}^{\left[\sqrt{P_t},\infty\right]} + \sum_{n=0}^{N-1} E\left\{|w[n]|^2 \left| 0 \le |w[n]|^2 \le P_t \right.\right\}^2 \left(1 - P_{w_n}^{\left[-\sqrt{P_t},\sqrt{P_t}\right]}\right) P_{w_n}^{\left[-\sqrt{P_t},\sqrt{P_t}\right]} \\
&+ \sum_{n=0}^{N-1} E\left\{|w[n]|^2 \left| |w[n]|^2 \ge P_t \right.\right\}^2 \left(1 - P_{w_n}^{\left[\sqrt{P_t},\infty\right]}\right) P_{w_n}^{\left[\sqrt{P_t},\infty\right]} \\
&- 2\sum_{n=0}^{N-1} E\left\{|w[n]|^2 \left| 0 \le |w[n]|^2 \le P_t \right.\right\} P_{w_n}^{\left[\sqrt{P_t},\infty\right]} E\left\{|w[n]|^2 \left| |w[n]|^2 \ge P_t \right.\right\} P_{w_n}^{\left[\sqrt{P_t},\infty\right]}. \qquad \text{(B.2)}
\end{aligned}
$$

Finally, according to Lemma 3.1 (B.2) takes its final shape which is given by (3.25).

Appendix C

Derivation of the mean $\mu_{\mathcal{H}_{00}{}_{M-Q}}$

The derivation of $\mu_{\mathcal{H}_{0,k=t,t=k}}$ under any M-QAM scenario is obtained considering the example of 64-QAM modulation. The constellation of 64-QAM is depicted in Figure C.1, where the red symbols represent the inner-constellation symbols, the black symbols represent the outer-constellation symbols, while the blue symbols correspond to the outermost-constellation symbols.

- For the inner-constellation symbols, the received signal is decoded correctly according to the following constraints C_1, C_2:

$$\begin{array}{ll} C_1: & -\sqrt{P_t} \leq \mathcal{R}\{w\} \leq \sqrt{P_t} \\ C_2: & -\sqrt{P_t} \leq \mathcal{I}\{w\} \leq \sqrt{P_t} \end{array}, \tag{C.1}$$

  with the probability of that to happen to be:

$$\begin{array}{c} P\left(-\sqrt{P_t} \leq \mathcal{R}\{w\} \leq +\sqrt{P_t}\right) = F_x\left(\sqrt{P_t}\right) - F_x\left(-\sqrt{P_t}\right) \\ \text{and} \\ P\left(-\sqrt{P_t} \leq \mathcal{I}\{w\} \leq +\sqrt{P_t}\right) = F_x\left(\sqrt{P_t}\right) - F_x\left(-\sqrt{P_t}\right) \end{array}. \tag{C.2}$$

- For the outer-constellation symbols, the received signal is decoded correctly according to the following constraints C_1, C_2:

$$\begin{array}{lll} C_1: & -\sqrt{P_t} \leq \mathcal{R}\{w\} \leq +\sqrt{P_t} & \text{horizontal up,} \\ C_2: & \mathcal{I}\{w\} \geq -\sqrt{P_t} & \\ C_1: & -\sqrt{P_t} \leq \mathcal{R}\{w\} \leq +\sqrt{P_t} & \text{horizontal down,} \\ C_2: & \mathcal{I}\{w\} \leq +\sqrt{P_t} & \end{array}$$

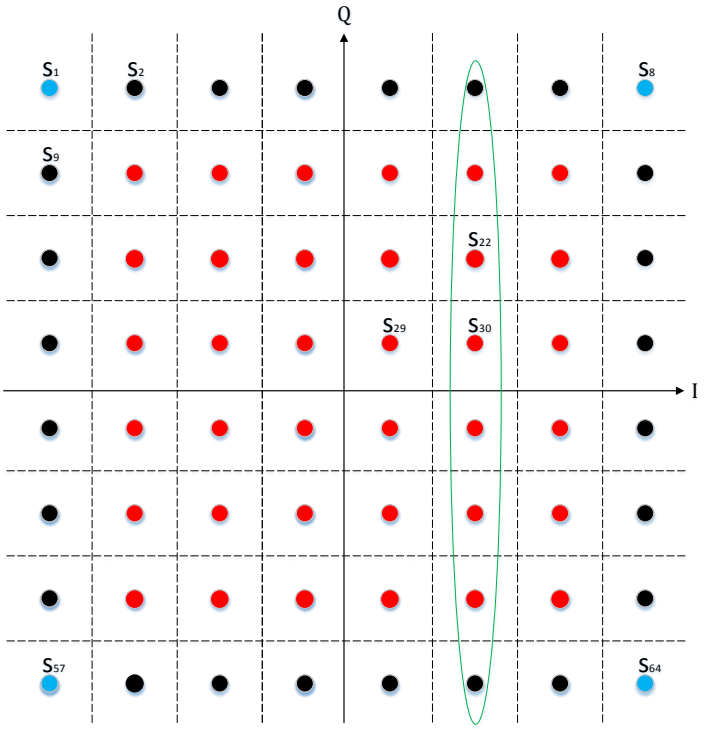

FIGURE C.1: Constellation for 64-QAM modulation.

$$\begin{aligned} C_1: &\quad \mathcal{R}\{w\} \geq -\sqrt{P_t} \\ C_2: &\quad -\sqrt{P_t} \leq \mathcal{I}\{w\} \leq +\sqrt{P_t} \end{aligned} \quad \text{vertical right,}$$

$$\begin{aligned} C_1: &\quad \mathcal{R}\{w\} \leq +\sqrt{P_t} \\ C_2: &\quad -\sqrt{P_t} \leq \mathcal{I}\{w\} < +\sqrt{P_t} \end{aligned} \quad \text{vertical left,} \tag{C.3}$$

with the probability of each sub-category to happen to be:

$$\begin{aligned} P\left(-\sqrt{P_t} \leq \mathcal{R}\{w\} \leq +\sqrt{P_t}\right) &= P\left(-\sqrt{P_t} \leq \mathcal{I}\{w\} \leq +\sqrt{P_t}\right) \\ &= F_x\left(\sqrt{P_t}\right) - F_x\left(-\sqrt{P_t}\right) \end{aligned} \tag{C.4}$$

and

$$\begin{aligned} P\left(\mathcal{R}\{w\} \leq +\sqrt{P_t}\right) = P\left(\mathcal{I}\{w\} \leq +\sqrt{P_t}\right) &= P\left(\mathcal{R}\{w\} \geq -\sqrt{P_t}\right) \\ = P\left(\mathcal{I}\{w\} \geq -\sqrt{P_t}\right) &= F_x\left(\sqrt{P_t}\right). \end{aligned} \tag{C.5}$$

Therefore, because the probability of each of the above sub-categories is equal, all these symbols are considered under the name of outer-constellation symbols.

- For the outermost-constellation symbols the received signal is decoded correctly according to the following constraints C_1, C_2:

$$\begin{array}{lll} C_1: & \mathcal{R}\{w\} \geq -\sqrt{P_t} & \text{right up,} \\ C_2: & \mathcal{I}\{w\} \geq -\sqrt{P_t} & \\ C_1: & \mathcal{R}\{w\} \geq -\sqrt{P_t} & \text{right down,} \\ C_2: & \mathcal{I}\{w\} \leq +\sqrt{P_t} & \\ C_1: & \mathcal{R}\{w\} \leq +\sqrt{P_t} & \text{left up,} \\ C_2: & \mathcal{I}\{w\} \geq -\sqrt{P_t} & \\ C_1: & \mathcal{R}\{w\} \leq +\sqrt{P_t} & \text{left down,} \\ C_2: & \mathcal{I}\{w\} \leq +\sqrt{P_t} & \end{array} \tag{C.6}$$

  with the probability of each sub-category to happen to be:

$$\begin{array}{c} P\left(\mathcal{R}\{w\} \geq -\sqrt{P_t}\right) = P\left(\mathcal{R}\{w\} \leq \sqrt{P_t}\right) = F_x\left(\sqrt{P_t}\right) \\ \text{and} \\ P\left(\mathcal{I}\{w\} \geq -\sqrt{P_t}\right) = P\left(\mathcal{I}\{w\} \leq \sqrt{P_t}\right) = F_x\left(\sqrt{P_t}\right) \end{array} . \tag{C.7}$$

  Therefore, because the probability of each of the above sub-categories is equal, all these symbols are considered under the name of outermost-constellation symbols.

Note that the intervals of interest for 64-QAM are the same as for the case of BPSK, with the difference that now the imaginary part has to be further considered. Therefore, we can generalize by saying that the intervals of interest for any M-QAM modulation scheme are the following for the real part: 1) $\mathcal{R}\{w[n]\} \leq -\sqrt{P_t}$; 2) $-\sqrt{P_t} \leq \mathcal{R}\{w[n]\} \leq \sqrt{P_t}$; and 3) $\mathcal{R}\{w[n]\} \geq \sqrt{P_t}$. The same intervals are valid for the imaginary part. Because of symmetry, we will work only with the real part, considering it twice. Then, taking into account all the possible transmitted symbols, the mean value for any M-QAM modulation scheme can be expressed as follows:

$$\begin{aligned} E\left\{\|\mathbf{y}\|^2 | H_{00}\right\} = \sum_{t=\frac{\sqrt{M}}{2}}^{t=\frac{\sqrt{M}}{2}} \sum_{k=\frac{\sqrt{M}}{2}}^{k=\frac{\sqrt{M}}{2}} \sum_{n=0}^{N-1} E\left\{|y[n]|^2 \left| s[n] = (2t-1)\sqrt{P_s} + j(2k-1)\sqrt{P_s}\right.\right. , \\ \left., \hat{s}[n] = (2t-1)\sqrt{P_s} + j(2k-1)\sqrt{P_s}\right\} P\left(s[n] = (2t-1)\sqrt{P_s} + j(2k-1)\sqrt{P_s}\right) \times \\ \times P\left(\hat{s}[n] = (2t-1)\sqrt{P_s} + j(2k-1)\sqrt{P_s} \,|c_{M-Q}\right) \end{aligned} \tag{C.8}$$

where c_{M-Q} represents the correct decision for M-QAM.

Based on the constraints of (C.1)-(C.7) and following the same methodology as in Appendix A, (C.8) can be further determined by (C.9),

$$E\left\{|y'|^2|\mathcal{H}_{0,k=t,t=k}\right\} = \underbrace{2E\left\{\mathcal{R}^2\{y'\}\left|-\sqrt{P_t} \le \mathcal{R}\{w\} \le \sqrt{P_t}\right\} P_{int}}_{A}$$
$$+\underbrace{2E\left\{\mathcal{R}^2\{y'\}\left|-\sqrt{P_t} \le \mathcal{R}\{w\} \le \sqrt{P_t}\right\} P_{ext1}}_{B} + \underbrace{2\frac{2}{\sqrt{M}}E\left\{\mathcal{R}^2\{y'\}\left|\mathcal{R}\{w\} \ge \sqrt{P_t}\right\} P_{ext2}}_{C}$$
$$+\underbrace{2\frac{4}{\sqrt{M}}E\left\{\mathcal{R}^2\{y'\}\left|\mathcal{R}\{w\} \ge \sqrt{P_t}\right\} P_{ext3}}_{D}, \tag{C.9}$$

where the factor 2 expresses the symmetry between the real and imaginary part, $P_{int} = \frac{P\left(-\sqrt{P_t}\le\mathcal{R}\{w\}\le\sqrt{P_t}\right)\,P\left(-\sqrt{P_t}\le\mathcal{I}\{w\}\le\sqrt{P_t}\right)}{P_{c_{\mathrm{M-Q}}}}$, $P_{ext1} = \frac{P\left(-\sqrt{P_t}\le\mathcal{R}\{w\}\le\sqrt{P_t}\right)P\left(\mathcal{I}\{w\}\ge\sqrt{P_t}\right)}{P_{c_{M-Q}}}$, and $P_{ext2} = \frac{P\left(\mathcal{R}\{w\}\ge\sqrt{P_t}\right)P\left(\mathcal{I}\{w\}\ge\sqrt{P_t}\right)}{P_{c_{M-Q}}}$. The first item of (C.9), defined as A, is valid for all the transmitted symbols of (C.8), the second and third item, defined as B and C, respectively, are valid for all the symbols except the inter-constellation symbols and for this reason are weighted by the factor $\frac{2}{\sqrt{M}}$, while the fourth item, defined as D, is only valid for the outermost-constellation symbols and that's why is weighted by the factor $\frac{4}{M}$. Based on this analysis, the proof of (3.36) is obtained.

Appendix D

Derivation of the mean μ_{w_M-Q}

The derivation of the mean for the wrong decoding is much more complicated than the correct decoding case. As showed earlier, there are three possible hypotheses regarding the wrong decoding when the transmitted signal from SU-Tx is QPSK modulated. This number of hypotheses greatly increases for higher modulation schemes and the generalization to any M-QAM scheme is not so easy but can be obtained with the following procedure.

Let's assume that the transmitted symbol of interest is the symbol $s_{29} = \sqrt{P_s} + j\sqrt{P_s}$ of Figure C.1. Then, the received signal is decoded wrongly according to the following constraints for the real part of noise:

$$\begin{aligned}
C_1: &\quad -6\sqrt{P_t} + \mathcal{R}\{w[n]\} \geq -\sqrt{P_t} \\
C_2: &\quad -\sqrt{P_t} \leq -4\sqrt{P_t} + \mathcal{R}\{w[n]\} \leq +\sqrt{P_t} \\
C_3: &\quad -\sqrt{P_t} \leq -2\sqrt{P_t} + \mathcal{R}\{w[n]\} \leq +\sqrt{P_t} \\
C_4: &\quad -\sqrt{P_t} \leq +2\sqrt{P_t} + \mathcal{R}\{w[n]\} \leq +\sqrt{P_t} \\
C_5: &\quad -\sqrt{P_t} \leq +4\sqrt{P_t} + \mathcal{R}\{w[n]\} \leq +\sqrt{P_t} \\
C_6: &\quad -\sqrt{P_t} \leq +6\sqrt{P_t} + \mathcal{R}\{w[n]\} \leq +\sqrt{P_t} \\
C_7: &\quad +8\sqrt{P_t} + \mathcal{R}\{w[n]\} \leq +\sqrt{P_t}
\end{aligned} \quad . \tag{D.1}$$

First, it is shown why the constraint C_3 takes this shape.

- The constraint C_3 for the real part of the noise is valid when we decide wrongly that the transmitted symbols is the symbol s_{30} or any another symbol in the same column with s_{30} (Figure C.1), instead of the symbol s_{29}. Therefore, the condition which guarantees that the estimated symbol is $\hat{s}[n] = s_{30} = 3\sqrt{P_s} + j\sqrt{P_s}$ is given as follows:

$$2\sqrt{P_t} \leq \sqrt{P_t} + \mathcal{R}\{w[n]\} \leq 4\sqrt{P_t} \;\Rightarrow\; \sqrt{P_t} \leq +\mathcal{R}\{w[n]\} \leq 3\sqrt{P_t}. \tag{D.2}$$

- Following the steps of the proposed algorithm in Section 3.2, we have to remove the estimated symbol from the received signal and focused on the real part, it is shown show that

$$\begin{aligned}\mathcal{R}\left(y[n]\right) &= \mathcal{R}\left\{s_{29}\right\} + \mathcal{R}\left\{w[n]\right\} - \mathcal{R}\left\{s_{30}\right\} \\ &= \sqrt{P_t} + \mathcal{R}\left\{w[n]\right\} - 3\sqrt{P_t} = -2\sqrt{P_t} + \mathcal{R}\left\{w[n]\right\}. \end{aligned} \tag{D.3}$$

- Because the ED is applied in the remaining signal, namely in the signal of (D.3), there is interest for the constraints of this quantity. Therefore, adding the factor $-2\sqrt{P_t}$ in (D.2), the constraint C_3 is proved.

Going back to the constraints of (D.1), it can be noticed that the intervals of interest are the same as before for the real part, which are also, due to symmetry, valid for the imaginary part. Furthermore, it can be seen that the constraints have different mean value, range from -6 to +8 for the transmitted symbol s_{29}. Therefore, following again the law of total expectations the mean value of the test statistic under the scenario of wrong decoding when the transmitted signal from SU-Tx is M-QAM modulated can be expressed as follows:

$$\begin{aligned}&\mu_{w\_M-Q} = E\left\{\|\mathbf{y}\|^2 \,|\text{wrong}\right\} = \sum_{n=0}^{N-1} E\left\{|y\left[n\right]|^2 \,|\text{wrong}\right\} = \\ &= \sum_{n=0}^{N-1}\sum_{k=1}^{M}\sum_{t=1,t\neq k}^{M} E\left\{|y\left[n\right]|^2 \,|s\left[n\right]=s_k, \hat{s}\left[n\right]=s_t\right\} P\left(s\left[n\right]=s_k\right) P\left(\hat{s}\left[n\right]=s_t \,|w_{M-Q}\right),\end{aligned} \tag{D.4}$$

where w_{M-Q} represents the decision for M-QAM and $P\left(s\left[n\right]=s_k\right)=\frac{1}{M}$. Let's see how (D.4) works for k=29 and t=30, namely for the case that the transmitted symbols is the symbol s_{29} and the estimated symbol is the symbol s_{30} of Figure C.1.

$$\begin{aligned}E\left\{\|\mathbf{y}\|^2\right\} &= \frac{1}{M}\sum_{n=0}^{N-1} E\left\{|y\left[n\right]|^2 \,|s\left[n\right]=s_{29}, \hat{s}\left[n\right]=s_{30}\right\} P\left(\hat{s}\left[n\right]=s_{30} \,|w_{M-Q}\right) = \\ &= \frac{1}{M}\sum_{n=0}^{N-1} E\left\{\mathcal{R}\left\{|y\left[n\right]|^2\right\} \,|\mathcal{R}\left\{s\left[n\right]\right\}=\mathcal{R}\left\{s_{29}\right\}, \mathcal{R}\left\{\hat{s}\left[n\right]\right\}=\mathcal{R}\left\{s_{30}\right\}\right\}\times \\ &\times P\left(\mathcal{R}\left\{\hat{s}\left[n\right]\right\}=\mathcal{R}\left\{s_{30}\right\} \,|w_{M-Q}\right) + \text{imaginary part}.\end{aligned} \tag{D.5}$$

As have mentioned many times so far, because of symmetry we focus only on the real part and we assume that the imaginary part follows the same behaviour. Therefore,

(D.5) can be further written as follows:

$$E\left\{\|\mathcal{R}\{\mathbf{y}\}\|^2\right\} = \frac{1}{M}\sum_{n=0}^{N-1} E\left\{\left|-2\sqrt{P_t}+\mathcal{R}\{w[n]\}\right|^2 \left|-\sqrt{P_t} \le -2\sqrt{P_t}+\mathcal{R}\{w[n]\} \le \sqrt{P_t}\right.\right\}\times$$
$$\times \frac{P\left(\sqrt{P_t} \le \mathcal{R}\{w[n]\} \le 3\sqrt{P_t}\right) P\left(-\sqrt{P_t} \le \mathcal{I}\{w[n]\} \le \sqrt{P_t}\right)}{P_{w\_M-Q}}, \tag{D.6}$$

where P_{w_M-Q} represents the probability of correct decision for M-QAM.

If now we examine how (D.4) behaves for k=29 and t=22, we will see that the final result is like in (D.6), with the only difference being the last probability for the imaginary part:

$$E\left\{\|\mathcal{R}\{\mathbf{y}\}\|^2\right\} = \frac{1}{M}\sum_{n=0}^{N-1} E\left\{\left|-2\sqrt{P_t}+\mathcal{R}\{w[n]\}\right|^2 \left|-\sqrt{P_t} \le -2\sqrt{P_t}+\mathcal{R}\{w[n]\} \le \sqrt{P_t}\right.\right\}\times$$
$$\times \frac{P\left(\sqrt{P_t} \le \mathcal{R}\{w[n]\} \le 3\sqrt{P_t}\right) P\left(\sqrt{P_t} \le \mathcal{I}\{w[n]\} \le 3\sqrt{P_t}\right)}{P_{w\_M-Q}}. \tag{D.7}$$

Therefore, it can be noticed that the symbols which are in the same column with that of s_{30} can be expressed with the same equation except the last probability for the imaginary part. Taking into account all these symbols (the symbols in the circle of Figure C.1) and taking out the common factor, the final expression is the following (k=29 and t=6, 14, 22, 30, 38, 46, 54, 62):

$$E\left\{\|\mathcal{R}\{\mathbf{y}\}\|^2\right\} = \frac{1}{M}\sum_{n=0}^{N-1} E\left\{\left|-2\sqrt{P_t}+\mathcal{R}\{w[n]\}\right|^2 \left|-\sqrt{P_t} \le -2\sqrt{P_t}+\mathcal{R}\{w[n]\} \le \sqrt{P_t}\right.\right\}\times$$
$$\times \frac{P\left(\sqrt{P_t} \le \mathcal{R}\{w[n]\} \le 3\sqrt{P_t}\right)}{P_{w\_M-Q}}, \tag{D.8}$$

because the summation of the different probabilities for the imaginary part is equal to one.

However, if we examine how (D.4) behaves for k=29 and t=2 (s_2), namely for a symbol in a different column than that of s_{30}, we see that the result is given as follows:

$$E\left\{\|\mathcal{R}\{\mathbf{y}\}\|^2\right\} = \frac{1}{M}\sum_{n=0}^{N-1} E\left\{\left|6\sqrt{P_t}+\mathcal{R}\{w[n]\}\right|^2 \left|-\sqrt{P_t} \le 6\sqrt{P_t}+\mathcal{R}\{w[n]\} \le \sqrt{P_t}\right.\right\}\times$$
$$\times \frac{P\left(-7\sqrt{P_t} \le \mathcal{R}\{w[n]\} \le -5\sqrt{P_t}\right) P\left(\mathcal{I}\{w[n]\} \ge 5\sqrt{P_t}\right)}{P_{w\_M-Q}}. \tag{D.9}$$

As before, considering all the symbols which are in the same column with the symbol s_2, (D.9) can be simplified in (D.10) as follows:

$$E\left\{\|\mathcal{R}\{\mathbf{y}\}\|^2\right\} = \frac{1}{M}\sum_{n=0}^{N-1} E\left\{\left|6\sqrt{P_t}+\mathcal{R}\{w[n]\}\right|^2 \left|-\sqrt{P_t} \le 6\sqrt{P_t}+\mathcal{R}\{w[n]\} \le \sqrt{P_t}\right.\right\}\times$$
$$\times \frac{P\left(-7\sqrt{P_t} \le \mathcal{R}\{w[n]\} \le -5\sqrt{P_t}\right)}{P_{w\_M-Q}}. \tag{D.10}$$

Hence, it can noticed that under the case that the transmitted symbols is the symbol s_{29}, each column of the constellation gives different result (different mean value). The same happens if we consider the other transmitted symbols. Thus, the goal is to find how many transmitted symbols satisfy (D.8), how many satisfy (D.10) and etc. and this can be answered ny noticing the constellation of Figure C.1. Then, with some simple process the mean of (3.39) is proved. Similar methodology is followed for the derivation of (3.40), (3.41), (3.42) and (3.43).

Appendix E

Distribution of the channel estimation error

First, the channel estimation under the hypothesis $\mathcal{H}_0$ is derived. With the use of a least square estimator, it can be written that

$$\hat{h} = \left(\mathbf{s}_p^H \mathbf{s}_p\right)^{-1} \mathbf{s}_p^H \mathbf{y}_p. \tag{E.1}$$

By substituting (4.6) to (E.1), it can be shown that

$$\begin{aligned} \hat{h} &= \left(\mathbf{s}_p^H \mathbf{s}_p\right)^{-1} \mathbf{s}_p^H h \mathbf{s}_p + \left(\mathbf{s}_p^H \mathbf{s}_p\right)^{-1} \mathbf{s}_p^H \mathbf{w}_p \\ &= h + \left(\mathbf{s}_p^H \mathbf{s}_p\right)^{-1} \mathbf{s}_p^H \mathbf{w}_p \\ &= h + \varepsilon_{\mathcal{H}_0}, \end{aligned} \tag{E.2}$$

where $\varepsilon_{\mathcal{H}_0} = \left(\mathbf{s}_p^H \mathbf{s}_p\right)^{-1} \mathbf{s}_p^H \mathbf{w}_p$. Then, it is easy to show that the mean of the channel estimation error is zero, because $\mathbb{E}\left\{\varepsilon_{\mathcal{H}_0}\right\} = \left(\mathbf{s}_p^H \mathbf{s}_p\right)^{-1} \mathbf{s}_p^H \mathbb{E}\left\{\mathbf{w}_p\right\} = 0$.

Furthermore, the covariance matrix of $\varepsilon_{\mathcal{H}_0}$ is computed as follows:

$$\begin{aligned} \mathbb{E}\left\{\varepsilon_{\mathcal{H}_0} \varepsilon_{\mathcal{H}_0}^*\right\} &= \mathbb{E}\left\{\left(\mathbf{s}_p^H \mathbf{s}_p\right)^{-1} \mathbf{s}_p^H \mathbf{w}_p \left[\left(\mathbf{s}_p^H \mathbf{s}_p\right)^{-1} \mathbf{s}_p^H \mathbf{w}_p\right]^H\right\} \\ &= \sigma_{w_p}^2 \left\{\left(\mathbf{s}_p^H \mathbf{s}_p\right)^{-1} \mathbf{s}_p^H \mathbf{s}_p \left(\mathbf{s}_p^H \mathbf{s}_p\right)^{-1}\right\} \\ &= \sigma_{w_p}^2 \left(\mathbf{s}_p^H \mathbf{s}_p\right)^{-1} = \frac{\sigma_{w_p}^2}{E_p}. \end{aligned} \tag{E.3}$$

Therefore, the channel estimation error can be considered Gaussian distributed: $\varepsilon_{\mathcal{H}_0} \sim \mathcal{N}\left(0, \frac{\sigma_{w_p}^2}{E_p}\right)$. Similar methodology can be followed for the computation of the channel estimation error under the hypothesis $\mathcal{H}_1$: $\varepsilon_{\mathcal{H}_1} \sim \mathcal{N}\left(0, \frac{\sigma_{w_p}^2 + \sigma_{i_p}^2}{E_p}\right)$.

Appendix F

Covariance matrix of (4.9) and (4.10)

First, the derivation of the covariance matrix of (4.9) is presented, which is given as follows:

$$\begin{aligned}\mathbb{E}\left\{\mathbf{y}'_p{\mathbf{y}'_p}^H|\mathcal{H}'_{0_p}\right\} &= \mathbb{E}\left\{\left(\mathbf{w}_p - \varepsilon_{\mathcal{H}_0}\mathbf{s}_p\right)\left(\mathbf{w}_p^H - \varepsilon^*_{\mathcal{H}_0}\mathbf{s}_p^H\right)\right\} \\ &= \mathbb{E}\left\{\mathbf{w}_p\mathbf{w}_p^H\right\} - \mathbb{E}\left\{\mathbf{w}_p\mathbf{s}_p^H\varepsilon^H_{\mathcal{H}_0}\right\} - \mathbb{E}\left\{\varepsilon_{\mathcal{H}_0}\mathbf{s}_p\mathbf{w}_p^H\right\} + \mathbb{E}\left\{\varepsilon_{\mathcal{H}_0}\mathbf{s}_p\mathbf{s}_p^H\varepsilon^H_{\mathcal{H}_0}\right\},\end{aligned} \tag{F.1}$$

where

$$A = \mathbb{E}\left\{\mathbf{w}_p\mathbf{w}_p^H\right\} = \sigma^2_{w_p}\mathbf{I}_{N_p}, \tag{F.2}$$

$$\begin{aligned}B = \mathbb{E}\left\{\mathbf{w}_p\mathbf{s}_p^H\varepsilon^*_{\mathcal{H}_0}\right\} = \mathbb{E}\left\{\mathbf{w}_p\varepsilon^*_{\mathcal{H}_0}\mathbf{s}_p^H\right\} &= \mathbb{E}\left\{\mathbf{w}_p\left(\left(\mathbf{s}_p^H\mathbf{s}_p\right)^{-1}\mathbf{s}_p^H\mathbf{w}_p\right)^H\mathbf{s}_p^H\right\} \\ &= \mathbb{E}\left\{\mathbf{w}_p\mathbf{w}_p^H\mathbf{s}_p\left(\mathbf{s}_p^H\mathbf{s}_p\right)^{-1}\mathbf{s}_p^H\right\} = \sigma^2_{w_p}\left(\mathbf{s}_p^H\mathbf{s}_p\right)^{-1}\mathbf{s}_p\mathbf{s}_p^H,\end{aligned} \tag{F.3}$$

$$\begin{aligned}C = \mathbb{E}\left\{\varepsilon_{\mathcal{H}_0}\mathbf{s}_p\mathbf{w}_p^H\right\} = \mathbb{E}\left\{\mathbf{s}_p\varepsilon_{\mathcal{H}_0}\mathbf{w}_p^H\right\} &= \mathbb{E}\left\{\mathbf{s}_p\left(\mathbf{s}_p^H\mathbf{s}\right)^{-1}\mathbf{s}_p^H\mathbf{w}\mathbf{w}_p^H\right\} \\ &= \sigma^2_{w_p}\left(\mathbf{s}_p^H\mathbf{s}_p\right)^{-1}\mathbf{s}_p\mathbf{s}_p^H,\end{aligned} \tag{F.4}$$

and

$$D = \mathbb{E}\left\{\varepsilon_{\mathcal{H}_0}\mathbf{s}_p\left(\varepsilon^*_{\mathcal{H}_0}\mathbf{s}_p^H\right)\right\} = \mathbf{s}_pE\left\{\varepsilon_{\mathcal{H}_0}\varepsilon^*_{\mathcal{H}_0}\right\}\mathbf{s}_p^H = \sigma^2_{w_p}\left(\mathbf{s}_p^H\mathbf{s}_p\right)^{-1}\mathbf{s}_p\mathbf{s}_p^H. \tag{F.5}$$

Therefore, the covariance matrix of $\mathbf{y}'_p$ under the hypothesis $\mathcal{H}'_{0_p}$ is given by

$$\mathbb{E}\left\{\mathbf{y}'_p{\mathbf{y}'_p}^H|\mathcal{H}'_{0_p}\right\} = A + B + C + D = \sigma^2_{w_p}\mathbf{I}_{N_p} - \sigma^2_{w_p}\left(\mathbf{s}_p^H\mathbf{s}_p\right)^{-1}\mathbf{s}_p\mathbf{s}_p^H$$
$$= \sigma^2_{w_p}\mathbf{I}_{N_p} - \frac{\sigma^2_{w_p}}{E_p}\mathbf{s}_p\mathbf{s}_p^H. \tag{F.6}$$

Then, it can be noticed that this covariance matrix is not a diagonal matrix, which implies that elements of the vector $\mathbf{y}'_p$ under the hypothesis $\mathcal{H}_{0_p}$ are correlated.

Similar methodology can be followed for the derivation of the covariance matrix of (4.10).

Appendix G

Derivation of $\overline{P_{FA}}$ in (4.30)

With the help of [100], eq. (13)], any integral of the following form can be solved:

$$\mathcal{F}\left(k, m, a, b, p\right) = \int_0^\infty x^{k-1} Q_m\left(a\sqrt{x}, b\right) e^{-px} dx. \tag{G.1}$$

Therefore, (4.35) can be translated to (G.1) as follows:

$$\overline{P_{FA_d}} = \zeta \int_0^\infty x^{k-1} Q_m\left(a\sqrt{x}, b\right) e^{-px} dx, \tag{G.2}$$

where $x = \varepsilon^2_{\mathcal{H}_0}$, $\zeta = \frac{1}{2^{1/2}\Gamma(1/2)}$, $k = \frac{1}{2}$, $m = \frac{N_d}{2}$, $a = \sqrt{\frac{E_d}{\sigma^2_{w_d}}}$, $b = \sqrt{\frac{\gamma_d}{\sigma^2_{w_d}}}$ and $p = \frac{1}{2}$. Then, the average probability of false alarm can be written as in (4.30).

Bibliography

[1] J. Mitola III, G. Q. Maguire, Jr., "Cognitive radios: making software radio more personal," *IEEE Pers. Commun.*, vol. 6, no. 4, pp. 13–18, Aug. 1999.

[2] S. Haykin,"Cognitive radio: brain-empowered wireless communications," *J. Sel. Areas Commun.*, vol. 23, no. 2, pp. 201-220, Feb. 2005.

[3] S.-K. Sharma, T.-E. Bogale S. Chatzinotas, B. Ottersten, L.-B. Le, X. Wang, "Cognitive Radio Techniques under Practical Imperfections: A Survey," *IEEE Commun. Surveys and Tutorials*, vol. 17, no. 4, pp. 1858-1884, Nov. 2015.

[4] D.Cabric, S. M. Mishra, R. W. Brodersen, "Implementation issues in spectrum sensing for cognitive radios," *Proc. Asilomar Comf. Signals, Syst., Comput.*, Pacific Grove, CA, USA, pp. 772-776, Nov. 2004.

[5] H. Urkowitz, "Energy detection of unknown deterministic signals," *Proc. of the IEEE*, vol. 55, no. 4, pp. 523-531, Apr. 1967.

[6] F. Digham, M.-S. Alouini, M.K. Simon, "On the energy detection of unknown signals over fading channels," *IEEE Trans. Commun.*, vol. 55, no. 1, pp. 21-24, Jan. 2007.

[7] R. Tandra, A. Sahai, "Fundamental limits on detection in low SNR under noise uncertainty," *Proc. IEEE Int. Conf. Wireless Netw., Commun. Mobile Comput.*, Maui, HI, USA, vol. 1, pp, 464-469, Jun. 2005.

[8] S. Atapattu, C. Tellambura, H. Jiang, "Performance of an energy detector over channels with both multipath fading and shadowing," *IEEE Trans. Wireless Commun.*, vol. 9, no. 12, pp. 3662-3670, Dec. 2010.

[9] P.D. Sutton, K.E. Nolan, L. E. Doyle, "Cyclostationary signatures in practical cognitive radio applications," *J. Sel. Areas Commun.*, vol. 26, no. 1, pp. 13-24, Jan. 2008.

[10] R. Zhang, T. J. Lim, Y.-C. Liang, Y. Zeng, "Multi-Antenna Based Spectrum Sensing for Cognitive Radios: A GLRT Approach," *IEEE transactions on communications*, vol. 58, no. 1, Jan. 2010.

[11] P. Wang, J. Fang, N. Han, H. Li, "Multiantenna-Assisted Spectrum Sensing for Cognitive Radio," *IEEE Trans. on Vehicular Technology*, vol. 59, no. 4, May 2010.

[12] C. Tsinos, K. Berberidis, "Decentralized Adaptive Eigenvalue-Based Spectrum Sensing for Multiantenna Cognitive Radio Systems," *IEEE Trans. Wireless Commun.*, vol. 14, no. 3, Mar. 2015.

[13] Y. C. Liang, Y. Zeng, E. Peh, A. T. Hoang, "Sensing-throughput tradeoff for cognitive radio networks," *IEEE Trans. Wireless Commun.*, vol. 7, no. 4, pp. 1326-1337, Apr. 2008.

[14] S. H. Song, K. Hamdi, K. B. Letaief, "Spectrum sensing with active cognitive systems," *IEEE Pers. Commun.*, vol. 9, no. 6, pp. 1849-1854, Jun. 2010.

[15] E. Tsakalaki, O. N. Alrabadi, A. Tatomirescu, E. Cavalho, and G. F. Pedersen, "Concurrent communication and sensing in cognitive radio devices: challenges and an enabling solution," *IEEE Trans. Antennas Propag.*, vol. PP, no. 99, Aug. 2013.

[16] J.Heo, H. Ju,S. Park, E. Kim, D. Hong, "Simultaneous Sensing and Transmission in Cognitive Radio," *IEEE Trans. Wireless Commun.*, vol. 13, no. 4, Apr. 2014.

[17] Y. Liao, T. Wang, L. Song, Z. Han, "Listen-and-Talk: Protocol Design and Analysis for Full-duplex Cognitive Radio Networks," *IEEE Trans. on Vehicular Technology.*, accepted for publication, 2016.

[18] S. K. Sharma, T. E. Bogale, L. B. Le, S. Chatzinotas, X. Wang, B. Ottersten, "Two-Phase Concurrent Sensing and Transmission Scheme for Full Duplex Cognitive Radio," *in Proc. IEEE VTC Spring*, Sept. 2016.

[19] W. Lee, D.-H. Cho, "Concurrent spectrum sensing and data transmission scheme in a CR system," *Proc. 2012 IEEE Wireless Commun. Netw. Conf.*, Paris, France, pp. 1326-1330., Apr. 2012.

[20] S. Stotas, A. Nallanathan, "On the throughput and spectrum sensing enhancement of opportunistic spectrum access cognitive radio networks," *IEEE Trans. Wireless Comm.*, vol. 11, pp. 97-101, Jan. 2012.

[21] *Technology Roadmap: Interference Monitoring, Detection/Isolation, Classification, Localisation and Mitigation*, ESA document, May 2015.

[22] R. Ames, "Satellite interference: What it means for your bottom life," www.integ.com/is3/whitepapers/sktelecommnews.pdf, *access*: 01/07/2018.

[23] ETSI TS 103 129 V1.1.1 (2013-05), "Digital Video Broadcasting (DVB); Framing structure, channel coding and modulation of a carrier identification system (DVB-CID) for satellite transmission."

[24] C. Politis, S. Maleki, S. Chatzinotas, B. Ottersten, "Harmful Interference Threshold and Energy Detector for On-Board Interference Detection," *22nd Ka band and Broadband Communications Conference*, Cleveland, USA, Oct. 2016.

[25] C. Politis, S. Maleki, C. Tsinos, S. Chatzinotas, B. Ottersten, "On-board the satellite interference detection with imperfect signal cancellation," *IEEE Intern. Workshop on Sig. Proc. Advanc.in Wirel. Comm.*, Edinburgh, Scotland, Jul. 2016.

[26] S. Smith, SES, "Satellite Interference Commercial Industry Views," presented at satellite Interference Reduction Group (sIRG), Jun. 2013.

[27] L. Luo, N. M. Neihart, S. Roy, D. J. Allstot, "A two-stage sensing technique for dynamic spectrum access", *IEEE Transactions on Wireless Communications*, pp. 3028-3037, Jun. 2009.

[28] S. Maleki, A. Pandharipande, G. Leus, "Two-stage spectrum sensing for cognitive radios", *in IEEE International Conference in Acoustics, Speech and Signal Processing*, Dallas, USA, Mar. 2010.

[29] C. Politis, Ashkan Kalantari, S. Maleki, S. Chatzinotas, "On-board interference detection and localization for satellite communication," to appear in *SATCOMs in the 5G Era*, IET, 2018.

[30] C. Politis, S. Maleki, C. Tsinos, K. Liolis, S. Chatzinotas, B. Ottersten, "Simultaneous Sensing and Transmission for Cognitive Radios with Imperfect Signal Cancellation," *in IEEE Transactions on Wireless Communications (TWC)*, vol. 16, no. 9, pp. 5599–5615, Sep. 2017.

[31] C. Politis, S. Maleki, C. Tsinos, S. Chatzinotas, B. Ottersten, "Weak interference detection with signal cancellation in satellite communications," *in IEEE International Conference on Acoustis, Speech, and Signal Processing (ICASSP)*, New Orleans, USA, Mar. 2017.

[32] C. Politis, S. Maleki, C. Tsinos, K. Liolis, S. Chatzinotas, B. Ottersten, "Energy Detector with Imperfect Signal Cancellation for Interference Detection On-board the Satellite, *in IEEE Transactions on Aerospace and Electronic Systems*, 2018, *submitted.*

[33] C. Politis, S. Maleki, J. C. M. Duncan, J. Krivochiza, S. Chatzinotas, B. Ottersten, "SDR Implementation of a Testbed for Real-Time Interference Detection with Signal Cancellation, *in IEEE Access*, 2018, *submitted.*

[34] J. Mitola, *Cognitive Radio Architecture: The Engineering Foundations of Radio XML*, 1st ed. Wiley, Oct. 2006.

[35] FCC, "Notice of proposed rule making and order," ET Docket 03-322, 2003.

[36] R. S. Groups, "Working document towards a preliminary draft new report: Software defined radio in land mobile services (question 230-1/8)," ITU, Tech. Rep. 8A/121-E, Sept. 2004.

[37] T. R. Shields, "SDR update," Global Standards Collaboration, Sophia Antipolis, France, Tech. Rep., Sept. 2005.

[38] A. Shukla and et al, "Cognitive radio technology: A study for OFCOM," QinetiQ, Tech. Rep. QINETIQ/ 06/00420 Issue 1.1, Feb. 2007.

[39] I. Akyildiz, W.-Y. Lee, M. C. Vuran, and S. Mohanty, "A survey on spectrum management in cognitive radio networks," *IEEE Commun. Mag.*, vol. 46, no. 4, pp. 40-48, April 2008.

[40] K. Letaief and W. Zhang, "Cooperative communications for cognitive radio networks," *Proceedings of the IEEE*, vol. 97, no. 5, pp. 878-893, May 2009.

[41] I. F. Akyildiz, W.-Y. Lee, M. C. Vuran, S. Mohanty, "A survey on spectrum management in cognitive radio networks," *IEEE Commun. Mag.*, vol. 46, no. 4, pp. 40-48, Apr. 2008.

[42] M. T. Masonta, M. Mzyece, N. Ntlatlapa "Spectrum decision in cognitive radio networks: A survey," *IEEE Commun. Surveys and Tutorials*, vol. 15, no. 3, pp. 1088-1107, 2013.

[43] T. Yucek and H. Arslan, "A survey of spectrum sensing algorithms for cognitive radio applications," *IEEE Commun. Surveys & Tutorials*, vol. 11, no. 1, pp. 116-130, 2009.

[44] E. Axell, G. Leus, E. Larsson, and H. Poor, "Spectrum sensing for cognitive radio: State-of-the-art and recent advances," *IEEE Signal Process. Magazine*, vol. 29, no. 3, pp. 101-116, May 2012.

[45] J. G. Proakis, M. Salehi,*Digital Communications*, 5th Edition, McGraw-Hill, 2008.

[46] D. Cabric, A. Tkachenko, and R. Brodersen, "Spectrum sensing measurements of pilot, energy, and collaborative detection," *in IEEE Military Commun. Conf.*, Oct. 2006, pp. 1-7.

[47] S. Herath, N. Rajatheva, and C. Tellambura, "Energy detection of unknown signals in fading and diversity reception," *IEEE Trans. Commun.*, vol. 59, no. 9, pp. 2443-2453, Sept. 2011.

[48] F. F. Digham, M.-S. Alouini, and M. K. Simon, "On the energy detection of unknown signals over fading channels," *IEEE Trans. Commun.*, vol. 55, no. 1, pp. 21-24, Jan. 2007.

[49] S. M. Kay, *Fundamentals of Statistical Signal Processing: Detection Theory*, Upper Saddle River, NJ: Prentice-Hall, 1998.

[50] Y. Zeng, C. L. Koh, and Y.-C. Liang, "Maximum eigenvalue detection: Theory and application," *in IEEE Int. Conf. Commun.*, May 2008, pp. 4160-4164.

[51] Y. Zeng and Y.-C. Liang, "Eigenvalue-based spectrum sensing algorithms for cognitive radio," *IEEE Trans. Commun.*, vol. 57, no. 6, pp. 1784-1793, June 2009.

[52] L. Cardoso, M. Debbah, P. Bianchi, and J. Najim, "Cooperative spectrum sensing using random matrix theory," *in 3rd Int. Symp. Wireless Pervasive Computing*, May 2008, pp. 334-338.

[53] F. Penna, R. Garello, and M. Spirito, "Cooperative spectrum sensing based on the limiting eigenvalue ratio distribution in Wishart matrices," *IEEE Commun. Letters*, vol. 13, no. 7, pp. 507-509, July 2009.

[54] A. Kortun and et al, "On the performance of eigenvalue-based cooperative spectrum sensing for cognitive radio," *IEEE J. Sel. Topics Signal Process.*, vol. 5, no. 1, pp. 49-55, Feb. 2011.

[55] D. Cabric and R. Brodersen, "Physical layer design issues unique to cognitive radio systems," *in IEEE PIMRC*, vol. 2, Sept. 2005, pp. 759-763.

[56] H. Tang, "Some physical layer issues of wide-band cognitive radio systems," *in First IEEE DySPAN*, Nov. 2005, pp. 151-159.

[57] H. Sun, A. Nallanathan, C.-X. Wang, and Y. Chen, "Wideband spectrum sensing for cognitive radio networks: a survey," *IEEE Wireless Commun.*, vol. 20, no. 2, pp. 74-81, April 2013.

[58] R. Sharma and J. Wallace, "Improved spectrum sensing by utilizing signal autocorrelation," *in IEEE 69th Veh. Technol. Conf.*, April 2009, pp. 1-5.

[59] R. Sharma and J. Wallace, "Improved autocorrelation-based sensing using correlation distribution information," *in Int. ITG Workshop on Smart Antennas (WSA)*, Feb 2010, pp. 335-341.

[60] Y. Zeng and Y.-C. Liang, "Spectrum-sensing algorithms for cognitive radio based on statistical covariances," *IEEE Trans. Vehicular Technol.*, vol. 58, no. 4, pp. 1804-1815, May 2009.

[61] M. Jin, Y. Li, and H.-G. Ryu, "On the performance of covariance based spectrum sensing for cognitive radio," *IEEE Trans. Signal Process.*, vol. 60, no. 7, pp. 3670-3682, July 2012.

[62] N. Miridakis, T. Tsiftsis, G. Alexandropoulos, M. Debbah, "Simultaneous spectrum sensing and data reception for cognitive spatial multiplexing distributed systems," *IEEE Transactions on Wireless Communications*, vol. 16, no. 5, pp. 3313-3327, May 2017.

[63] G. Maral, M. Bousquet, *Satellite Communication Systems*, 5th Ed., Wiley, 2009.

[64] Z. Sai, L. Liu, K. Long, "Improved energy detector with interference cancellation in heterogeneous cognitive wireless networks," *IEEE GLOBECOM*, California, USA, Dec., 2012.

[65] T. Riihonen, R. Wichman, "Energy detection in full-duplex cognitive radios under residual self-interference," *IEEE CROWNCOM*, Oulu, Finland, June, 2014.

[66] L. Tang, Y. Chen, A. Nallanathan, E. L. Hines, "Performance Evaluation of Spectrum Sensing Using Recovered Secondary Frames With Decoding Errors," *IEEE Transactions on Wireless Communications*, vol. 11, no. 8, pp. 2934-2945, Aug. 2012.

[67] G. Maral, *VSAT Networks*, 2nd Ed., Wiley, 2003.

[68] L. Castanet, A. Bolea-Alamanc, M. Bousquet, "Interference and fade mitigation techniques for Ka and Q/V band satellite communication systems," *in Proc. Int. Workshop on COST Actions 272 and 280*, Noordwijk, Netherlands, May 2003.

[69] E. Lavan, "Satellite Interference: an Operator's Perspective", Eutelsat Communications, Jun. 2013.

[70] R. Rideout, "Technologies to identify and/or mitigate harmful interference," *in International satellite communication workshop on the ITU-challenges in the 21st century: Preventing harmful interference to satellite systems*, Jun. 2013.

[71] S. K. Sharma, S. Chatzinotas, B. Ottersten, "In-line interference mitigation techniques for spectral coexistence of GEO and NGEO satellites," *international journal of satellite communications and networking*, vol. 34, issue. 1, pp. 11-39, Feb. 2016.

[72] A. Pourmoghadas, S. K. Sharma, S. Chatzinotas, B. Ottersten, "Cognitive Interference Management Techniques for the Spectral Co-existence of GSO and NGSO Satellites," *International Conference on Wireless and Satellite Systems*, Cardiff, UK, Sep. 2016.

[73] SIECAMS, "Satellite monitoring and geolocation system," https://atos.net/en/convergence-creators/portfolio/siecams/carrier-monitoring, *access*: 01/07/2018.

[74] H. Mahmoud, H. Arslan, "Error Vector Magnitude to SNR Conversion for Nondata-Aided Receivers," *IEEE Transactions on Wireless Communications*, vol 8, no 5, May 2009.

[75] GLOWLINK, "Communications Signal Interference Removal," http://www.glowlink.com/technologies/csir, *access*: 28/05/2018.

[76] Monics Net, "Carrier Monitoring and RFI Detection System," http://www.kratostts.com/products/satellite-and-space/satguard, *access*: 28/05/2018.

[77] SatGuard, "Identifying VSAT Terminals Causing Interference," http://www.kratostts.com/products/satellite-and-space/satguard, *access*: 28/05/2018.

[78] G. P. Wadsworth, J. G. Bryan, *Introduction to Probability and Random Variables,* McGraw-Hill, page 52, 1960.

[79] N.L. Johnson, S. Kotz, N. Balakrishnan, *Continuous Univariate Distributions*, Volume 1, Wiley, 1994.

[80] P. Damien, G. S. Walker, "Sampling truncated normal, beta, and gamma densities," *Journal of Computational and Graphical Statistics*, 2001.

[81] J. Rice, *Mathematical Statistics and Data Analysis*, Second Edition, Duxbury Press, 1995.

[82] P. Billingsley, *Probability and Measure*, Third Edition, John Wiley and Sons, 1995, page 357.

[83] C. S. Coffey, K. E. Muller, "Properties of Doubly-Truncated Gamma Variables," *Commun. Stat. Theory Methods*, Feb. 2000.

[84] E. Marchand, "Computing the moments of a truncated noncentral chi-square distribution," *Journal of Statistical Computation and Simulation*, Mar. 2007.

[85] P. J. Dhrymes, "Moments of truncated (normal) distributions", 2005.

[86] D. Tse, P. Viswanath, *Fundamentals of Wireless Communication*, Cambridge University Press, 2005.

[87] A. Taherpour, M. Nasiri-Kenari, S. Gazor, "Multiple antenna Spectrum Sensing in Cognitive Radios," *IEEE Trans. Wireless Commun.*, vol. 9, no. 2, Feb. 2010.

[88] D. Cabric, A. Tkachenko and R. W. Brodersen, "Experimental study of spectrum sensing based on energy detection and network cooperation," *First international workshop on Technology and policy for accessing spectrum*, 2006.

[89] R. Deng, J. Chen, C. Yuen, P. Cheng and Y. Sun, "Energy-Efficient Cooperative Spectrum Sensing by Optimal Scheduling in Sensor-Aided Cognitive Radio Networks," *IEEE Transactions on Vehicular Technology*, vol.61, no.2, pp.716,725, Feb. 2012.

[90] Q. Huang, P.J. Chung, "An F-Test Based Approach for Spectrum Sensing in Cognitive Radio," *IEEE Trans. Wireless Commun.*, vol. 12, no. 8, Aug. 2013.

[91] *Satellite Evolution Sparks a Service Revolution*, white paper, SES, Jun. 2016.

[92] P. Angeletti, R. De Gaudenzi, M. Lisi, "From Bent Pipes to Software Defined Payloads: Evolution and Trends of Satellite Communications Systems," 2008.

[93] *Digital Transparent Processor*, data sheet, Thales Alenia Space, Mar. 2012.

[94] A. Le Pera, F. Forni, M. Grossi, M. Lucente, V. Palma, T. Rossi, M. Ruggieri, "Digital transparent processor for satellite telecommunication services," *in IEEE Aerospace Conference*, Manhattan, USA, Mar. 2007.

[95] C.D. Hou, "A simple approximation for the distribution of the weighted combination of non-independent or independent probabilities," *Statistics and probability Letters*, vol. 73, issue 2, June 2005.

[96] M.S. Alouini, A. Abdi, and M. Kaveh, "Sum of Gamma Variates and Performance of Wireless Communication Systems Over Nakagami-Fading Channels," *IEEE Transactions on Vehicular Technology*, vol. 50, no. 6, Nov. 2001.

[97] ETSI EN 302 307-2 V1.1.1 (2014-10), Digital Video Broadcasting (DVB); "Second generation framing structure, channel coding and modulation systems for Broadcasting, Interactive Services, News Gathering and other broadband satellite applications; Part 2: DVB-S2 Extensions (DVB-S2X)."

[98] I. S. Gradshteyn, I. M. Ryzhik, *Table of Integrals, Series, and Products*, 7th Ed. ed. New York, NY, USA: Academic, 2007.

[99] Y. A. Brychkov, *Handbook of special functions: Derivatives, integrals, series and other formulas*, Boca Raton, FL, USA: CRC, 2008.

[100] P. C. Sofotasios, S. Muhaidat, G. K. Karagiannidis, B. S. Sharif, "Solutions to Integrals Involving the Marcum Q-Function and Applications," *IEEE Signal Processing Letters*, vol. 22, no. 10, Oct. 2015.

[101] ETSI EN 301 545-2 V1.2.1 (2014-04), Digital Video Broadcasting (DVB); "Second generation DVB Interactive satellite system (DVB-RCS2); Part 2: Lower layers for satellite standard."

[102] National Instruments, "AN INTRODUCTION TO SOFTWARE DEFINED RADIO With NI LabVIEW and NI USRP ," ftp://ftp.ni.com/pub/events/campus_workshop/niusrp_hands_on_sp_manual.pdf, *access*: 01/07/2018.

[103] National Instruments, "USRP Software Defined Radio Device," http://www.ni.com/en-gb/shop/select/usrp-software-defined-radio-device, *access*: 01/07/2018.

[104] National Instruments, "USRP-2954," http://www.ni.com/documentation/en/software-defined-radio-reconfigurable-device/latest/usrp-2954/overview/, *access*: 01/07/2018.

[105] National Instruments, "NI USRP-2954R Block Diagram," http://www.ni.com/documentation/en/labview-comms/2.0/2954r/block-diagram/, *access*: 01/07/2018.

[106] National Instruments, "USRP-2954 Specifications," http://www.ni.com/documentation/en/software-defined-radio-reconfigurable-device/latest/specs-usrp-2954/specs/, *access*: 01/07/2018.

[107] National Instruments, "LabVIEW Communications System Design Suite 2.0 Readme," http://download.ni.com/support/softlib/labview/labview_communications/2.0/readme_LVComms.html#LVCommssysreq, *access*: 01/07/2018.

[108] C. L. Clark, *LabVIEW Digital Signal Processing and Digital Communications*, McGraw-Hill, 2005.

[109] F. Jabbarvaziri, M. Nokhbeh-Zaeem, G. Moradi, "Preamble design for symbol synchronization in frequency-selective fading channels," *in IET Communications*, Apr. 2014.

[110] H.-S. Chen, W. Gao, D. G. Daut, "Spectrum sensing for OFDM systems employing pilot tones," *IEEE Trans. Wireless Commun.*, vol. 8, no. 12, pp. 5862-5860, Dec. 2009.

[111] H.-S. Chen, W. Gao, "Spectrum sensing for TV white space in North America," *IEEE J. Select. Areas Commun.*, vol. 29, no. 2, pp. 316-326, Feb. 2011.

[112] Schmidl, T.M., Cox, D.C.: "Robust frequency and timing synchronization for OFDM", *IEEE Trans. Commun.*, vol. 45, no. 12, 1997, pp. 1613–1621.

[113] Minn, H., Bhargava, V.K., Letaief, K.B.: "A robust timing and frequency synchronization for OFDM systems," *IEEE Trans. Wirel. Commun.*, vol. 2, no. 4, 2003, pp. 822–839.

[114] N. A. Weiss, *A Course in Probability*, Addison - Wesley, 2005, pages 385-386.

[115] A. Stuart, K. Ord, (1994), *Kendall's Advanced Theory of Statistics: Volume I — Distribution Theory*, Wiley, Jun. 1994.